VIBRONIC COHERENCE IN LIGHT-HARVESTING PROTEINS AND SEMICONDUCTOR NANOMATERIALS

By

Ryan Tilluck

A DISSERTATION

Submitted to
Michigan State University
in partial fulfillment of the requirements
for the degree of

Chemistry – Doctor of Philosophy

2020

ABSTRACT

VIBRONIC COHERENCE IN LIGHT-HARVESTING PROTEINS
AND SEMICONDUCTOR NANOMATERIALS

By

Ryan Tilluck

Light harvesting in photosynthetic organisms employ complex arrays of highly ordered chromophores in proteins for the capture and transfer of energy from solar photons. The structural design of the light harvesting proteins leads to extensive delocalization across many molecules of the system. Recent studies demonstrate the involvement of quantum coherence in extraordinarily fast energy transfer pathways in photosynthetic light harvesting proteins. The extent of delocalization may also form vibronic excitons, vibronic excitons, arising from quantum coherent mixing of vibrations with the extensively delocalized electronic states. Vibronic excitons can greatly enhance the excitation energy transfer within light harvesting systems. In this dissertation, the detection and role of quantum coherence in the peridinin–chlorophyll protein (PCP), a mid-visible peripheral light-harvesting protein in marine dinoflagellates that delivers excitation energy to photosystem II, will be discussed. This dissertation will also discuss the role of vibronic coherences, involving organic surface ligands, in the hot carrier cooling process of CdSe semiconductor quantum dots (QDs). Optical broadband two-dimensional electronic spectroscopy (2DES) with ultrashort pulses has been employed on these systems to characterize nonradiative decay and energy transfer pathways in PCP and CdSe QDs. Understanding the advantage gained by the organism through the use of coherent energy transfer mechanisms may enable the development of more efficient light harvesting materials for use in photovoltaic cells or in photocatalysis.

To my family and friends

ACKNOWLEDGEMENTS

My journey toward my doctorate has been incredible. It all started on a dual-island Caribbean nation, Trinidad and Tobago. Despite being my home for 18 years, it never truly felt like home, and my childhood educational institutions failed to support my academic ambitions. The many challenges faced during this journey never limited my ambitions, thanks to the many kind and supportive individuals who accompanied me along the way. Without their support and guidance, my success and journey towards a Ph.D. would have been an impossible task. I will forever be in their debt.

I would like to begin by thanking my graduate advisor, Professor Warren F. Beck, for the opportunity to learn and grow under his mentorship. It may not have always been easy, but you have guided and supported my journey, ensuring my success as a scientist and professional. The opportunity to serve as a teaching assistant to your undergraduate courses has allowed me to grow and improve my communication and teaching skills. You have also granted me the intellectual freedom to pursue new and innovative ideas, allowing me to follow my interests and passion in research. Thank you. Words fail to describe your impact on my life.

I would also like to thank my undergraduate advisor, Professor P. Gregory Van Patten, for his mentorship, motivation, and support. You were the first inspiration in this academic journey, and sparked my interest and love for nanomaterials and ultrafast spectroscopy. You granted me the freedom to explore and experiment in your laboratory at Middle Tennessee State University, which has only served to expand my experience and knowledge. And, well after my departure, you have continued to support my endeavors, forming a collaboration with my graduate laboratory to pursue new and exciting research endeavors. Thank you.

I would also like to thank my senior colleagues from the Beck Laboratory. Firstly, Dan (Dr. Jerome Roscioli), for your guidance during my early days in research. It has been an absolute pleasure working alongside you, designing one of the most elegant and robust (and non-barbaric) two-dimensional electronic spectrometers. The success that followed my graduate research hinged on the success of our instrument. I have learned a lot from you, and I am thankful for your friendship. Secondly, Jessica, you have been my longest friendship and long-time colleague. From our days researching in the Van Patten Laboratory, to our days at the Beck Laboratory, you have brought laughter, joy, and support to my journey. Thank you for your friendship. Dr. Soumen Ghosh, you guided me in my early months in the Beck Laboratory, and I continue to learn from you to this day. Thank you for your support and your friendship. Nila, Sourav, and Justin, I wish you all the best in your graduate and postgraduate careers. It has been a pleasure working alongside you, and I am excited to see where you carry the research. I am also grateful to my committee members, Professors Marcos Dantus, Benjamin Levine, and John McCracken, for their insightful questions and support during my graduate journey.

Along this journey, I have formed many wonderful and lasting friendships. Zach, you have been there from the very early years of my undergraduate journey, and you've stuck by my side through all the ups and downs. Your friendship has been the most supportive. I will forever be in your debt, and grateful for the many adventures, the laughs, and the times spent together. Thank you. Jonathan, Carly, Cody, Jeremy, and John, we share many great memories of our time in college; good food, good drinks, and overall good times. Thank you for your friendships, encouragement and support over these many years. And a very special thanks to Chris, for your kindness, support and friendship through my undergraduate years.

I have been fortunate to come across many amazing professors during my journey. A special thanks to Dr. Terrence Lee, Dr. Keying Ding, Dr. Norma Dunlap, Dr, Scott Handy, Dr. Anatoliy Volkov, Dr. Kevin Bicker, Dr. Bud Fischer and Professor Amy Pollock. for your support and encouragement in my academic pursuit.

Lastly, my parents, Wayne and Sylvia. The financial and logistical challenges never limited my potential, thanks to your sacrifices and love. I am truly grateful for your care and love. Without your support, this journey would never have been possible. Thank you. I hope that I have made you all proud.

The work featured in this dissertation was supported by the Photosynthetic Systems program of the Chemical Science, Geosciences, and Biosciences Division, Office of Basic Energy Sciences, Office of Science, U.S. Department of Energy under Award Number DE-SC0010847. Work in the laboratory of Harry Frank at the University of Connecticut was also supported by grants from the National Science Foundation (MCB-1243565) and the University of Connecticut Research Foundation. We thank Professor Roger Hiller (Macquarie University) for the generous gifts of the wild-type PCP samples and the expression construct for the N-terminal domain apoprotein of PCP that were required for the Chl *b* reconstitution procedure. We also thank Professor P. Gregory Van Patten (Middle Tennessee State University) for providing the CdSe QD samples.

TABLE OF CONTENTS

LIST OF TABLES

LIST OF TABLES

KEY TO ABBREVIATIONS

2DES, two-dimensional electronic spectroscopy

APC, allophycocyanin

ATP, adenosine triphosphate

BChl, bacteriochlorophyll

CCD, charge-coupled device

Chl, chlorophyll

CI, conical intersection

DART-MS, direct analysis in real time mass spectrometry

DDT, n-dodecanethiol

DEAE, diethylaminoethyl

DO, diffractive optic

EADS, evolution associated difference spectra

EET, excitation energy transfer

ESA, excited-state absorption

FFT, fast Fourier transform

FMO, Fenna−Matthews−Olson

FWHM, full-width half maximum

GSB, ground state bleaching

HDA, hexadecylamine

HP, hexadecyl palmitate

ICT, intramolecular charge transfer

LO, local oscillator

LPSVD, linear prediction singular value decomposition

MIIPS, multi-photon intrapulse interferometric phase scanning

NADPH, nicotinamide adenine dinucleotide phosphate

NMR, nuclear magnetic resonance

NOPA, noncollinear optical parametric amplifier

NTO, natural transition orbitals

OAcid, oleic acid

OAP, off-axis parabolic mirrors

OLA, oleylamine

PB, photobleaching

PBF, Poisson–Boltzmann finite difference

PBS, phycobilisome

PC, C-phycocyanin

PCP, peridinin–chlorophyll protein

PDB, protein data bank

PE, phycoerythrin

Per, peridinin

PSI, photosystem I

PSII, photosystem II

QDs, quantum dots

rPCP–Chl *b*, reconstituted peridinin–chlorophyll *b* protein

SE, stimulated emission

SHG, second harmonic

SLM, spatial light modulators

TA, transient absorption

TDDFT, time-dependent density functional theory

TEM, transmission electron microscopy

THG, third harmonic

TOP, trioctylphosphine

TOPO, trioctylphosphine oxide

TOPSe, trioctylphosphine selenide

WMEL, wave mixing energy level diagram

WL, white light continuum

wtPCP–Chl *a*, wild-type peridinin–chlorophyll *a* protein

Overview of the Dissertation

The purpose of my dissertation project is to address the involvement of vibronic coherence in excitation energy transfer and non-radiative relaxation processes in photosynthetic light-harvesting systems and nanomaterials. *Vibronic coherences* arise from quantum mechanical mixing of electronic and vibrational wavefunctions in strongly coupled systems. As one example, excitation energy transfer in light-harvesting proteins is apparently promoted by strong coupling of the skeletal vibrations and electronic states of the chromophores, which leads to the optical preparation of delocalized, molecular exciton states. Similarly, strong spatial confinement in colloidal nanoparticles enables strong coupling of core electronic states with the vibrations of surface-capping ligands, which can then mediate faster than expected hot carrier cooling transitions.

In my dissertation, we employed broadband two-dimensional electronic spectroscopy (2DES) to study excitation energy transfer between donor and acceptor states in two systems: the peridinin–chlorophyll protein from marine dinoflagellates, and CdSe quantum dots. Analysis of the temporal characteristics of the 2DES spectra allowed us to address the following specific aims:

1. Identify energy transfer pathways between carotenoids and chlorophylls in the peridinin–chlorophyll protein.
2. In the peridinin–chlorophyll protein, determine the mechanisms of energy transfer that are active between donor and acceptor chromophores and whether quantum coherence is involved.
3. Determine the involvement of nonadiabatic radiationless decay mechanisms in semiconductor quantum dots.

Chapter 1 presents a brief overview on light harvesting proteins and semiconductor quantum dots (QDs). The design and structure of light harvesting complexes are introduced, along with the current understanding of the energy transfer mechanisms present. The nonradiative relaxation process in semiconductor QDs is reviewed, and an alternate hypothesis is introduced based on the known structural properties of the materials. The vibronic exciton picture is then presented. This chapter concludes with a brief discussion on the method employed to study these systems.

Chapter 2 presents a background to broadband 2DES experiments performed previously in the Beck laboratory. We then review the third-order nonlinear responses before introducing a newly designed 2DES spectrometer, employing adaptive pulse shapers and a lock-in detection scheme. An overview of the implementation of the adaptive pulse shaping technique is addressed. This newly designed instrument was used for all experiments featured in this dissertation. The method of data acquisition and analysis are also reported.

Chapter 3 presents the results on the study of the excitation energy transfer pathways and mechanisms in the peridinin–chlorophyll *a* protein from marine dinoflagellates. In 2DES studies of excitation energy transfer in wild type PCP containing chlorophyll *a*, we employed 15 fs broadband pulses, photoseleting the main absorption band of the donor peridinin states. The results support previous studies performed in our laboratory of a branched energy transfer mechanism involving the S_2 and S_x states, facilitating coherent and incoherent mechanisms described in the earlier work. The experiment also revealed peridinin to peridinin energy transfer, whereby lower energy peridinins serve as an intermediate state to the chlorophyll acceptor. Furthermore, we observe the production of chlorophyll polarons by the coherent energy transfer from the optically excited peridinin exciton states in the system. These are localized,

self-trapped chlorophyll excited states exhibiting enhanced coupling to the surroundings. Evidence for the formation of polarons are presented in the time evolution of the off-diagonal cross-peak accompanied by oscillatory amplitudes. Analysis of the frequencies of these oscillations reveal a principal modulation component of 570 cm^{-1}, attributed to the torsional motion of the peridinin's polyene backbone. Additionally, the damping time is an intermediate of the timescales observed for electronic decoherence (<20 fs) and pure vibrational decoherence (<500 fs). These findings are extremely important as it implicates the vibrations of the localized product of coherent energy transfer as a possible explanation for long-lived quantum beating observed in light-harvesting systems.

Chapter 4 of my dissertation focuses on mechanisms of nonradiative relaxation of hot carriers in CdSe quantum dots. In particular, we hypothesize the involvement of vibronic coherence results from the mixing of core electronic states with that of vibrational states from organic surface ligands. We present the first evidence for vibronic coherences in CdSe quantum dots capped with different organic ligands in experiments using 2DES with broadband pulses covering the lowest three exciton states. Results from the 2DES experiments support previous studies of hot carrier cooling in QDs, where an Auger-like mechanism promotes rapid nonradiative relaxation of the hot-carrier exciton to the band-edge. However, our findings reveal strongly modulated, rapidly damped oscillations at short time, observed at the initial and final state coordinates in the 2DES spectra. Fourier transformation analysis of the modulations unveils frequency components much higher than lattice vibrational modes. The highest frequency and most rapidly damped modulation components of 700 cm^{-1} and 980 cm^{-1} are in range for NH_2-bending and out-of-plane motions of the alkyl backbone of amine capping ligands. The findings

of this work can lead to significant advancements of QD-based photovoltaic cells and photocatalysis applications.

Chapter 5 presents preliminary data on excitation energy transfer in phycobilisomes. This chapter highlights the future work planned following the findings reported in Chapters 3 and 4.

The work featured in this dissertation identifies the role of vibronic coherences in the peridinin–chlorophyll protein, demonstrating a nonadiabatic energy transfer mechanism resulting from the quantum mechanical wave mixing of electronic and vibrational states. Here, we also report the first observation of vibronic coherences in colloidal semiconductor quantum dots, involving core electronic levels and vibrational states of organic capping ligands. The vibronic coherences present in QDs significantly impacts the hot carrier cooling rates of the system. Preliminary findings in intact phycobilisomes are also reported, as the future direction of the project. These studies can lead to significant advancements in the development of efficient photovoltaic devices, photocatalytic and quantum information applications.

Chapter 1: Introduction to Light Harvesting Proteins and Semiconductor Quantum Dots

Light harvesting in photosynthesis involves complex systems of highly ordered arrays of chromophores, resulting in extremely high energy transfer efficiencies. The structure and interaction of chromophores within these systems allow for extensive delocalization. Another system that exhibits similar extensive delocalization is a quantum confined nanocrystal, in particular, a quantum dot (QD). This chapter will cover the background of structure and energy transfer in light harvesting proteins, along with a review of work on the peridinin–chlorophyll protein complex (PCP) to date. This chapter will also feature a background to semiconductor quantum dots and the nonradiative relaxation of hot carriers. Finally, we will present our hypothesis and approach to identifying and understanding the role of vibronic coherence in the energy transfer and nonradiative processes.

1.1 Light Harvesting in Photosynthesis: An Overview

Photosynthetic light-harvesting is a membrane-based biological process involving the capture of solar photons and subsequent energy conversion used to support life in natural organisms. The process of photosynthesis begins with light-harvesting proteins which capture solar photons, and transfer the energy to the reaction center through a channel of excitation energy transfer (EET) pathways. The excitation energy undergoes energetic and spatial transfer across electronically coupled chromophores, where the electron is transferred to a lower energy acceptor in a downhill cascade to separate the charges across the membrane. Finally, the electron involved in the EET process is stabilized by the formation of chemical bonds in molecules such as adenosine triphosphate (ATP) and nicotinamide adenine dinucleotide phosphate (NADPH). At this stage of the process, the molecules can then form stable sugars to support many cellular functions necessary for the organisms' survival.[1]

Photosynthetic organisms are known to thrive in environments with vastly different environmental conditions. Therefore, through evolutionary processes, these organisms have adapted and developed light-harvesting antennae capable of extremely high efficiencies. The complexes employed by these organisms contain a variety of pigments capable of harvesting an abundance of solar radiation. The experiments in this dissertation will focus mainly on a protein complex containing carotenoids and chlorophylls. The work features an extension to previous work completed in the Beck laboratory.[2]

1.2 Light Harvesting Complexes

Over the last few decades, the study of EET in light harvesting complexes have been of considerable interest. Particular advancements made in the understanding of the structure of different types of photosynthetic light harvesting complexes through high-resolution X-ray crystallography. Combined with ultrafast spectroscopic techniques, EET processes have been identified in some of the most commonly studied light harvesting complexes, such the Fenna-Matthews-Olson complex (FMO),[3–7] the light harvesting complex II (LH2),[8–12], and the peridinin–chlorophyll protein complex (PCP).[13–16] In general, a light harvesting antenna system is comprised of three main components: the harvester, the mediator, and the reaction center (RC). The light harvester serves to capture as many solar photons as possible in efforts to increase the probability of successful energy transfer to the RC. The mediator aids in the EET process from peripheral complexes to integral light harvesting proteins or RCs. Finally, the RC converts the transferred energy into an electrochemical potential gradient. While the RC can capture photons directly, the harvesters and mediators serve to enhance the number of possible excitations that arrive at the RC. The complex structures are designed in nature to increase the efficiency of EET through optimized energetic and spatial arrangements.

1.2.1 Energy Transfer Mechanisms in Light Harvesting Complexes

The excitation energy transfer process in light harvesting systems has been of great interest over the last few decades. These systems are extremely efficient in their EET, with LH2 exhibiting an efficiency of 70%,[17] and PCP at 90%.[18,19] A deep understanding of the mechanisms involved in EET in light harvesting complexes can lead to significant advancements in the design and implementation of materials in photovoltaic cells and photocatalytic applications.

The efficiency of energy transfer between chromophores is strongly influenced by the strength of the interaction, which is determined by the orientation and distance between the electric dipoles of the involved chromophores. The strength of the interaction can determine the mechanism employed by the chromophores. For example, excitation energy can hop from chromophore to chromophore in an incoherent process, or it can exhibit a wavelike character involving delocalized excitons over serval chromophores (quantum coherence).

In the case of weakly coupled chromophores (that is, chromophores that interact more with the solvent that one another), then the incoherent energy transfer process is implemented. Weakly coupled chromophores are considered to have localized wavefunctions of electron densities, which is evident by comparing their absorption spectra in solution against the absorption spectrum in a coupled complex. If there are no apparent differences between the spectra, we can conclude the chromophores are in the weakly coupled regime. Therefore, the Förster energy transfer mechanism[20] can be used to describe the incoherent EET. This mechanism requires the emission spectrum of the donor chromophore to be resonant with the absorption spectrum of the acceptor chromophore. The energy is transferred from donor to acceptor nonradiatively, through transition dipole-transition dipole interactions.

Chromophores in the intermediate to strongly coupled regime (where the chromophores interact more strongly with each other than the solvent) may exhibit wavefunction mixing, forming delocalized wavefunctions across multiple chromophores. Strongly coupled systems exhibit splitting of the energy states of the chromophores, resulting in shifts in the absorption spectrum. Such effect was evident in studies of mutated LH2 complex, where B800 chlorophylls were removed from the complex, but circular dichroism experiments revealed strong features at 700 nm.[21] This result is attributed to the collective excitation and exciton formation from strongly coupled B850 chlorophylls.

The extent of chromophore to chromophore coupling and chromophore to solvent coupling determines what type of interaction is present in the system. Quantum mechanical mixing of the chromophores' wavefunction requires stronger chromophore to chromophore interaction than chromophore to surrounding interactions. Therefore, photosynthetic organisms employ complex designs involving chromophore clusters bound by protein, increasing chromophore to chromophore interactions, and enhancing EET efficiencies. A more detailed review of quantum coherent energy transfer is covered in previous work in the Beck laboratory.[2]

The exact nature of carotenoid and chlorophyll interactions in light harvesting and the involvement of coherent energy transfer remain inconclusive. The following section will cover the current understanding of carotenoid to chlorophyll energy transfer in the peridinin–chlorophyll protein complex, and highlight unresolved questions regarding the EET process.

1.3 Peridinin–Chlorophyll Protein

The peridinin–chlorophyll protein complex (PCP) is a water-soluble, trimeric complex found in marine dinoflagellates. Unlike most light-harvesting complexes, PCP contains more carotenoids than chlorophylls (Chls) (Figure 1.1a,b). Marine dinoflagellates reside on the

sedimentary surface of shallow bodies of water, and are therefore exposed to less of the solar spectrum. Peridinin (Figure 1.1c), a ketocarotenoid, serves as the principal mid-visible chromophore, increasing absorption in a region where chlorophyll falls short (470-570 nm). X-ray crystallography of PCP from *Amphidinium carters* (1PPR.pdb) reveals a trimer. Each subunit of PCP consists of a of α helices bound in a dense cluster of eight peridinin carotenoids and two Chl *a* chromophores in a C_2-symmetric, two-domain assembly. The two Chl *a* molecules are approximately 17 Å apart. In contrast, the four peridinins in each domain are effectively in van der Waals contact (3.3 to 3.8 Å separation) with a central Chl a acceptor.[22] This highly-ordered crystal-like structure results in high excitation energy transfer (EET) efficiency. The principle chromophore, peridinin, captures solar photons and transfers excitation energy to chlorophylls via different mechanisms. These mechanisms are a major focus of this dissertation.

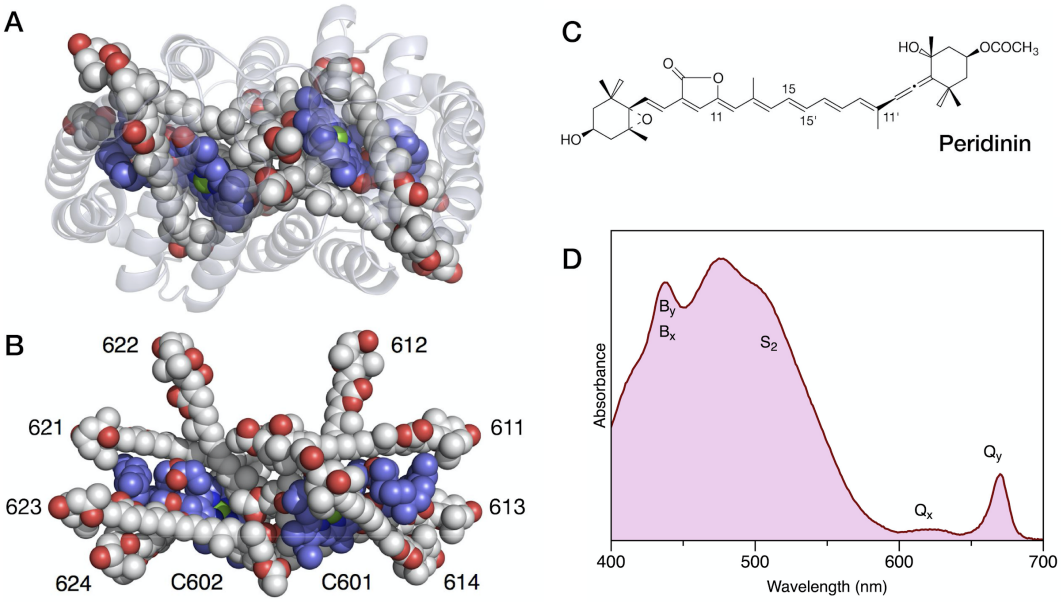

Figure 1.1. Structure of PCP from *Amphidinium carterae* (1PPR): (a) Bottom view, along the two-fold symmetry axis for a single subunit. (b) Peridinin–Chl *a* chromophore cluster only, with the symmetry axis oriented vertically. (c) Structure of peridinin. (d) Absorption spectrum of PCP (red), showing Chl *a* transitions (B_x, B_y, Q_x, Q_y) and peridinin S_2 transition.

1.3.1 Energy Transfer in Peridinin–Chlorophyll Protein

Peridinin carotenoids serve as the light-harvesting donor chromophores in PCP, with very strong transitions from S_0 (1^1A_g-) state to the S_2 (1^1B_u+) state; Chl serves as the terminal emitter. The mechanisms of excitation energy transfer (EET) from peridinins to Chl *a* result in a total quantum yield which approaches 90%, notably one of the highest efficiencies in carotenoid-containing light-harvesting complexes.[18] Because the S_2 state lies above the Q_x excited state of Chl, a Förster resonant dipole-dipole mechanism is energetically favorable from S_2 to Q_x.[20,23] However, studies have established that the energy transfer pathway competes with the nonradiative relaxation, where population in the S_2 state is depleted rapidly (<100 fs).[24–33] The nonradiative pathway continues as the S_1 state decays into the S_0 state. The S_1 state, however, is characterized as a 'dark' state, as the transition from S_0 to S_1 is symmetry forbidden.[34] Additionally, the fluorescence quantum yield from the S_1 state is extremely weak, suggesting that

the dipole strength of the S_1 state is very small.[35–47] With a very small dipole strength, the S_1 state would be unlikely to conduct efficient energy transfer to the Chl Q_y acceptor, as the dipole strength integral overlap would be quite small. However, carotenoids, including peridinin, exhibit intramolecular charge transfer (ICT) character,[33,48–58] which may facilitate in the EET to the Chl acceptor. In this process, the donor state for energy transfer was assigned to a form of the S_1 state of peridinin with intramolecular charge-transfer (ICT) character from the carbonyl-substituted γ-lactone ring at one end of the conjugated polyene backbone.[51,59–61] Many studies have attempted to incorporate this ICT character into the EET process. In early studies, it was suggested that the S_1 state simply propagates along the ICT coordinate, linking the diabatic S_1 and ICT states.[48,49,55,56] Another approach suggests a quantum mechanically mixing of the states.[52,62] In either scenario, the model relies simply on the increase in the dipole strength of S_1 through the ICT character. Lastly, another hypothesis suggests that the S_1 and ICT states are the same state, arising from a quantum mechanical mixing of the S_1 and S_2 states.[60] Nevertheless, any energy transfer originating from the S_1 state would require an increase in its dipole strength. Early studies on PCP employed femtosecond pump-probe measurements with 100 fs pulses and were only able to detect incoherent energy transfer pathways via the Förster mechanism from the peridinins to the Chl *a* acceptor with a 2.3–3.2 ps time constant.[13,15,51,59,63,64]

A much faster energy transfer process (<50 fs) was suggested to account for a small fraction of the total yield, involving an unrelaxed S_2 state of peridinin as the donor via a coherent mechanism.[13,15,51,59,63,64] Previous studies in the Beck laboratory definitively establish that the Franck–Condon and twisted (S_x) conformations of peridinin in the S_2 state are the donor states, respectively, for coherent and incoherent energy transfer channels. The coherent mechanism accounts for at least two thirds of the yield.[2,65–67] These studies featured increased time resolution

through broadband excitation, as well as global models and numerical simulations. However, these studies focused mainly on the lower-energy transitions in the peridinin absorption region. Therefore, questions regarding the energy transfer pathway and mechanisms from higher energy peridinin molecules in PCP remain open.

1.4 Semiconductor Quantum Dots

Colloidal semiconductor quantum dots (QDs)[68–71] are nanomaterials commonly composed of type II-VI materials, that exhibit tunable electronic properties dependent on size, shape, and composition. The sensitivity to size and shape alterations arises from a strong spatial confinement of the electronic wavefunctions, resulting in discrete energy levels and an interband gap that is tunable across the solar spectrum.[69]

Similar to bulk semiconductors, the electronic structure of QDs can be described in terms of a conduction band and valence band. At room temperature, the valence band is populated in the ground state by a distribution of electrons, while the conduction band remains vacant. The energy difference between the highest occupied level in the valence band (HOMO) and the lowest level of the conduction band (LUMO) is defined as the *energy band-gap*. This band-gap varies with size, shape, composition, and crystal structure of the QD.

The electronic structure of a QD can be described by investigating the confinement regime and the effective mass of the electron and hole.[71,72] When a QD is confined to a radius much smaller than the Bohr exciton radius for the material ($a << a_B$), the QD is defined as strongly confined. Unlike the weak confinement regime ($a >> a_B$), the quantization energy of both electron and hole is larger than the Coulomb interaction. Therefore, the optical spectra describe transitions between electron and hole quantum-sized levels. The simplest model can describe these energy levels with the multi-band effective mass approximation. The model accounts for

the effective masses of the electron and hole independently, while the selection rules govern only transitions between levels with the same quantum number. In strongly confined QDs, the valence band contains a higher density of states when compared to the conduction band, which introduces complexities in describing the hole levels of a QD. Experimental results from absorption spectra,[73] photoluminescence excitation,[74] and hole burning experiments[75] have been used to describe the valence band quantitatively. Figure 1.2 below illustrates the general electronic structure of CdSe QDs featured in the experiments in this dissertation. The QDs were colloidal, and therefore capped with organic surface ligands. Each state is assigned a principal quantum number (1,2), angular momentum (S, P, D), and total angular momentum (1/2, 3/2).

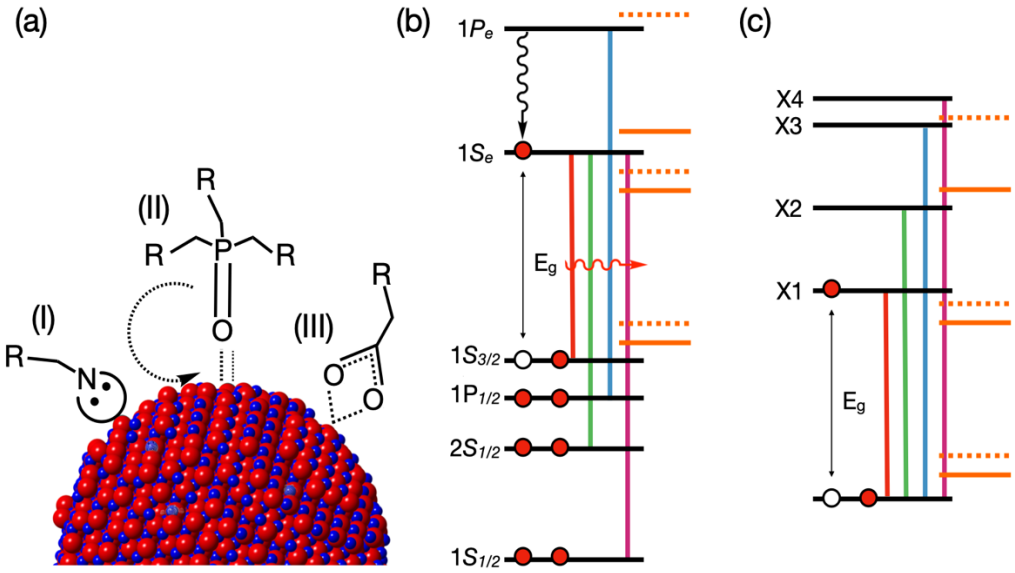

Figure 1.2. Examples of surface capping ligands and possible coupling of core electronic states in QDs with ligand vibrations, after Lifshitz.[76] (a) Alkylamine (I), trioctylphosphineoxide (TOPO, II), and alkylcarboxyl (III) ligands and ligation to metal cation (e.g. Cd^{2+}) and anion (chalcogen, e.g. Se^{2-}) sites, with R representing alkane or alkene substituents. (b) Coupling of core QD electronic (black) states and ligand bonding (solid red) and antibonding (dashed red) states. (c) Exciton manifold for the first four bound electron-hole pairs formed upon excitation, labeled X1 through X4.

The potential application of QDs is wide-ranging. In addition to being of interest for their photoluminescent properties[77] and as laser gain media,[78–80] they are potentially useful as mid-visible light-harvesting structures in photocatalysis applications.[81,82] Unfortunately, they perform efficiently in such applications because of rapid excitation energy relaxation mechanisms. In particular, hot carrier cooling exhibits an ultrafast nonradiative relaxation process mediated by an Auger mechanism. [83–87] The role of surface trapping states and organic capping ligands in hot carrier cooling is under current investigation.[88–91] One hypothesis implicates the vibrations of surface ligands merely as classical promoting (or bath) modes, which would accept the excess energy of the donor state in an incoherent energy transfer mechanism.[76,89–91]

1.4.1 Hot Carrier Dynamics in Quantum Dots

The production of nanoscale semiconductors using strongly confined QDs leads to the expectation that the photoexcited exciton states would have longer exciton lifetimes (>100 ps) when compared to bulk semiconductors (<20 ps),[92] which would favor their use in photovoltaic cells over bulk semiconductors. The energy level spacing due to lattice vibrations (phonon modes) in CdSe QDs is 30 meV (240 cm-1), whereas the intraband spacings are four to ten times as large,[93–95] which anticipates a multiphonon process for energy dissipation. Contradictory to this prediction, fast hot carrier cooling occurs via an Auger-like mechanism, in which a photoexcited electron in the conduction band transfers the excess energy above the band edge to a hole in the valence band with the higher state density.[83,87] The Auger-like mechanism involves a Coulombic attraction between the electron and the hole. The lighter mass electron can transfer energy to the hole with a higher mass and state density, allowing the electron to occupy the conduction band edge while the holes non-radiatively dissipate the excess energy through a multiphonon process. The time constants for hot carrier cooling are usually in the sub-

picosecond regime.[84,96–99] In conflict with this picture, the relaxation rate for the hole back up to the valence band edge is increased for smaller quantum dots and in the presence of nucleophilic surface ligands. These findings strongly implicate nonadiabatic transitions involving coupled vibrations of the surface ligands as a dominant mechanism for hole relaxation.[97,98,100,101]

In an effort to slow the rate of exciton relaxation and to enable extraction of the "hot" electron for use in photovoltaic cells, suppression of the Auger channel has been explored. By isolating the hole to the surface of the QD, the magnitude of the Coulombic coupling strength of the electron-hole pair can be reduced.[86,97,100,101]

Synthetic advancements have made it possible to vary the rate of exciton relaxation by changing the surface ligands. The large surface/volume ratio and the strong spatial confinement of the electronic wavefunction causes many of the properties of QDs to be quite sensitive to the presence of surface (lone pair, hole trapping) states, making it possible to use ligands to obtain electronic passivation,[102–105] exciton decoupling,[86,88,89,100,106] and particle shape reconstruction.[107] The presence of surface ligands has a considerable impact on the electrical conductivity of films of QDs[108,109] by introducing mid-band-gap states that trap carriers at the surface,[88,110–115] which increases the strength of interactions with the surroundings and between QDs.[116,117]

Accordingly, recent investigations have led to synthetic advancements that make it possible to vary the rate of exciton relaxation by controlling the nature of the surface ligands.[110] Guyot-Sionnest and coworkers observed that certain surface ligands lengthen carrier cooling times.[89] The four most common surface ligands for CdSe QDs were included: oleic acid (OAcid), oleylamine (OLA), n-dodecanethiol (DDT), and trioctylphosphine/trioctylphosphine oxide (TOP/TOPO). DDT-capped QDs exhibited the slowest relaxation time, ~18 ps, while TOP/TOPO mixtures exhibited a faster relaxation time, ~6 ps. One approach to explain these

observations would be to assume an electronic mechanism, involving charge transfer to a surface state. The trend would be expected to be consistent with hard-soft acid-base theory; softer ligands (thiols and amines in this case) and increased covalency to the surface metal ions would accompany slower relaxation times.[118] However, such a mechanism should also exhibit a temperature dependence, which has not been observed.[88] This conflict leaves open the possibility that the ligands serve either as incoherent or coherent energy transfer acceptors, as recently reviewed.[76] Given the considerable advances that have been made since the work of Guyot-Sionnest and coworkers in characterizing and controlling the surface ligands in QDs,[119–123] there is an opportunity now to understand with far better detail how the ligands take part in the electronic structure of QDs and how they impact the exciton relaxation and photoluminescence properties.

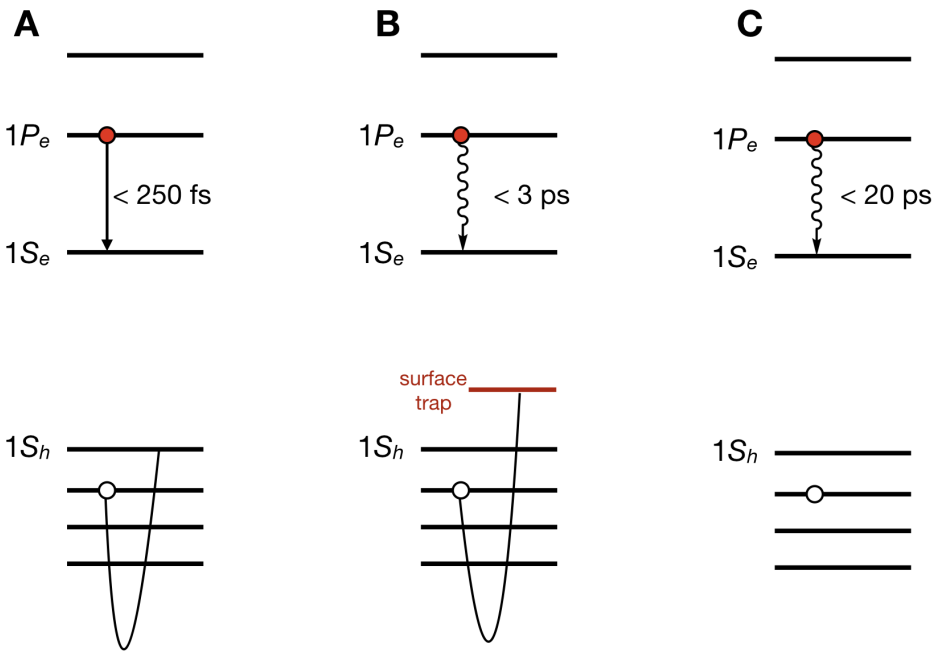

Figure 1.3. Exciton relaxation pathways in QDs. (a) Auger-like recombination involving energy transfer from electron to hole results in exciton lifetimes <250 fs.[99] (b) Surface trapping of hole reduces the Auger mechanism, resulting in exciton lifetimes of <3 ps.[86] (c) Ligand mediated relaxation increases exciton relaxation to ~20 ps.[90]

1.4.2 Organic capping ligands

As reviewed recently by Owen,[124] three ligand types (Figure 1.4) have been identified on the surface of QDs by determining how an exchange of ligands alters the photoluminescence quantum yield[125–127] due to the introduction of mid-gap, surface-trapping states. These types are labeled using Green's Covalent Bond Classification (CBC) method for transition metals.[128,129] L-type ligands are Lewis bases such as amines or phosphines that coordinate as neutral, two-electron donors to the divalent metal cations (for example, Cd^{2+}) on a QD's surface. More prevalent, however, are the X-type ligands, which are anions such as carboxylates or phosphonates that coordinate as one-electron Lewis bases. Two X-type ligands can coordinate to a divalent metal cation on the surface of a QD.[119] As the size of a QD increases, however, it increasingly deviates from the 1:1 stoichiometry of the bulk semiconductor lattice by adding an encapsulating monolayer of metal cations.[130] X-type ligands can also bind to these metal cations, effectively serving as counterions for the overall positive charge of the QDs.[119] The surface monolayer of divalent metal cations is labile; L-type ligands can reversibly displace them coordinated with a pair of X-type ligands. These neutral MX2 complexes are termed Z-type ligands because they act as two-electron acceptors that bind to an exposed chalcogen anion (for example, Se^{2-}) site.[121]

The three ligand types would be expected to exhibit different strengths of coupling of their vibrational modes to the core electronic wavefunction of the QD. The strongest interactions would be expected with the L- or X-type ligands when they are directly coordinated to the stoichiometric core in contact with the delocalized electron density of the QD. Very weak couplings would arise for the X-type ligands when coordinated to the monolayer of metal cations

as a Z-type ligand, however, because these metal cations are not strongly coupled to the core electronic structure, as judged by their not having a significant impact on the band gap.[121,131]

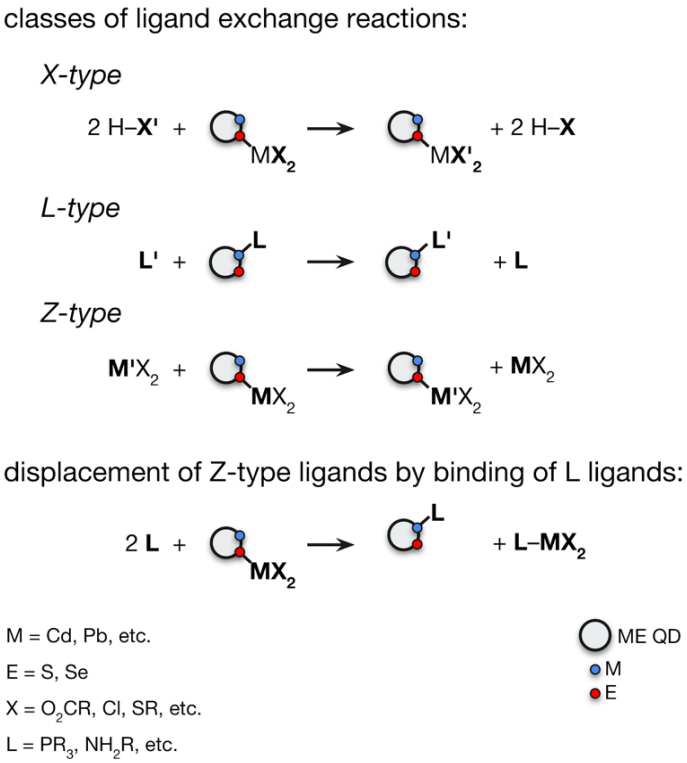

Figure 1.4. Ligand types for QDs based on their ligand exchange chemistry. After Anderson et al.[121]

1.4.3 Vibronic Coherence Hypothesis

The above summary of what is known about hot carrier cooling dynamics in QDs is based predominantly on information from picosecond time-resolved fluorescence and femtosecond pump–probe transient absorption spectroscopy, the latter typically with ~100 fs time resolution.[84–86,88,96,100,106] Opportunities for new discoveries with 2DES in studies of QDs and in other semiconductor materials such as quantum wells were reviewed recently by Cassette et al.[132] and Li and Cundiff,[133] respectively. From the perspective of the planned work, 2DES[134–136] affords several key advantages over conventional femtosecond pump–probe spectroscopy. Pathways of exciton relaxation can be determined from the time evolution of the 2DES spectrum in terms of off-diagonal cross peaks, which correlate the excitation and detection transitions.[137]

Quantum beating and excited-state absorption transitions to multiple quantum states reveal the initial presence and decay over time of quantum coherence.[138] Many of these advantages have been illustrated by the initial studies on QDs using 2DES. The ability to resolve the fine structure due to single and biexciton excitations despite the presence of extensive inhomogeneous line broadening due to size and shape polydispersity was demonstrated in CdSe QDs by Wong and Scholes[139–141] and in PbS QDs by Engel and coworkers.[142] In addition to observing hot carrier cooling in CdSe QDs using off-diagonal cross peaks,[143] Engel and coworkers detected quantum beating between exciton electronic levels and vibronic coherence arising from electron-phonon coupling.[144] The same group subsequently demonstrated the ability to observe size and state-dependent exciton relaxation dynamics while also resolving surface trap and biexciton features.[145]

1.5 Hypothesis and proposed work

The established findings of quantum coherent energy transfer in PCP from previous studies[2,66,67] has sparked further interest in the fundamentals of the EET pathway. The previous studies have led to the hypothesis of a *nonadiabatic mechanism* for EET, involving *vibronic coherence*. Nonadiabatic mechanisms, as identified in previous studies,[146–149] involve concerted vibrational and electronic motion in light harvesting systems in the intermediate coupling regime. Extensive delocalization across the chromophore cluster and EET rate can be significantly enhanced by vibronic resonance, where the vibrational quanta of the included chromophore match the gaps between exciton energy levels, as identified in previous studies.[150–155]

In an effort to understand the underlying mechanism and identify the presence of vibronic coherences in PCP and colloidal QDs, we employed broadband 2DESS with ultrashort

broadband pulses with the ability to optically excite and follow the EET pathway. Experiments were performed on wild type PCP containing Chl *a*, and a reconstituted variant that replaces the terminal emitter with Chl *b*. This change allowed us to vary the energy gap between donor and acceptor, and identify donor specific mechanisms. Experiments were also performed on CdSe QDs, with varied particle sizes and ligand composition, allowing us to vary the vibronic resonance and characterize potential inter-excitonic electronic coherences. The main questions addressed in this dissertation are:

1) Identify energy transfer pathways between carotenoids and chlorophylls in the peridinin–chlorophyll protein.
2) In the peridinin–chlorophyll protein, determine the mechanisms of energy transfer that are active between donor and acceptor chromophores and whether quantum coherence is involved.
3) Determine the involvement of vibronic coherences in radiationless decay mechanisms in semiconductor quantum dots.

As discussed earlier, many studies on PCP[15,18,51,64] and QDs[79,84,86–90,100,106] were conducted with ultrafast (~100 fs pulses) transient absorption (TA) spectroscopy. The employment of 2DES, however, provides several key advantages over transitional TA spectroscopy. Firstly, broadband pulses are compressed the transform limit pulse durations as short as 6.5 fs, resulting in a significant increase in time resolution capable of extracting high-frequency oscillations from vibronic coherences as well as monitoring ultrafast (<50 fs) EET processes. Secondly, the second axis of the 2DES experiment provides the excitation frequency resolution necessary to identify optically prepared chromophores. This allows one to correlate excited events with detected responses. Lastly, and arguably most important for systems such as QDs, is the ability to

improve the resolution of congested spectral lineshapes resulting from inhomogeneous line broadening from random energy fluctuations in the environment or system. In the next chapter of this dissertation, the theory and execution of 2DES will be discussed, along with the introduction of a newly designed instrument employed in the experiments presented.

REFERENCES

REFERENCES

(1) Blankenship, R. E. *Molecular Mechanisms of Photosynthesis*; John Wiley & Sons, 2014.

(2) Roscioli, J. D. Detection of Coherent Energy Transfer Pathways in Photosynthesis with Two-Dimensional Electronic Spectroscopy. Chemistry - Doctor of Philosophy, Michigan State University, 2018.

(3) Brixner, T.; Stenger, J.; Vaswani, H. M.; Cho, M.; Blankenship, R. E.; Fleming, G. R. Two-Dimensional Spectroscopy of Electronic Couplings in Photosynthesis. *Nature* **2005**, *434* (7033), 625–628.

(4) Engel, G. S.; Calhoun, T. R.; Read, E. L.; Ahn, T. K.; Mančal, T.; Cheng, Y. C.; Blankenship, R. E.; Fleming, G. R. Evidence for Wavelike Energy Transfer through Quantum Coherence in Photosynthetic Systems. *Nature* **2007**, *446*, 782–786.

(5) Cheng, Y.-C.; Fleming, G. R. Dynamics of Light Harvesting in Photosynthesis. *Annu. Rev. Phys. Chem.* **2009**, *60*, 241–262.

(6) Hayes, D.; Engel, G. S. Extracting the Excitonic Hamiltonian of the Fenna-Matthews-Olson Complex Using Three-Dimensional Third-Order Electronic Spectroscopy. *Biophys. J.* **2011**, *100* (8), 2043–2052.

(7) Fransted, K. A.; Caram, J. R.; Hayes, D.; Engel, G. S. Two-Dimensional Electronic Spectroscopy of Bacteriochlorophyll *a* in Solution: Elucidating the Coherence Dynamics of the Fenna-Matthews-Olson Complex Using Its Chromophore as a Control. *J. Chem. Phys.* **2012**, *137*, 125101.

(8) Papiz, M. Z.; Prince, S. M.; Hawthornthwaite-Lawless, A. M.; McDermott, G.; Freer, A. A.; Isaacs, N. W.; Cogdell, R. J. A Model for the Photosynthetic Apparatus of Purple Bacteria. *Trends Plant Sci.* **1996**, *1* (6), 198–206.

(9) Krueger, B. P.; Scholes, G. D.; Fleming, G. R. Calculation of Couplings and Energy-Transfer Pathways between the Pigments of LH2 by the Ab Initio Transition Density Cube Method. *J. Phys. Chem. B* **1998**, *102* (27), 5378–5386.

(10) Polli, D.; Cerullo, G.; Lanzani, G.; De Silvestri, S.; Hashimoto, H.; Cogdell, R. J. Carotenoid-Bacteriochlorophyll Energy Transfer in LH2 Complexes Studied with 10-Fs Time Resolution. *Biophys. J.* **2006**, *90* (7), 2486–2497.

(11) Wormit, M.; Harbach, P. H. P.; Mewes, J. M.; Amarie, S.; Wachtveitl, J.; Dreuw, A. Excitation Energy Transfer and Carotenoid Radical Cation Formation in Light Harvesting complexes—A Theoretical Perspective. *Biochimica et Biophysica Acta (BBA)-Bioenergetics* **2009**, *1787* (6), 738–746.

(12) Ostroumov, E. E.; Mulvaney, R. M.; Anna, J. M.; Cogdell, R. J.; Scholes, G. D. Energy Transfer Pathways in Light-Harvesting Complexes of Purple Bacteria as Revealed by

Global Kinetic Analysis of Two-Dimensional Transient Spectra. *J. Phys. Chem. B* **2013**, *117* (38), 11349–11362.

(13) Kleima, F. J.; Hofmann, E.; Gobets, B.; van Stokkum, I. H.; van Grondelle, R.; Diederichs, K.; van Amerongen, H. Förster Excitation Energy Transfer in Peridinin-Chlorophyll-*a*-Protein. *Biophys. J.* **2000**, *78* (1), 344–353.

(14) Damjanović, A.; Ritz, T.; Schulten, K. Excitation Transfer in the Peridinin-Chlorophyll-Protein of *Amphidinium Carterae*. *Biophys. J.* **2000**, *79* (4), 1695–1705.

(15) Krueger, B. P.; Lampoura, S. S.; van Stokkum, I. H.; Papagiannakis, E.; Salverda, J. M.; Gradinaru, C. C.; Rutkauskas, D.; Hiller, R. G.; van Grondelle, R. Energy Transfer in the Peridinin Chlorophyll-*a* Protein of *Amphidinium Carterae* studied by Polarized Transient Absorption and Target Analysis. *Biophys. J.* **2001**, *80* (6), 2843–2855.

(16) Niedzwiedzki, D. M.; Jiang, J.; Lo, C. S.; Blankenship, R. E. Low-Temperature Spectroscopic Properties of the Peridinin–chlorophyll *a*–protein (PCP) Complex from the Coral Symbiotic Dinoflagellate *Symbiodinium*. *J. Phys. Chem. B* **2013**, 11091–11099.

(17) Krueger, B. P.; Scholes, G. D.; Gould, I. R.; Fleming, G. R. Carotenoid-Mediated B800-B850 Coupling in LH2. *Phys. Chem. Comm.* **1999**, *2*, 34–40.

(18) Bautista, J. A.; Hiller, R. G.; Sharples, F. P.; Gosztola, D.; Wasielewski, M.; Frank, H. A. Singlet and Triplet Energy Transfer in the Peridinin-Chlorophyll *a*-Protein from *Amphidinium Carterae*. *J. Phys. Chem. A* **1999**, *103* (14), 2267–2273.

(19) Damjanović, A.; Ritz, T.; Schulten, K. Energy Transfer between Carotenoids and Bacteriochlorophylls in Light-Harvesting Complex II of Purple Bacteria. *Phys. Rev. E* **1999**, *59*, 3293–3311.

(20) Förster, T. Zwischenmolekulare Energiewanderung Und Fluoreszenz. *Annu. Physik* **1948**, *2*, 55–75.

(21) Koolhaas, M. H. C.; Frese, R. N.; Fowler, G. J. S.; Bibby, T. S.; Georgakopoulou, S.; van der Zwan, G.; Hunter, C. N.; van Grondelle, R. Identification of the Upper Exciton Component of the B850 Bacteriochlorophylls of the LH2 Antenna Complex, Using a B800-Free Mutant of *Rhodobacter Sphaeroides*. *Biochemistry* **1998**, *37*, 4693–4698.

(22) Hofmann, E.; Wrench, P. M.; Sharples, F. P.; Hiller, R. G.; Welte, W.; Diederichs, K. Structural Basis of Light Harvesting by Carotenoids: Peridinin-Chlorophyll-Protein from *Amphidinium Carterae*. *Science* **1996**, *272* (5269), 1788–1791.

(23) Förster, T. Intermolecular Energy Transfer and Fluorescence. *Annu. Phys.* **1968**, *2*, 55–75.

(24) Cherry, R. J.; Chapman, D.; Langelaar, J. Fluorescence and Phosphorescence of β-Carotene. *Trans. Faraday Soc.* **1968**, *64*, 2304–2307.

(25) van Riel, M.; Kleinen-Hammans, J.; van de Ven, M.; Verwer, W.; Levine, Y. Fluorescence Excitation Profiles of β-Carotene in Solution and in Lipid/water Mixtures. *Biochem. Biophys. Res. Commun.* **1983**, *113*, 102–107.

(26) Haley, L. V.; Koningstein, J. A. Space and Time-Resolved Resonance-Enhanced Vibrational Raman Spectroscopy from Femtosecond-Lived Singlet Excited State of β-Carotene. *Chem. Phys.* **1983**, *77*, 1–9.

(27) Watanabe, J.; Kinoshita, S.; Kushida, T. Non-Motional Narrowing Effect in Excitation Profiles of Second-Order Optical Processes: Comparison between Stochastic Theory and Experiments in β-Carotene. *Chem. Phys. Lett.* **1986**, *126*, 197–200.

(28) Bondarev, S. L.; Dvornikov, S. S.; Bachilo, S. M. Fluorescence of β-Carotene at 77 and 4.2 K. *Opt. Spectrosc.* **1988**, *64*, 268–270.

(29) Gillbro, T.; Cogdell, R. J. Carotenoid Fluorescence. *Chem. Phys. Lett.* **1989**, *158* (3-4), 312–316.

(30) Koyama, Y.; Kuki, M.; Andersson, P. O.; Gillbro, T. Singlet Excited States and the Light-Harvesting Function of Carotenoids in Bacterial Photosynthesis. *Photochem. Photobiol.* **1996**, *63* (3), 243–256.

(31) Frank, H. A.; Young, A. J.; Britton, G.; Cogdell, R. J. The Photochemistry of Carotenoids. In *Advances in Photosynthesis*; Govindjee, Ed.; Kluwer Academic Publishers: Dordrecht, 1999.

(32) Christensen, R. L. The Photochemistry of Carotenoids. *Frank, HA* **1999**, 137–159.

(33) Frank, H. A.; Bautista, J. A.; Josue, J.; Pendon, Z.; Hiller, R. G.; Sharples, F. P.; Gosztola, D.; Wasielewski, M. R. Effect of the Solvent Environment on the Spectroscopic Properties and Dynamics of the Lowest Excited States of Carotenoids. *J. Phys. Chem. B* **2000**, *104* (18), 4569–4577.

(34) Birge, R. R. Two Photon Spectroscopy of Protein-Bound Chromophores. *Acc. Chem. Res.* **1986**, *19*, 138–146.

(35) Cosgrove, S. A.; Guite, M. A.; Burnell, T. B.; Christensen, R. L. Electronic Relaxation in Long Polyenes. *J. Phys. Chem.* **1990**, *94*, 8118–8124.

(36) Katoh, T.; Nagashima, U.; Mimuro, M. Fluorescence Properties of the Allenic Carotenoid Fucoxanthin: Implication for Energy Transfer in Photosynthetic Pigment Systems. *Photosynth. Res.* **1991**, *27* (3), 221–226.

(37) DeCoster, B.; Christensen, R. L.; Gebhard, R.; Lugtenburg, J.; Farhoosh, R.; Frank, H. A. Low-Lying Electronic States of Carotenoids. *Biochim. Biophys. Acta* **1992**, *1102* (1), 107–114.

(38) Mimuro, M.; Nagashima, U.; Takaichi, S.; Nishimura, Y.; Yamazaka, I.; Katoh, T. Molecular Structure and Optical Properties of Cartenoids for the *in Vivo* Energy Transfer Function in Algal Photosynthetic Pigment System. *Biochim. Biophys. Acta* **1992**, *1098*, 271–274.

(39) Mimuro, M.; Nishimura, Y.; Yamazaki, I.; Katoh, T.; Nagashima, U. Fluorescence Properties of the Allenic Carotenoid Fucoxanthin: Analysis of the Effect of Keto Carbonyl Group by Using a Model Compound, All-Trans-B-Apo-8'-Carotenal. *J. Lumin.* **1991**, *50*, 1–10.

(40) Andersson, P. O.; Gillbro, T.; Asato, A. E.; Liu, R. S. H. Dual Singlet State Emission in a Series of Mini-Carotenes. *J. Lumin.* **1992**, *51* (1-3), 11–20.

(41) Cogdell, R. J.; Andersson, P. O.; Gillbro, T. Carotenoid Singlet States and Their Involvement in Photosynthetic Light-Harvesting Pigments. *J. Photochem. Photobiol. B* **1992**, *15* (1-2), 105–112.

(42) Watanabe, Y.; Kameyama, T.; Miki, Y.; Kuki, M.; Koyama, Y. The 2 ^{1}A\textsubscript{g}- State and Two Additional Low-Lying Electronic States of Spheroidene Newly Identified by Fluorescence and Fluorescence-Excitation Spectroscopy at 170 K. *Chem. Phys. Lett.* **1993**, *206* (1-4), 62–68.

(43) Gillbro, T.; Andersson, P. O.; Liu, R. S. H.; Asato, A. E.; Takaishi, S.; Cogdell, R. J. Location of the Carotenoid $2A_g^-$ State and Its Role in Photosynthesis. *Photochem. Photobiol.* **1993**, *57* (1), 44–48.

(44) Bondarev, S. L.; Knyukshto, V. N. Fluorescence from the S_1 (2^1A_g) State of All-*trans*-β-Carotene. *Chem. Phys. Lett.* **1994**, *225*, 346–350.

(45) Koyama, Y. Structures, Excited-State Properties and Functions of Carotenoids in Photosynthesis. *Spectrosc. Biol. Mol., Eur. Conf., 6th* **1995**, 183–186.

(46) Fujii, R.; Onaka, K.; Kuki, M.; Koyama, Y.; Watanabe, Y. The $2A_g^-$ Energies of All-*trans*-Neurosporene and Spheroidene as Determined by Fluorescence Spectroscopy. *Chem. Phys. Lett.* **1998**, *288* (5,6), 847–853.

(47) Onaka, K.; Fujii, R.; Nagae, H.; Kuki, M.; Koyama, Y.; Watanabe, Y. The State Energy and the Displacements of the Potential Minima of the $2A_g^-$ State in All-*trans*-β-Carotene as Determined by Fluorescence Spectroscopy. *Chem. Phys. Lett.* **1999**, *315* (1,2), 75–81.

(48) Bautista, J. A.; Connors, R. E.; Raju, B. B.; Hiller, R. G.; Sharples, F. P.; Gosztola, D.; Wasielewski, M. R.; Frank, H. A. Excited State Properties of Peridinin: Observation of a Solvent Dependence of the Lowest Excited Singlet State Lifetime and Spectral Behavior Unique among Carotenoids. *J. Phys. Chem. B* **1999**, *103* (41), 8751–8758.

(49) Vaswani, H. M.; Hsu, C. P.; Head-Gordon, M.; Fleming, G. R. Quantum Chemical Evidence for an Intramolecular Charge-Transfer State in the Carotenoid Peridinin of Peridinin-Chlorophyll-Protein. *J. Phys. Chem. B* **2003**, *107* (31), 7940–7946.

(50) Zigmantas, D.; Polívka, T.; Hiller, R. G.; Yartsev, A.; Sundström, V. Spectroscopic and Dynamic Properties of the Peridinin Lowest Singlet Excited States. *J. Phys. Chem. A* **2001**, *105* (45), 10296–10306.

(51) Zigmantas, D.; Hiller, R. G.; Sundstrom, V.; Polivka, T. Carotenoid to Chlorophyll Energy Transfer in the Peridinin-Chlorophyll-*a*-Protein Complex Involves an Intramolecular Charge Transfer State. *Proc. Natl. Acad. Sci. U. S. A.* **2002**, *99* (26), 16760–16765.

(52) Zigmantas, D.; Hiller, R. G.; Yartsev, A.; Sundström, V.; Polívka, T. Dynamics of Excited States of the Carotenoid Peridinin in Polar Solvents: Dependence on Excitation Wavelength, Viscosity, and Temperature. *J. Phys. Chem. B* **2003**, *107*, 5339–5348.

(53) Zigmantas, D.; Hiller, R. G.; Sharples, F. P.; Frank, H. A.; Sundström, V.; Polívka, T. Effect of a Conjugated Carbonyl Group on the Photophysical Properties of Carotenoids. *Phys. Chem. Chem. Phys.* **2004**, *6* (11), 3009–3016.

(54) Herek, J. L.; Wendling, M.; He, Z.; Polívka, T.; Garcia-Asua, G.; Cogdell, R. J.; Hunter, C. N.; van Grondelle, R.; Sundström, V.; Pullerits, T. Ultrafast Carotenoid Band Shifts: Experiment and Theory. *J. Phys. Chem. B* **2004**, *108* (29), 10398–10403.

(55) Papagiannakis, E.; Larsen, D. S.; van Stokkum, I. H. M.; Vengris, M.; Hiller, R. G.; van Grondelle, R. Resolving the Excited State Equilibrium of Peridinin in Solution. *Biochemistry* **2004**, *43* (49), 15303–15309.

(56) Wild, D. A.; Winkler, K.; Stalke, S.; Oum, K.; Lenzer, T. Extremely Strong Solvent Dependence of the S_1 -> S0 Internal Conversion Lifetime of 12'-Apo-β-Caroten-12'-Al. *Phys. Chem. Chem. Phys.* **2006**, *8* (21), 2499–2505.

(57) Stalke, S.; Wild, D. A.; Lenzer, T.; Kopczynski, M.; Lohse, P. W.; Oum, K. Solvent-Dependent Ultrafast Internal Conversion Dynamics of N'-Apo-Beta-Carotenoic-N'-Acids (n = 8, 10, 12). *Phys. Chem. Chem. Phys.* **2008**, *10* (16), 2180–2188.

(58) Kopczynski, M.; Ehlers, F.; Lenzer, T.; Oum, K. Evidence for an Intramolecular Charge Transfer State in 12'-Apo-β-Caroten-12'-Al and 8'-Apo-β-Caroten-8'-Al: Influence of Solvent Polarity and Temperature. *J. Phys. Chem. A* **2007**, *111* (25), 5370–5381.

(59) Bautista, J. A.; Hiller, R. G.; Sharples, F. P.; Gosztola, D.; Wasielewski, M.; Frank, H. A. Singlet and Triplet Energy Transfer in the Peridinin−Chlorophyll *a*−Protein from *Amphidinium Carterae*. *J. Phys. Chem. A* **1999**, *103* (14), 2267–2273.

(60) Shima, S.; Ilagan, R. P.; Gillespie, N.; Sommer, B. J.; Hiller, R. G.; Sharples, F. P.; Frank, H. A.; Birge, R. R. Two-Photon and Fluorescence Spectroscopy and the Effect of Environment on the Photochemical Properties of Peridinin in Solution and in the Peridinin-Chlorophyll-Protein from *Amphidinium Carterae*. *J. Phys. Chem. A* **2003**, *107* (40), 8052–8066.

(61) Wagner, N. L.; Greco, J. A.; Enriquez, M. M.; Frank, H. A.; Birge, R. R. The Nature of the Intramolecular Charge Transfer State in Peridinin. *Biophys. J.* **2013**, *104*, 1314–1325.

(62) Linden, P. A.; Zimmermann, J.; Brixner, T.; Holt, N. E.; Vaswani, H. M.; Hiller, R. G.; Fleming, G. R. Transient Absorption Study of Peridinin and Peridinin–chlorophyll *a*–protein after Two-Photon Excitation. *J. Phys. Chem. B* **2004**, *108*, 10340–10345.

(63) Lampoura, S. S.; Krueger, B. P.; van Stokkum, I. H. M.; Salverda, J. M.; Gradinaru, C. C.; Rutkauskas, D.; Hiller, R. G.; van Grondelle, R. Energy Transfer in the Peridinin Chlorophyll *a* Protein of *Amphidinium Carterae* Studied by Polarized Absorption Measurements. *Int. J. Mod. Phys. B* **2001**, *15*, 3849–3852.

(64) van Stokkum, I. H. M.; Papagiannakis, E.; Vengris, M.; Salverda, J. M.; Polívka, T.; Zigmantas, D.; Larsen, D. S.; Lampoura, S. S.; Hiller, R. G.; van Grondelle, R. Inter-Pigment Interactions in the Peridinin Chlorophyll Protein Studied by Global and Target Analysis of Time Resolved Absorption Spectra. *Chem. Phys.* **2009**, *357*, 70–78.

(65) Ghosh, S.; Bishop, M. M.; Roscioli, J. D.; LaFountain, A. M.; Frank, H. A.; Beck, W. F. Excitation Energy Transfer by Coherent and Incoherent Mechanisms in the Peridinin–chlorophyll *a* Protein. *J. Phys. Chem. Lett.* **2017**, *8*, 463–469.

(66) Roscioli, J. D.; Ghosh, S.; LaFountain, A. M.; Frank, H. A.; Beck, W. F. Quantum Coherent Excitation Energy Transfer by Carotenoids in Photosynthetic Light Harvesting. *J. Phys. Chem. Lett.* **2017**, *8* (20), 5141–5147.

(67) Roscioli, J. D.; Ghosh, S.; LaFountain, A. M.; Frank, H. A.; Beck, W. F. Structural Tuning of Quantum Decoherence and Coherent Energy Transfer in Photosynthetic Light Harvesting. *J. Phys. Chem. Lett.* **2018**, *9*, 5071–5077.

(68) Brus, L. E. A Simple Model for the Ionization Potential, Electron Affinity, and Aqueous Redox Potentials of Small Semiconductor Crystallites. *J. Chem. Phys.* **1983**, *79* (11), 5566–5571.

(69) Brus, L. Quantum Crystallites and Nonlinear Optics. *Appl. Phys. A: Mater. Sci. Process.* **1991**, *53* (6), 465–474.

(70) Alivisatos, A. P. Semiconductor Clusters, Nanocrystals, and Quantum Dots. *Science* **1996**, *271* (5251), 933–937.

(71) Efros, A. L.; Rosen, M. The Electronic Structure of Semiconductor Nanocrystals. *Annu. Rev. Mater. Sci.* **2000**, *30* (1), 475–521.

(72) Alivisatos, A. P.; Harris, A. L.; Levinos, N. J.; Steigerwald, M. L.; Brus, L. E. Electronic States of Semiconductor Clusters: Homogeneous and Inhomogeneous Broadening of the Optical Spectrum. *J. Chem. Phys.* **1988**, *89* (7), 4001–4011.

(73) Ekimov, A. I.; Hache, F.; Schanne-Klein, M. C.; Ricard, D.; Flytzanis, C.; Kudryavtsev, I. A.; Yazeva, T. V.; Rodina, A. V.; Efros, A. L. Absorption and Intensity-Dependent Photoluminescence Measurements on CdSe Quantum Dots: Assignment of the First Electronic Transitions. *J. Opt. Soc. Am. B, JOSAB* **1993**, *10* (1), 100–107.

(74) Norris, D. J.; Bawendi, M. G. Measurement and Assignment of the Size-Dependent Optical Spectrum in CdSe Quantum Dots. *Phys. Rev. B Condens. Matter* **1996**, *53* (24), 16338–16346.

(75) Norris, D. J.; Sacra, A.; Murray, C. B.; Bawendi, M. G. Measurement of the Size Dependent Hole Spectrum in CdSe Quantum Dots. *Phys. Rev. Lett.* **1994**, *72* (16), 2612–2615.

(76) Lifshitz, E. Evidence in Support of Exciton to Ligand Vibrational Coupling in Colloidal Quantum Dots. *J. Phys. Chem. Lett.* **2015**, *6* (21), 4336–4347.

(77) Owen, J.; Brus, L. Chemical Synthesis and Luminescence Applications of Colloidal Semiconductor Quantum Dots. *J. Am. Chem. Soc.* **2017**, *139* (32), 10939–10943.

(78) Klimov, V. I.; Mikhailovsky, A. A.; Xu, S.; Malko, A.; Hollingsworth, J. A.; Leatherdale, C. A.; Eisler, H.; Bawendi, M. G. Optical Gain and Stimulated Emission in Nanocrystal Quantum Dots. *Science* **2000**, *290* (5490), 314–317.

(79) Klimov, V. I. Spectral and Dynamical Properties of Multiexcitons in Semiconductor Nanocrystals. *Annu. Rev. Phys. Chem.* **2007**, *58*, 635–673.

(80) García-Santamaría, F.; Chen, Y.; Vela, J.; Schaller, R. D.; Hollingsworth, J. A.; Klimov, V. I. Suppressed Auger Recombination in "Giant" Nanocrystals Boosts Optical Gain Performance. *Nano Lett.* **2009**, *9* (10), 3482–3488.

(81) Weiss, E. A. Designing the Surfaces of Semiconductor Quantum Dots for Colloidal Photocatalysis. *ACS Energy Lett.* **2017**, *2* (5), 1005–1013.

(82) Bloom, B. P.; Liu, R.; Zhang, P.; Ghosh, S.; Naaman, R.; Beratan, D. N.; Waldeck, D. H. Directing Charge Transfer in Quantum Dot Assemblies. *Acc. Chem. Res.* **2018**, *51* (10), 2565–2573.

(83) Efros, A. L.; Kharchenko, V. A.; Rosen, M. Breaking the Phonon Bottleneck in Nanometer Quantum Dots: Role of Auger-like Processes. *Solid State Commun.* **1995**, *93* (4), 281–284.

(84) Klimov, V. I.; McBranch, D. W. Femtosecond P-to- S Electron Relaxation in Strongly Confined Semiconductor Nanocrystals. *Phys. Rev. Lett.* **1998**, *80* (18), 4028–4031.

(85) Klimov, V. I., VI; Mikhailovsky, A. A.; McBranch, D. W.; Leatherdale, C. A.; Bawendi, M. G. Quantization of Multiparticle Auger Rates in Semiconductor Quantum Dots. *Science* **2000**, *287* (5455), 1011–1013.

(86) Klimov, V. I.; Mikhailovsky, A. A.; McBranch, D. W.; Leatherdale, C. A.; Bawendi, M. G. Mechanisms for Intraband Energy Relaxation in Semiconductor Quantum Dots: The Role of Electron-Hole Interactions. *Phys. Rev. B Condens. Matter* **2000**, *61* (20), R13349–R13352.

(87) Klimov, V. I. Optical Nonlinearities and Ultrafast Carrier Dynamics in Semiconductor Nanocrystals. *J. Phys. Chem. B* **2000**, *104* (26), 6112–6123.

(88) Guyot-Sionnest, P.; Shim, M.; Matranga, C.; Hines, M. Intraband Relaxation in CdSe Quantum Dots. *Phys. Rev. B Condens. Matter* **1999**, *60* (4), R2181–R2184.

(89) Guyot-Sionnest, P.; Wehrenberg, B.; Yu, D. Intraband Relaxation in CdSe Nanocrystals and the Strong Influence of the Surface Ligands. *J. Chem. Phys.* **2005**, *123* (7), 074709.

(90) Peterson, M. D.; Cass, L. C.; Harris, R. D.; Edme, K.; Sung, K.; Weiss, E. A. The Role of Ligands in Determining the Exciton Relaxation Dynamics in Semiconductor Quantum Dots. *Annu. Rev. Phys. Chem.* **2014**, *65*, 317–339.

(91) Liu, J.; Kilina, S. V.; Tretiak, S.; Prezhdo, O. V. Ligands Slow Down Pure-Dephasing in Semiconductor Quantum Dots. *ACS Nano* **2015**, *9* (9), 9106–9116.

(92) Nozik, A. J. Spectroscopy and Hot Electron Relaxation Dynamics in Semiconductor Quantum Wells and Quantum Dots. *Annu. Rev. Phys. Chem.* **2001**, *52*, 193–231.

(93) Inoshita, T.; Sakaki, H. Electron Relaxation in a Quantum Dot: Significance of Multiphonon Processes. *Phys. Rev. B Condens. Matter* **1992**, *46* (11), 7260–7263.

(94) Inoshita, T.; Sakaki, H. Electron-Phonon Interaction and the so-Called Phonon Bottleneck Effect in Semiconductor Quantum Dots. *Physica B Condens. Matter* **1996**, *227* (1), 373–377.

(95) Li, X.-Q.; Nakayama, H.; Arakawa, Y. Phonon Bottleneck in Quantum Dots: Role of Lifetime of the Confined Optical Phonons. *Phys. Rev. B Condens. Matter* **1999**, *59* (7), 5069–5073.

(96) Klimov, V. I.; McBranch, D. W.; Leatherdale, C. A.; Bawendi, M. G. Electron and Hole Relaxation Pathways in Semiconductor Quantum Dots. *Phys. Rev. B Condens. Matter* **1999**, *60* (19), 13740–13749.

(97) Cooney, R. R.; Sewall, S. L.; Anderson, K. E. H.; Dias, E. A.; Kambhampati, P. Breaking the Phonon Bottleneck for Holes in Semiconductor Quantum Dots. *Phys. Rev. Lett.* **2007**, *98* (17), 177403.

(98) Cooney, R. R.; Sewall, S. L.; Dias, E. A.; Sagar, D. M.; Anderson, K. E. H.; Kambhampati, P. Unified Picture of Electron and Hole Relaxation Pathways in Semiconductor Quantum Dots. *Phys. Rev. B Condens. Matter* **2007**, *75* (24), 245311.

(99) Kambhampati, P. Hot Exciton Relaxation Dynamics in Semiconductor Quantum Dots: Radiationless Transitions on the Nanoscale. *J. Phys. Chem. C* **2011**, *115* (45), 22089–22109.

(100) Pandey, A.; Guyot-Sionnest, P. Slow Electron Cooling in Colloidal Quantum Dots. *Science* **2008**, *322* (5903), 929–932.

(101) T isdale, W. A.; Williams, K. J.; Timp, B. A.; Norris, D. J.; Aydil, E. S.; Zhu, X.-Y. Hot-Electron Transfer from Semiconductor Nanocrystals. *Science* **2010**, *328* (5985), 1543–1547.

(102) Bawendi, M. G.; Carroll, P. J.; Wilson, W. L.; Brus, L. E. Luminescence Properties of CdSe Quantum Crystallites: Resonance between Interior and Surface Localized States. *J. Chem. Phys.* **1992**, *96* (2), 946–954.

(103) Kuno, M.; Lee, J. K.; Dabbousi, B. O.; Mikulec, F. V.; Bawendi, M. G. The Band Edge Luminescence of Surface Modified CdSe Nanocrystallites: Probing the Luminescing State. *J. Chem. Phys.* **1997**, *106* (23), 9869–9882.

(104) Gao, M.; Kirstein, S.; Möhwald, H.; Rogach, A. L.; Kornowski, A.; Eychmüller, A.; Weller, H. Strongly Photoluminescent CdTe Nanocrystals by Proper Surface Modification. *J. Phys. Chem. B* **1998**, *102* (43), 8360–8363.

(105) Yin, Y.; Alivisatos, A. P. Colloidal Nanocrystal Synthesis and the Organic-Inorganic Interface. *Nature* **2005**, *437* (7059), 664–670.

(106) Pandey, A.; Guyot-Sionnest, P. Hot Electron Extraction From Colloidal Quantum Dots. *J. Phys. Chem. Lett.* **2010**, *1* (1), 45–47.

(107) Bealing, C. R.; Baumgardner, W. J.; Choi, J. J.; Hanrath, T.; Hennig, R. G. Predicting Nanocrystal Shape through Consideration of Surface-Ligand Interactions. *ACS Nano* **2012**, *6* (3), 2118–2127.

(108) Yu, D.; Wang, C.; Guyot-Sionnest, P. N-Type Conducting CdSe Nanocrystal Solids. *Science* **2003**, *300* (5623), 1277–1280.

(109) Talapin, D. V.; Murray, C. B. PbSe Nanocrystal Solids for N- and P-Channel Thin Film Field-Effect Transistors. *Science* **2005**, *310* (5745), 86–89.

(110) Darugar, Q.; Landes, C.; Link, S.; Schill, A.; El-Sayed, M. A. Why Is the Thermalization of Excited Electrons in Semiconductor Nanoparticles so Rapid? Studies on CdSe Nanoparticles. *Chem. Phys. Lett.* **2003**, *373* (3), 284–291.

(111) Borys, N. J.; Walter, M. J.; Huang, J.; Talapin, D. V.; Lupton, J. M. The Role of Particle Morphology in Interfacial Energy Transfer in CdSe/CdS Heterostructure Nanocrystals. *Science* **2010**, *330* (6009), 1371–1374.

(112) Morris-Cohen, A. J.; Frederick, M. T.; Cass, L. C.; Weiss, E. A. Simultaneous Determination of the Adsorption Constant and the Photoinduced Electron Transfer Rate for a Cds Quantum Dot–Viologen Complex. *J. Am. Chem. Soc.* **2011**, *133* (26), 10146–10154.

(113) Mooney, J.; Krause, M. M.; Saari, J. I.; Kambhampati, P. Challenge to the Deep-Trap Model of the Surface in Semiconductor Nanocrystals. *Phys. Rev. B Condens. Matter* **2013**, *87* (8), 081201.

(114) Veamatahau, A.; Jiang, B.; Seifert, T.; Makuta, S.; Latham, K.; Kanehara, M.; Teranishi, T.; Tachibana, Y. Origin of Surface Trap States in CdS Quantum Dots: Relationship between Size Dependent Photoluminescence and Sulfur Vacancy Trap States. *Phys. Chem. Chem. Phys.* **2015**, *17* (4), 2850–2858.

(115) Giansante, C.; Infante, I. Surface Traps in Colloidal Quantum Dots: A Combined Experimental and Theoretical Perspective. *J. Phys. Chem. Lett.* **2017**, *8* (20), 5209–5215.

(116) Law, M.; Luther, J. M.; Song, Q.; Hughes, B. K.; Perkins, C. L.; Nozik, A. J. Structural, Optical, and Electrical Properties of PbSe Nanocrystal Solids Treated Thermally or with Simple Amines. *J. Am. Chem. Soc.* **2008**, *130* (18), 5974–5985.

(117) Hyun, B.-R.; Bartnik, A. C.; Sun, L.; Hanrath, T.; Wise, F. W. Control of Electron Transfer from Lead-Salt Nanocrystals to TiO_2. *Nano Lett.* **2011**, *11* (5), 2126–2132.

(118) Schroeter, D. F.; Griffiths, D. J.; Sercel, P. C. Defect-Assisted Relaxation in Quantum Dots at Low Temperature. *Phys. Rev. B Condens. Matter* **1996**, *54* (3), 1486–1489.

(119) Owen, J. S.; Park, J.; Trudeau, P.-E.; Alivisatos, A. P. Reaction Chemistry and Ligand Exchange at Cadmium−Selenide Nanocrystal Surfaces. *J. Am. Chem. Soc.* **2008**, *130* (37), 12279–12281.

(120) Dong, A.; Ye, X.; Chen, J.; Kang, Y.; Gordon, T.; Kikkawa, J. M.; Murray, C. B. A Generalized Ligand-Exchange Strategy Enabling Sequential Surface Functionalization of Colloidal Nanocrystals. *J. Am. Chem. Soc.* **2011**, *133* (4), 998–1006.

(121) Anderson, N. C.; Hendricks, M. P.; Choi, J. J.; Owen, J. S. Ligand Exchange and the Stoichiometry of Metal Chalcogenide Nanocrystals: Spectroscopic Observation of Facile Metal-Carboxylate Displacement and Binding. *J. Am. Chem. Soc.* **2013**, *135* (49), 18536–18548.

(122) Anderson, N. C.; Owen, J. S. Soluble, Chloride-Terminated CdSe Nanocrystals: Ligand Exchange Monitored by 1 H and 31 P NMR Spectroscopy. *Chem. Mater.* **2013**, *25* (1), 69–76.

(123) Knauf, R. R.; Lennox, J. C.; Dempsey, J. L. Quantifying Ligand Exchange Reactions at CdSe Nanocrystal Surfaces. *Chem. Mater.* **2016**, *28* (13), 4762–4770.

(124) Owen, J. Nanocrystal Structure. The Coordination Chemistry of Nanocrystal Surfaces. *Science* **2015**, *347* (6222), 615–616.

(125) Kalyuzhny, G.; Murray, R. W. Ligand Effects on Optical Properties of CdSe Nanocrystals. *J. Phys. Chem. B* **2005**, *109* (15), 7012–7021.

(126) Bullen, C.; Mulvaney, P. The Effects of Chemisorption on the Luminescence of CdSe Quantum Dots. *Langmuir* **2006**, *22* (7), 3007–3013.

(127) Munro, A. M.; Jen-La Plante, I.; Ng, M. S.; Ginger, D. S. Quantitative Study of the Effects of Surface Ligand Concentration on CdSe Nanocrystal Photoluminescence. *J. Phys. Chem. C* **2007**, *111* (17), 6220–6227.

(128) Green, M. L. H. A New Approach to the Formal Classification of Covalent Compounds of the Elements. *J. Organomet. Chem.* **1995**, *500* (1-2), 127–148.

(129) Green, M. L. H.; Parkin, G. Application of the Covalent Bond Classification Method for the Teaching of Inorganic Chemistry. *J. Chem. Educ.* **2014**. https://doi.org/10.1021/ed400504f.

(130) Moreels, I.; Lambert, K.; De Muynck, D.; Vanhaecke, F.; Poelman, D.; Martins, J. C.; Allan, G.; Hens, Z. Composition and Size-Dependent Extinction Coefficient of Colloidal PbSe Quantum Dots. *Chem. Mater.* **2007**, *19* (25), 6101–6106.

(131) Chen, O.; Yang, Y.; Wang, T.; Wu, H.; Niu, C.; Yang, J.; Cao, Y. C. Surface-Functionalization-Dependent Optical Properties of II–VI Semiconductor Nanocrystals. *J. Am. Chem. Soc.* **2011**, *133* (43), 17504–17512.

(132) Cassette, E.; Dean, J. C.; Scholes, G. D. Two-Dimensional Visible Spectroscopy for Studying Colloidal Semiconductor Nanocrystals. *Small* **2016**, *12*, 2234–2244.

(133) Li, H.; Cundiff, S. T. 2D Coherent Spectroscopy of Electronic Transitions. In *Advances In Atomic, Molecular, and Optical Physics*; Elsevier, 2017; Vol. 66, pp 1–48.

(134) Jonas, D. M. Two-Dimensional Femtosecond Spectroscopy. *Annu. Rev. Phys. Chem.* **2003**, *54*, 425–463.

(135) Cho, M. Coherent Two-Dimensional Optical Spectroscopy. *Chem. Rev.* **2008**, *108* (4), 1331–1418.

(136) Ginsberg, N. S.; Cheng, Y.-C.; Fleming, G. R. Two-Dimensional Electronic Spectroscopy of Molecular Aggregates. *Acc. Chem. Res.* **2009**, *42*, 1352–1363.

(137) Ogilvie, J. P.; Kubarych, K. J. Multidimensional Electronic and Vibrational Spectroscopy. *Adv. At. Mol. Opt. Phys.* **2009**, *57*, 249–321.

(138) Chenu, A.; Scholes, G. D. Coherence in Energy Transfer and Photosynthesis. *Annu. Rev. Phys. Chem.* **2015**, *66*, 69–96.

(139) Kim, J.; Wong, C. Y.; Scholes, G. D. Exciton Fine Structure and Spin Relaxation in Semiconductor Colloidal Quantum Dots. *Acc. Chem. Res.* **2009**, *42* (8), 1037–1046.

(140) Wong, C. Y.; Scholes, G. D. Using Two-Dimensional Photon Echo Spectroscopy to Probe the Fine Structure of the Ground State Biexciton of CdSe Nanocrystals. *J. Lumin.* **2011**, *131* (3), 366–374.

(141) Wong, C. Y.; Scholes, G. D. Biexcitonic Fine Structure of CdSe Nanocrystals Probed by Polarization-Dependent Two-Dimensional Photon Echo Spectroscopy. *J. Phys. Chem. A* **2011**, *115* (16), 3797–3806.

(142) Harel, E.; Rupich, S. M.; Schaller, R. D.; Talapin, D. V.; Engel, G. S. Measurement of Electronic Splitting in PbS Quantum Dots by Two-Dimensional Nonlinear Spectroscopy. *Phys. Rev. B Condens. Matter* **2012**, *86* (7), 075412.

(143) Griffin, G. B.; Ithurria, S.; Dolzhnikov, D. S.; Linkin, A.; Talapin, D. V.; Engel, G. S. Two-Dimensional Electronic Spectroscopy of CdSe Nanoparticles at Very Low Pulse Power. *J. Chem. Phys.* **2013**, *138* (1), 014705.

(144) Caram, J. R.; Zheng, H.; Dahlberg, P. D.; Rolczynski, B. S.; Griffin, G. B.; Fidler, A. F.; Dolzhnikov, D. S.; Talapin, D. V.; Engel, G. S. Persistent Inter-Excitonic Quantum Coherence in CdSe Quantum Dots. *J. Phys. Chem. Lett.* **2014**, *5* (1), 196–204.

(145) Caram, J. R.; Zheng, H.; Dahlberg, P. D.; Rolczynski, B. S.; Griffin, G. B.; Dolzhnikov, D. S.; Talapin, D. V.; Engel, G. S. Exploring Size and State Dynamics in CdSe Quantum Dots Using Two-Dimensional Electronic Spectroscopy. *J. Chem. Phys.* **2014**, *140* (8), 084701.

(146) Tully, J. C. Nonadiabatic Molecular Dynamics. *Int. J. Quantum Chem.* **1991**, *40* (S25), 299–309.

(147) Yarkony, D. R. Current Issues in Nonadiabatic Chemistry. *J. Phys. Chem.* **1996**, *100* (48), 18612–18628.

(148) Tully, J. C. Perspective: Nonadiabatic Dynamics Theory. *J. Chem. Phys.* **2012**, *137*, 22A301.

(149) Curchod, B. F. E.; Martínez, T. J. Ab Initio Nonadiabatic Quantum Molecular Dynamics. *Chem. Rev.* **2018**, *118* (7), 3305–3336.

(150) Womick, J. M.; Moran, A. M. Exciton Coherence and Energy Transport in the Light-Harvesting Dimers of Allophycocyanin. *J. Phys. Chem. B* **2009**, *113* (48), 15747–15759.

(151) Womick, J. M.; Moran, A. M. Nature of Excited States and Relaxation Mechanisms in C-Phycocyanin. *J. Phys. Chem. B* **2009**, *113*, 15771–15782.

(152) Tiwari, V.; Peters, W. K.; Jonas, D. M. Electronic Resonance with Anticorrelated Pigment Vibrations Drives Photosynthetic Energy Transfer Outside the Adiabatic Framework. *Proc. Natl. Acad. Sci. U. S. A.* **2013**, *110* (4), 1203–1208.

(153) Tiwari, V.; Peters, W. K.; Jonas, D. M. Electronic Energy Transfer through Non-Adiabatic Vibrational-Electronic Resonance. I. Theory for a Dimer. *J. Chem. Phys.* **2017**, *147* (15), 154308.

(154) Jumper, C. C.; Rafiq, S.; Wang, S.; Scholes, G. D. From Coherent to Vibronic Light Harvesting in Photosynthesis. *Curr. Opin. Chem. Biol.* **2018**, *47*, 39–46.

(155) Cao, J.; Cogdell, R. J.; Coker, D. F.; Duan, H.-G.; Hauer, J.; Kleinekathöfer, U.; Jansen, T. L. C.; Mančal, T.; Miller, R. J. D.; Ogilvie, J. P.; Prokhorenko, V. I.; Renger, T.; Tan, H.-S.; Tempelaar, R.; Thorwart, M.; Thyrhaug, E.; Westenhoff, S.; Zigmantas, D. Quantum Biology Revisited. *Sci Adv* **2020**, *6* (14), eaaz4888.

Chapter 2: Experimental

In this chapter, we will discuss the experimental technique used in the study of excitation energy transfer in photosynthetic systems and semiconductor nanocrystals. The chapter contains the necessary theory to implement and interpret two-dimensional electronic spectroscopy (2DES), and introduce the newly designed instrument employed in this dissertation study

2.1 Two-Dimensional Electronic Spectroscopy

The experiments discussed in this dissertation employ broadband two-dimensional electronic spectroscopy (2DES), pioneered by Jonas and coworkers.[1] The 2DES technique is a powerful tool in the study of energy transfer dynamics in photosynthetic and semiconductor systems. The 2DES presents several significant advantages over traditional approaches such as transient absorption (TA). In particular, broadband excitation pulses allow for transform limit pulse durations as short as 6.5 fs. Additionally, the resulting spectra allows for correlation of events across a range of frequencies during a single experiment. Lastly, a powerful feature of 2DES is the ability to improve the resolution of congested spectral lineshapes, which is crucial in the study of systems that exhibit inhomogeneous line broadening from random energy fluctuations involving the surroundings. The approach of 2DES, however, presents several challenges. In particular, implementation of broadband, visible 2DES requires high phase-stability.

Over the years, there have been different implementations of the 2DES experiment. The first 2DES experiments were performed by Jonas and coworkers, using a conventional Michelson interferometer to generate four individual pulses from a cavity dumped Ti:sapphire laser, controlling the time of flight of arrival to the sample with conventional delay lines.[2] Later work by the Fleming group[3] and Miller group[4,5] implemented a diffractive-optics-based approach

to achieve passively phase stabilized optical geometry with wedge-shaped prisms to control time delays. Another approach involved active interferometric phase stabilization, as reported by the Cundiff group.[6] Each of the aforementioned approaches used four independent beams arranged in box-car geometry. An alternate approach employs a collinear (pump-probe) geometry, with the added implementation of phase-cycling,[7] phase-modulation,[8] or noncollinear pulse-shaping methods.[9–11] The experiments featured in this dissertation employ the latter approach.

2.1.1 Broadband Pulse Sequence

Regardless of approach, each implementation of 2DES involves three broadband excitation pulses, as shown in Figure 2.1. The pump pulse is split into two individual pulses with a time delay separation known as the coherence time, τ. The first optical field-matter interaction by a pump pulse generates a coherence. This coherent oscillation will evolve and decay over time. In the 2DES experiment, a second optical field-matter interaction occurs with the second pump pulse, generating a population within the system. The population created by the second pump pulse can evolve, unperturbed, over a fixed waiting time, T, before a third interaction occurs with the probe pulse. This action creates another coherence that evolves to emit a signal after a certain emission time, t. The emitted signal is heterodyned by a local oscillator (LO).

The coherence time, τ, is scanned for a short interval (< 75 fs) at fixed waiting time, T. The emitted signal is heterodyned and Fourier transformed upon incidence onto a spectral grating and dispersed onto a charge-coupled device (CCD), where the spectrum is collected for a particular τ and T. This axis is called the directly detected axis or emission axis. If τ is scanned while T is fixed, a series of spectra are collected along the tau axis. Fourier transformation of this axis provides the second axis in the 2DES experiments. This axis is called the indirectly detected axis or excitation axis.

The result is a 2D spectrum that can be interpreted as a correlation spectrum:[1] at a given (*x, y)* coordinate in the plotted contours, the plotted signal arises from the sequential action of a specific wavelength *x* from the excitation pulse pair followed by the action of a certain wavelength *y* of the probe pulse after the indicated waiting time *T*. By repeating the 2DES measurements as a function of *T* can observe the time evolution of the populations and coherences that were prepared by the initial pair of excitation pulses.

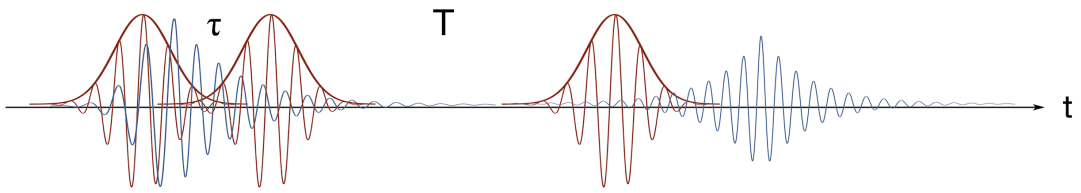

Figure 2.1. Pulse sequence in the 2DES experiment. Three broadband excitation pulses are represented by red Gaussians. The oscillating coherence is depicted in blue between the first two pulses. After the coherence time, τ, a population is generated. After a waiting time, *T*, the third pulse (probe) creates another coherence which emits a photon echo (blue evolving cosine).

2.1.2 Third-Order Nonlinear Responses

The signals discussed in this dissertation involves three types of responses: *ground state bleaching*, *stimulated emission*, and *excited-state absorption*. The theory involved in interpreting the nonlinear responses are based on the works of Mukamel,[12] and Hamm and Zanni.[13] A more detailed review is included in Jerome Roscioli's dissertation.[14]

In this section, a brief overview of the three types of responses are described using wave mixing energy level diagrams (WMEL) to interpret signals from a three level system. The WMEL diagrams are depicted by three states as horizontal lines: the ground state, labeled *g*; the first excited state, *e*; and the second excited state, *f*. Actions by an external electric field are shown in red.

Ground state bleaching (GSB) is a result of the formation of ground state population after the first two actions of light (interactions between a pump-pulse pair and the system), followed by the probe pulse that excites the ground state population. The first action by the pump pulse creates a *ge* or *eg* coherence, as shown in Figure 2.2. This coherence can evolve and decay over time. In the 2DES experiment, however, a second action of light occurs after a short coherent time, τ, by the second pump pulse. This results in a nonequilibrium, ground state population, *gg* in Figure 2.2. The ground state population is described as nonequilibrium as a result of the first two actions of light, and conservation of momentum of the photons within the system. After a particular waiting time, *T*, a third action of light will act on the ground state population and create another coherence, *eg*. This coherence will then decay and emit a signal after the emission time, *t*. This emitted signal is the third-order nonlinear response that will be represented in the 2DES spectrum.

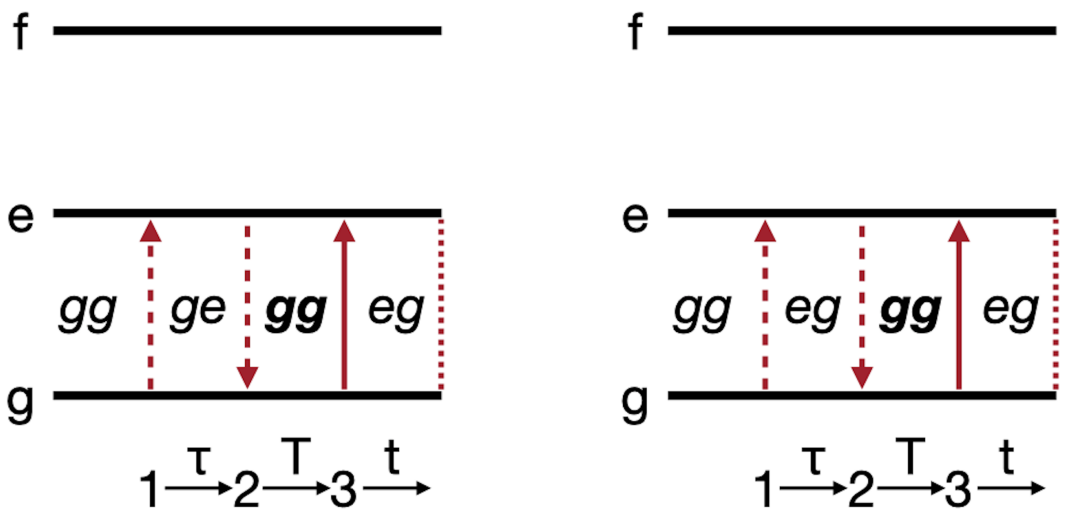

Figure 2.2. WMEL diagrams of rephasing (left) and nonrephasing (right) ground state bleaching response. In the WMEL diagram, actions of light are represented by red arrows, with time increasing from left to right. The final dashed line represents the emitted signal.

Stimulated emission (SE) is identical to GSB, as the sequence of events involves only the ground and first excited state. However, the actions of the first two pulses generate a population in the first excited state. As shown in Figure 2.3, the system starts in the ground state, *gg*. The first action of light creates a coherence *ge* or *eg*. After the coherent time, τ, the second pulse creates a population in the excited state, *ee*. The population will then evolve during the waiting time, *T*, when the probe acts on the excited state to create a coherence, *eg*. That coherence will decay to emit a signal after the emission time, *t*.

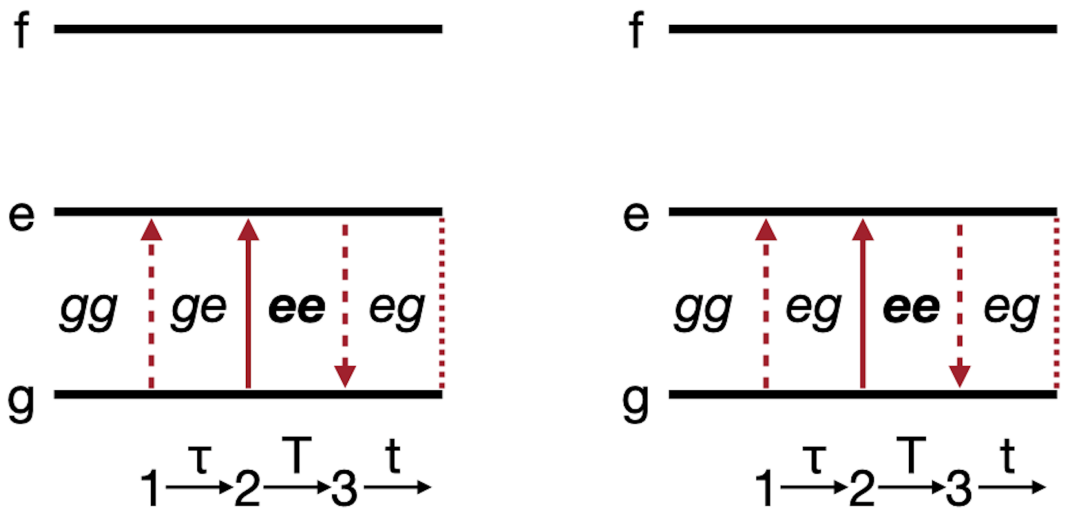

Figure 2.3. WMEL diagrams of rephasing (left) and nonrephasing (right) stimulated emission response. In the WMEL diagram, actions of light are represented by red arrows, with time increasing from left to right. The final dashed line represents the emitted signal.

Unlike GSB and SE, excited-state absorption (ESA) involves the second excited state, *f*. As shown in Figure 2.4, the first two actions of light, the result is similar to that of SE. However, the third action by the probe excites the first excited state to create a coherence between the first and second excited state, *ef*.

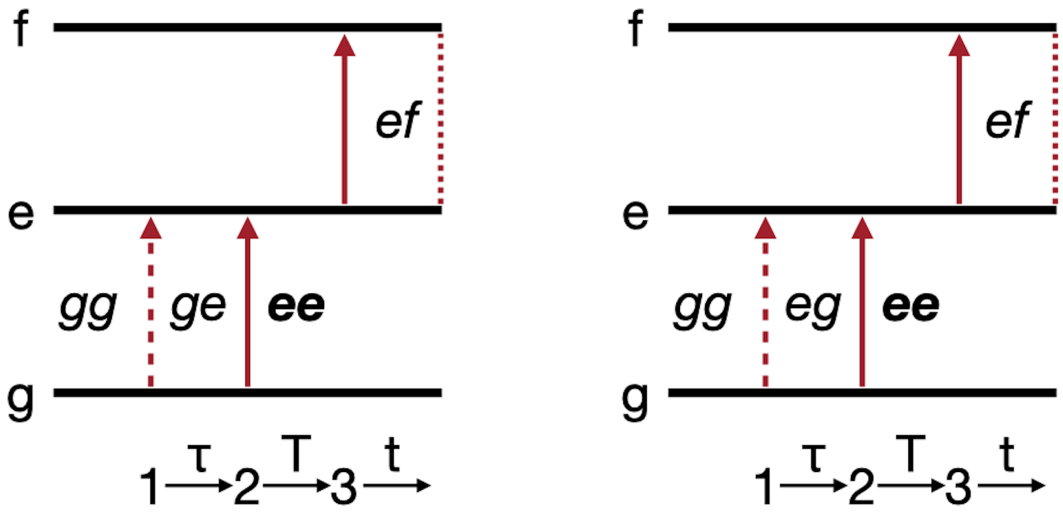

Figure 2.4. WMEL diagrams of rephasing (left) and nonrephasing (right) excited-state absorption response. In the WMEL diagram, actions of light are represented by red arrows, with time increasing from left to right. The final dashed line represents the emitted signal.

2.2 Experimental Design

Previous studies[14] in the Beck laboratory employed a passively phase-stabilized photon echo spectrometer based on the designs of Brixner et. al[3] and Moran and Scherer.[15] In this approach, the pump and probe beams were separated by a conventional time-of-flight delay line. Both beams were then focused onto a single spot of a transmissive diffractive optic (DO), dispersing different orders. Four beams were then collimated and arranged in a box-car geometry. Three beams were passed through wedge pairs to introduce the coherent time delay between the pump-pulse pair. The third, reference beam, LO, was delayed with respect to the probe beam. The four beams were ordered and focused at the sample position so that the signal is emitted along the same direction as the LO. A CCD was placed along this direction, and the time

and space ordering ensured the phase matching criteria was satisfied. The experiment involved Fourier transform spectral interferometry to obtain the desired signal.

In this previous design, the emitted signal needed to be phased to separate absorptive and dispersive components of a complex signal. This process required an additional phase factor correction, owing to the phase difference introduced between the LO and the emitted signal. The phase factor was obtained through the projection slice theorem[3] using pump-probe spectroscopy.[14]

The phase uncertainty, and time-consuming optical engineering required to perform 2DES experiments influenced the new approach employed for the studies in this dissertation.

2.2.1 Collinear Two-Dimensional Electronic Spectroscopy

The experimental 2DES setup employed to study excitation energy transfer in this dissertation was performed in pump-probe geometry. The experimental design is based on the design by Ogilvie and coworkers[10] and Zanni and coworkers,[11] using adaptive pulse shapers to generate a coherent pump-pulse pair. The detection scheme is inspired by the scheme details by Zigmantas and coworkers,[16] using amplitude modulation and phase sensitive detection.

The femtosecond excitation pulses were produced by a Yb oscillator and amplifier (Spectra Physics Spirit-4W) with a 100 kHz output at 1040nm with 4W power output. The laser pumps a noncollinear optical parametric amplifier (NOPA, Spectra Physics Spirit-NOPA-3H), where the fundamental beam is split into two beams to generate a white light continuum (WL) and a third harmonic (THG). The THG and WL were mixed at two amplification stages containing nonlinear crystals, generating the designed laser spectrum used in the experiments reported in this dissertation. The NOPA output is split into two beams by a broadband dielectric beamsplitter (Layertec, Mellingen), and each beam is directed into an adaptive pulse shaper

(FemtoJock and FemtoJock P, Biophotonics Solutions Inc.). These instruments provided two primary laser spectrum outputs used in the dissertation research: one spanning 495 nm-575 nm, with a central wavelength of 530 nm, and a 15 fs transform limited pulse duration; and 520 nm-710 nm, centered at 615 nm and a 6.5 fs transform limited pulse duration. Using multiphoton intrapulse interference phase scan (MIIPS),[17] and a pair of broadband chirped mirrors (Ultrafast Innovations, Munich), the pump and probe pulses are compressed close to transform limited durations at the sample position.

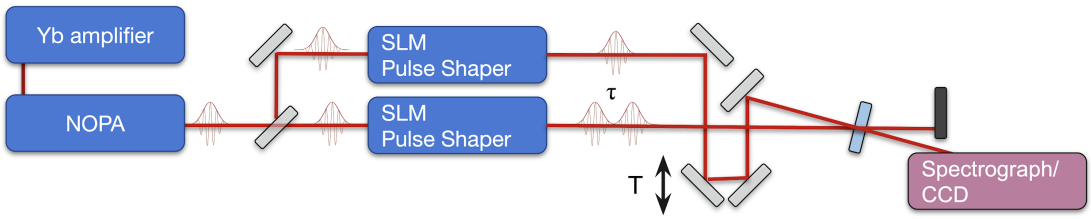

Figure 2.5. Laser and instrumentation used in the 2DES experiment. The Yb amplifier was used to pump the NOPA with 100 kHz, 1040 nm, 4W output. The NOPA was aligned to generate the desired output featured in Chapter 3, 4 and 5. SLM based adaptive pulse shapers were used to compress broadband pulses to the transform limit duration. The pump-beam pulse shaper generated the coherent pump-pulse pair. Signal was collected by a lab built spectrograph with a fast CCD detection scheme.

2.2.2 Noncollinear Pulse-Shaping

The pulse shaper on the pump beam (FemtoJock, Biophotonic Solutions Inc.) contains two 128-pixel spatial light modulators (SLM), allowing for control of both the phase and amplitude of the transmitted electric field. With that, the incoming pump pulse is split into a pump-pulse pair through manipulation of the phase and amplitude of the electric field with programming.

The incoming electric field can be described by the function: *E(t)*. As shown in Figure 2.6, the desired result of the pulse splitting technique produces two independent pulse described by Eq. 2.1 and 2.2 respectively:

$$\frac{1}{2}E(t-\frac{\tau}{2})\cdot e^{-i\frac{\phi}{2}} \tag{2.1}$$

$$\frac{1}{2}E(t+\frac{\tau}{2})\cdot e^{+i\frac{\phi}{2}} \tag{2.2}$$

where τ is the desired coherent time delay, and ϕ is the desired phase difference between the two pulses. The combined electric field is described as:

$$E'(t)=[\frac{1}{2}E(t-\frac{\tau}{2})\cdot e^{-i\frac{\phi}{2}}]+[\frac{1}{2}E(t+\frac{\tau}{2})\cdot e^{+i\frac{\phi}{2}}] \tag{2.3}$$

Fourier transformation from the time domain to the frequency domain:

$$E'(\omega)=\int_{-\infty}^{\infty}[\frac{1}{2}E(t-\frac{\tau}{2})\cdot e^{-i\frac{\phi}{2}}]+[\frac{1}{2}E(t+\frac{\tau}{2})\cdot e^{+i\frac{\phi}{2}}]\times e^{-i\omega t}\,dt \tag{2.4}$$

$$E'(\omega)=\frac{1}{2}E(\omega)\cdot[e^{-i(\frac{\omega\tau+\phi}{2})}+e^{i(\frac{\omega\tau+\phi}{2})}] \tag{2.5}$$

Eq. 2.5 can be simplified to the form:

$$E'(\omega)=E(\omega)\cdot[\cos(\frac{\omega\tau+\phi}{2})] \tag{2.6}$$

Eq. 2.6 contains the terms necessary to alter the transmitted electric field through the SLM, by applying a phase mask ($\Phi(\omega)$) and transmission mask ($T(\omega)$):

$$\Phi(\omega)=\arg[\cos(\frac{\omega\tau+\phi}{2})] \tag{2.7}$$

$$T(\omega)=[\cos(\frac{\omega\tau+\phi}{2})]^2 \tag{2.8}$$

As shown in Figure 2.6, Eq. 6, 7 and 8 are applicable for pulses split and centered about the initial electric field. This sequencing, however, will create undesired variation of the waiting time, *T*, during the 2DES experiment. Therefore, mathematical adjustments of these equations were used to obtain the following:

$$E'(\omega)=E(\omega)\cdot[1+e^{-i(\omega\tau+\phi)}] \tag{2.9}$$

$$\Phi(\omega)=\arg[1+e^{-i(\omega\tau+\phi)}] \tag{2.10}$$

$$T(\omega)=[1+e^{-i(\omega\tau+\phi)}]^2 \tag{2.11}$$

The experiments conducted in this dissertation do not feature alterations to the phase term, ϕ, of the electric field. However, one is able to introduce phase-cycling to the pump-pulse pair to obtain the rephasing and nonrephasing components of the nonlinear signal.[10,13,18] The signal obtained in the experiments discussed in this dissertation are the sum of both the rephasing and nonrephasing pathways.

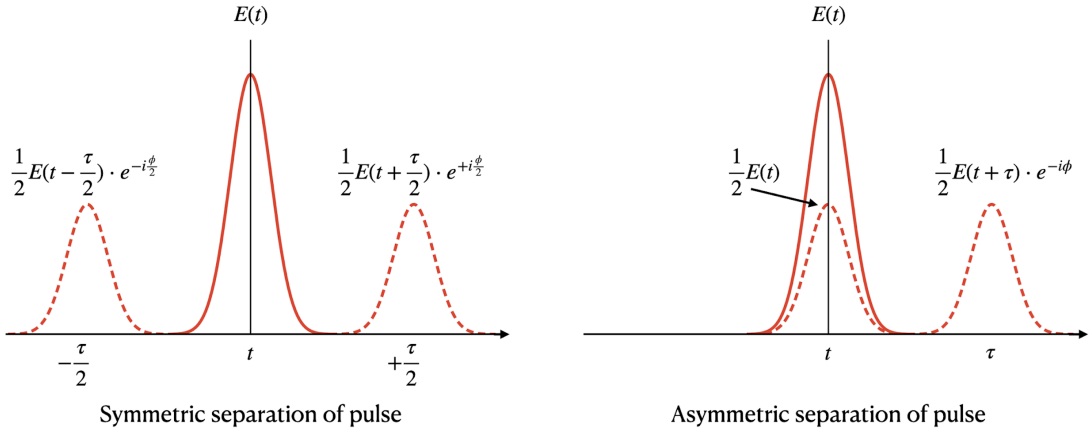

Figure 2.6. Pulse splitting sequence. (*left*) Symmetric separation of pulses centered around the initial electric field. (*right*) Asymmetric separation of pulses, where the first pulse is stepped forward by τ, and the second pulse is centered at the initial electric field.

The resulting pump-pulse pair can then be scanned over a coherent time axis ranging 0 fs to 75 fs in 2.5 fs steps (for shorter pulse durations, a 0 fs to 50 fs coherent time axis was implemented). The waiting time, *T*, between the second pump pulse and the third (probe) pulse is controlled by conventional delay lines, with a time of flight range of 300 ps.

The two beams are focused onto the sample by off-axis parabolic mirrors (OAP) to a spot size < 100 microns. The pulses are attenuated to energies of 2 nJ/pulse or 5 nJ/pulse, depending on the sample. The signal is emitted along the probe beam in this geometry. This is a significant advantage, as the probe serves as an intrinsic phase-stable local oscillator for heterodyne detection. The probe beam is directed into the spectrograph, while the pump beam is terminated after the sample interaction.

2.2.3 Detection Scheme

The previous instrument[14] employed shutters in individual beam paths to suppress scattering contributions to the signal, as described by Brixner et. al.[3] The detection scheme implemented in this newly designed spectrometer is based on a design by Augulis and Zigmantas.[16]

In the experimental setup, a mechanical chopper modulates the phase and amplitude of the pump beam at a frequency of 400 Hz. The signal emitted at the sample position is heterodyned by a local oscillator (LO) in the probe beam. The probe beam, containing the signal is focused through a spatial filter (50 to 100 micron pinhole), before being spatially dispersed by a 300 gr/mm diffraction grating within the spectrograph. This action performs a direct Fourier transformation of the signal onto a defined detection energy axis, which is collected on a fast CCD detector (Newton Andor 940) at a rate of 1 kHz. The dispersed light is focused on the lower 10 pixels of the CCD sensor (2048 W x 512 H). The CCD readout undergoes hardware binning and is shifted to the register as a single line. This single line of acquired data contains the probe intensity as well as the desired nonlinear response. This process is repeated to obtain blocks of spectra during a 800 millisecond integration (80,000 excitation pulse pairs at 100 kHz pulse-repetition frequency, at 400 Hz amplitude modulation of the pump beam by the mechanical chopper). The full-width acquisition of 2048 pixels in the spectra were binned by a factor of eight, producing 256 channels across the laser bandwidth. The pump-induced signal was then isolated using fast Fourier transformation of the modulated spectral time series (Figure 2.7) at each individual wavelength.

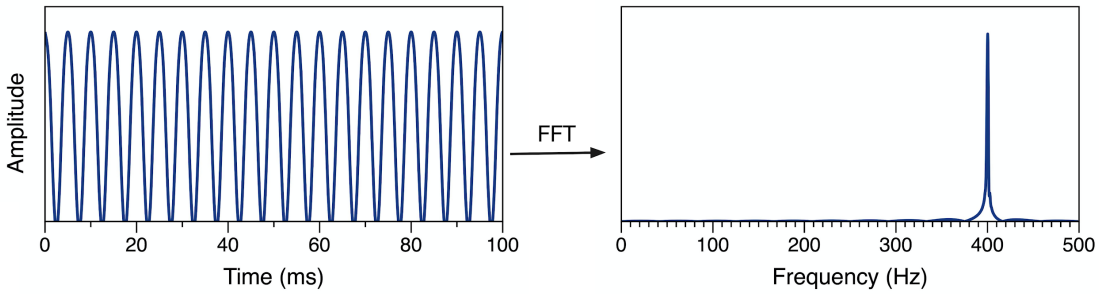

Figure 2.7. Simulated signal captured at 1 kHz over a period of 100 ms (*left*). Signal is imported and undergoes fast Fourier transformation to reveal desired emitted signal response at 400 Hz (*right*).

This particular method reduced possible scattering contributions that may be problematic in protein and nanocrystalline samples. The instrument was also designed to perform dual-beam amplitude modulation, where the desired signal can be isolated at the sum and difference-frequency of the modulations. Combined with the collinear geometry, the detection scheme removes any ambiguity of the phase of the emitted signal.

2.3 Data Processing of 2DES Spectra

The acquired dataset from each experiment contains a series of coherent time, τ, spectra at specific waiting times, T. Each waiting time can contain 151 coherent spectra (0 fs to 75 fs in 2.5 fs steps) or 101 spectra (0 fs to 50 fs in 2.5 fs steps). (The coherence time varied with transform limit pulse durations.) The waiting time spanned 0 to 300 ps, with varying step sizes from 2.5 fs to 100 ps. This condition varied for a given system to best follow the population kinetics. The entire process is repeated at least three times per experiment. Each spectrum collected is subject to background removal by subtracting the spectra collected at T = -3 ps. The dataset is loaded into a MATLAB software for data processing.

The coherent evolution obtained during the coherent time is a free induction decay. Following the final overlap between the pump-pulse pair, the remaining coherent time spectra simply contain irrelevant pump-probe signals. The points are removed in the initial moments of

the data processing, in order to reduce noise contributions to the 2DES spectra. Since the coherent evolution in the collinear spectra is symmetric about $\tau = 0$ fs, the spectra are mirrored and concatenated for each individual detection energy point (256 points spanning the laser spectrum). This step prevents artifacts from the fast Fourier transform (FFT) algorithm in MATLAB. The coherent evolution of spectra is then zero-padded to obtain 2^N points required for the interlaced decomposition of FFT (Figure 2.8). Each detection energy point undergoes FFT to generate a complex signal of real and imaginary components. The real component is combined to generate the correlated two-dimensional spectrum for a particular waiting time. This process is repeated for each waiting time T, and the again for each iteration captured during the experiment. The datasets for each iteration are statistically analyzed and averaged to increase the signal-to-noise ratio. Standard deviation and 95 % confidence intervals are also computed during this process.

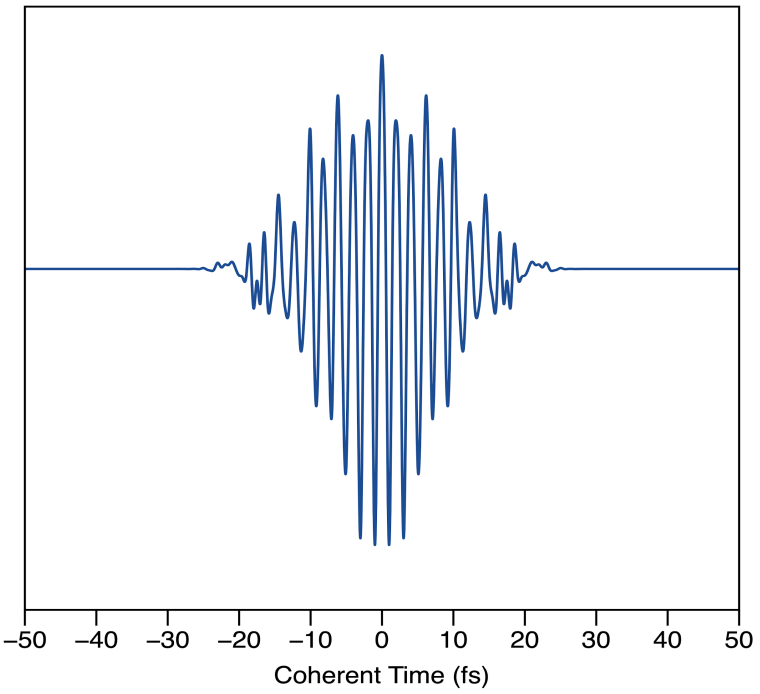

Figure 2.8. Coherent evolution of signal, integrated along the detection axis. The coherent signal is isolated, mirrored and zero-padded prior to the FFT process.

The 2DES data set is saved in a single MATLAB file, along with the statistical data points, excitation axis, detection axis, and waiting time axis. The 2DES contour map, as well as the coordinate specific amplitude change over time can then be plotted and analyzed separately, as will be discussed in the chapters to follow.

REFERENCES

REFERENCES

(1) Jonas, D. M. Two-Dimensional Femtosecond Spectroscopy. *Annu. Rev. Phys. Chem.* 2003, *54*, 425–463.

(2) Gallagher, S. M.; Albrecht, A. W.; Hybl, J. D.; Landin, B. L.; Rajaram, B.; Jonas, D. M. Heterodyne Detection of the Complete Electric Field of Femtosecond Four-Wave Mixing Signals. *J. Opt. Soc. Am. B* 1998, *15*, 2338–2345.

(3) Brixner, T.; Mančal, T.; Stiopkin, I. V.; Fleming, G. R. Phase-Stabilized Two-Dimensional Electronic Spectroscopy. *J. Chem. Phys.* 2004, *121*, 4221.

(4) Goodno, G. D.; Dadusc, G.; Miller, R. J. D. Ultrafast Heterodyne-Detected Transient-Grating Spectroscopy Using Diffractive Optics. *J. Opt. Soc. Am. B* 1998, *15*, 1791–1794.

(5) Goodno, G. D.; Miller, R. J. D. Femtosecond Heterodyne-Detected Four-Wave-Mixing Studies of Deterministic Protein Motions. 1. Theory and Experimental Technique of Diffractive Optics-Based Spectroscopy. *J. Phys. Chem. A* 1999, *103*, 10619–10629.

(6) Zhang, T.; Borca, C. N.; Li, X.; Cundiff, S. T. Optical Two-Dimensional Fourier Transform Spectroscopy with Active Interferometric Stabilization. *Optics Express*. 2005, p 7432. https://doi.org/10.1364/opex.13.007432.

(7) Tian, P.; Keusters, D.; Suzaki, Y.; Warren, W. S. Femtosecond Phase-Coherent Two-Dimensional Spectroscopy. *Science* 2003, *300*, 1553–1555.

(8) Tekavec, P. F.; Lott, G. A.; Marcus, A. H. Fluorescence-Detected Two-Dimensional Electronic Coherence Spectroscopy by Acousto-Optic Phase Modulation. *J. Chem. Phys.* 2007, *127* (21), 214307.

(9) Vaughan, J. C.; Hornung, T.; Stone, K. W.; Nelson, K. A. Coherently Controlled Ultrafast Four-Wave Mixing Spectroscopy. *J. Phys. Chem. A* 2007, *111* (23), 4873–4883.

(10) Myers, J. A.; Lewis, K. L.; Tekavec, P. F.; Ogilvie, J. P. Two-Color Two-Dimensional Fourier Transform Electronic Spectroscopy with a Pulse-Shaper. *Opt. Express* 2008, *16* (22), 17420.

(11) Shim, S. H.; Zanni, M. T. How to Turn Your Pump-Probe Instrument into a Multidimensional Spectrometer: 2D IR and Vis Spectroscopies via Pulse Shaping. *Phys. Chem. Chem. Phys.* 2009, *11* (5), 748–761.

(12) Mukamel, S. *Principles of Nonlinear Optical Spectroscopy*; Oxford University Press: New York, 1995.

(13) Hamm, P.; Zanni, M. *Concepts and Methods of 2D Infrared Spectroscopy*; Cambridge University Press: Cambridge, 2011.

(14) Roscioli, J. D. Detection of Coherent Energy Transfer Pathways in Photosynthesis with Two-Dimensional Electronic Spectroscopy. Chemistry - Doctor of Philosophy, Michigan State University, 2018.

(15) Moran, A. M.; Nome, R. A.; Scherer, N. F. Resolving the Emission Times of Solute and Solvent Four-Wave Mixing Signals by Spectral Interferometry. *J. Chem. Phys.* 2006, *125* (3), 31101.

(16) Augulis, R.; Zigmantas, D. Two-Dimensional Electronic Spectroscopy with Double Modulation Lock-in Detection: Enhancement of Sensitivity and Noise Resistance. *Opt. Express* 2011, *19* (14), 13126–13133.

(17) Lozovoy, V. V.; Pastirk, I.; Dantus, M. Multiphoton Intrapulse Interference 4: Characterization and Compensation of the Spectral Phase of Ultrashort Laser Pulses. *Opt. Lett.* 2004, *29*, 775–777.

(18) Hybl, J. D.; Albrecht, A. W.; Gallagher Faeder, S. M.; Jonas, D. M. Two-Dimensional Electronic Spectroscopy. *Chem. Phys. Lett.* 1998, *297*, 307.

Chapter 3: Coherent vibronic wavepacket motion controls excitation energy transfer in the peridinin–chlorophyll protein

Photosynthetic light-harvesting proteins assemble arrays of electronic chromophores to capture solar energy. When the chromophores are closely spaced and strongly interacting, collective optical excitations are produced upon absorption of single photons: the excitation energy is initially delocalized over the chromophore array. Excitation energy transfer can be unusually fast and efficient in light-harvesting proteins when transitions between molecular excitons occur in concert with the vibrational motions of the chromophores. We report herein that a vibronically coherent, nonadiabatic mechanism mediates transfer of excitation energy in the peridinin–chlorophyll protein from marine dinoflagellates. Results from two-dimensional electronic spectroscopy and supported electronic structure calculations reveal a delocalized, two-step pathway from peridinin carotenoids to the chlorophyll terminal emitters in each protein domain. Rapidly damped coherent wavepacket motions report the arrival and trapping of population with retention of vibrational coherence in <50 fs after optical excitation. This coherent regime of dynamics involves the charge-transfer character of the peridinin chromophores. Out-of-plane deformations of the isoprenoid backbones of the peridinins serve as the strongly coupled branching modes, which control a cascade of conical intersections between the donor and acceptor exciton potential surfaces. It may be possible to take advantage of these findings to design unusually efficient light-harvesting materials that exploit the phased vibrational motions of the chromophores to direct the transfer of solar energy to photocatalytic devices and solar cells.

[†] The work presented in this chapter has been adapted for submission for external publishing.
[†] This work was completed in collaboration with Dr. José A. Gascón and Dr. Matthew J. Guberman-Pfeffer at the University of Connecticut.

3.1 Introduction

In several well-characterized examples of photosynthetic light-harvesting proteins,[1–7] absorption of light creates *molecular excitons*, collective optical excitations of strongly interacting pairs or larger clusters of chromophores.[8–10] The excitons result from quantum coherent mixing of the electronic states of the individual chromophores.[11] Captured excitation energy is relayed in some cases in <50 fs to the lowest energy exciton states of the cluster, which are derived mainly from the red-shifted, terminal emitter chromophores. Similar interexciton relaxation processes are observed in the primary electron donor of purple bacterial reaction centers, which is an excitonically coupled pair of bacteriochlorophyll (BChl) molecules,[12,13] and, for example, in a model system consisting of diacetylene-linked perylenediimide dimers.[14] Understanding the mechanisms that contribute to the speed and unidirectionality of these ultrafast excitation energy transfer and relaxation pathways is of great interest because of the urgent need to develop efficient and inexpensive light harvesting and photocatalytic materials.[15] A central question here is how the structure of a light-harvesting protein sustains the delocalized exciton states[16,17] long enough to transfer the captured excitation energy efficiently despite the natural tendency for it to collapse onto a given chromophore.[18,19] In the weak electronic coupling regime typical of widely spaced chromophores, excitation energy hops incoherently in a few ps from one chromophore to another via the Förster mechanism.[20]

In this contribution, we report the results of a two-dimensional electronic spectroscopy (2DES)[21] study of the excitation energy transfer mechanisms involving the short-lived molecular excitons in the peridinin–chlorophyll protein (PCP) from marine dinoflagellates. PCP serves as a water-soluble, peripheral light-harvesting complex that absorbs strongly in the mid-visible, 470–550-nm wavelength range and relays captured the excitation energy to membrane-bound

chlorophyll proteins.[22,23] The structure of the PCP complex (Figure 3.1ab) is a two-fold symmetric, two-domain assembly, each of which contains four peridinin carotenoids (Figure 3.1c) tightly clustered around a single chlorophyll (Chl) (Figure 3.1d).[23] This arrangement is highly distinctive because the chromophore assemblies resemble nanocrystals, lacking any intervening protein scaffolding. Despite the presence only of intermediate electronic coupling strengths,[24–28] several recent investigations have indicated that excitation energy transfer to the Chl *a* acceptors (Figure 3.1e,f) occurs in <20 fs when peridinins absorbing in the long-wavelength onset of the mid-visible absorption band are photoexcited by broadband pulses of light. The results indicate that ultrafast processes account for perhaps two-thirds of the ~90% overall excitation energy transfer yield.[29–32] The remaining third of the excitation transfer yield is attributed to the Förster mechanism, with time constants observed in the 2–3 ps range.[33–39]

The yields of the ultrafast and Förster mechanisms in PCP are apparently determined by a rate competition between ultrafast excitation transfer and nonradiative decay processes. Peridinins in PCP are excited to the second excited singlet state, S_2, by strong $\pi \rightarrow \pi^*$ absorption transitions in the mid visible region of the spectrum (Figure 3.1f). The S_2 state peridinins are capable of transferring excitation to the Chls using ultrafast mechanisms, but the earliest femtosecond spectroscopy studies on PCP showed that nonradiative decay in <150 fs to the first excited singlet state, S_1, limits the yield.[33–37] The Förster excitation transfer process over the ps timescale was accordingly assigned to the S_1 state of peridinin,[33–37,39–41] which obtains an intramolecular charge transfer (ICT) character from its carbonyl substituted γ-lactone ring in conjugation with the isoprenoid backbone.[42–51]

In subsequent work, a possible role in excitation energy transfer in carotenoid-containing light-harvesting proteins by "dark" states along the nonradiative path from the S_2 state to the S_1

state has been identified.[29,52,53] The most widely discussed of these has been labelled S_x.[54,55] Rather than assigning S_x to a discrete electronic excited state of the carotenoid, such as the $1B_u^-$ state suggested by Tavan and Schulten,[56] we recently proposed that S_x is actually a dynamic intermediate, a distorted conformation of the S_2 state in which the carotenoid is evolving rapidly along the torsional and/or pyramidal out-of-plane coordinates of its isoprenoid backbone on the way to a conical intersection (CI) seam with the S_1 state.[53,57–59] We proposed that this idea leads to a natural explanation for the branching of population between the ultrafast and ps mechanisms for excitation energy transfer in PCP. Decay of S_2 to S_x would be expected to collapse the initially delocalized excitation in PCP because S_x would naturally develop an ICT character and an enhanced permanent dipole moment from the out-of-plane motions, which would increase the solvation reorganization energy compared to the interchromophore electronic coupling.[58,60] In this picture, S_x would serve as the principal excitation transfer donor to Chl acceptors via the Förster mechanism. It would retain much of the oscillator strength of the S_2 state, and the carbonyl substituent of peridinin would further enhance the yield by retarding nonradiative decay to the S_1 state.[29,59,60]

As shown in the following, the details of the ultrafast excitation transfer and nonradiative decay processes in PCP can be examined with unusual clarity with 2DES by comparing the wild-type complexes containing Chl *a* acceptors (wtPCP–Chl *a*) with reconstituted complexes containing Chl *b* (rPCP–Chl *b*),[31,61,62] which are constructed using a polypeptide sequence taken from the N-terminal domain of the PCP structure. When reconstituted with pigments, rPCP–Chl *b* assembles a two-fold symmetric dimer complex[61] (Figure 3.1a,b) with almost exactly the same X-ray crystal structure as that for the naturally occurring, heterodimer PCP complex.[31,63] In aqueous solution, wtPCP–Chl *a* forms trimeric aggregates, whereas rPCP–Chl *b* remains

monomeric. The absorption spectra exhibited by the natural and reconstituted complexes nevertheless contain a very similar pattern of four peridinin transitions (Figure 3.1e). The main distinction is that wtPCP–Chl *a* exhibits a fifth, higher energy peridinin absorption transition, which is attributed to splitting of the principal exciton levels by the symmetry-breaking electrostatic differences between the N- and C-terminal domains[64] and by the long-range interchromophore electronic couplings across the two domains.[28] Figure 3.1f shows how the vibronic structure of the Chl *a* and Chl *b* absorption spectra is registered with the peridinin bands. Replacement of Chl *a* with Chl *b* changes the energy gaps from the peridinin energy levels to the vibronic energy levels of the Chls in the two complexes.

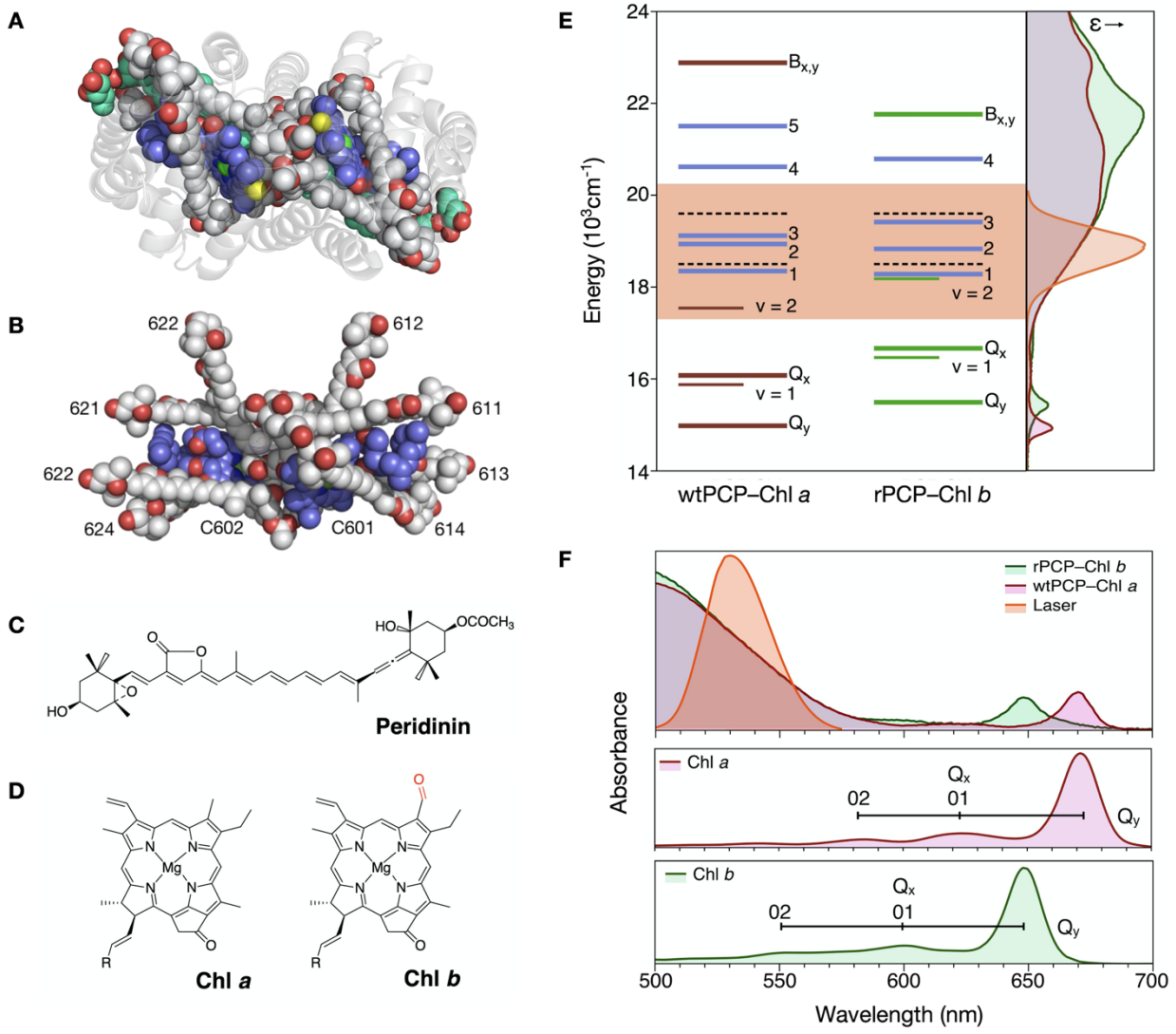

Figure 3.1. Structure and linear spectroscopy of PCP complexes. (a) Structure of rPCP–Chl *b* (PDB structure 2X20)[63] viewed along the two-fold symmetry axis. (b) Structure of the chromophore cluster in rPCP–Chl *b*, with the symmetry axis oriented vertically. In (a) and (b) a space-filling rendering is used for the chromophores, with red spheres used for oxygen atoms. The carbon atoms are blue for Chl *b*, with the formyl group's carbonyl oxygen tinted yellow; the carbon atoms are grey for the peridinins and cyan for the digalactosyldiacylglycerol lipid molecules.[23] The numbering of the chromophores is that from the crystal structure. (c–d) Structures of peridinin, Chl *a*, and Chl *b*, with the formyl oxygen of the latter marked in red. (e) Energy level diagram, after Roscioli et al.,[31] comparing the experimental peridinin (blue, numbered 1–4 for the per1–per4 excitons), Chl *a* (purple), and Chl *b* (green) optical transition frequencies for the wtPCP–Chl *a* and rPCP–Chl *b*[64,65] complexes with the laser excitation spectrum (orange shading) used in the present 2DES experiments. The Chl levels are labelled $B_{x,y}$, Q_x, and Q_y for each complex; the Q_y $v = 1$ and $v = 2$ vibrational levels are estimated from the spectra in panel (f). Dotted lines mark the excitations marked in the 2DES spectra (Figures 3.2 and 3) and used in the global models (Figures 3.4–3.7). (f) Room-temperature absorption spectra

Figure 3.1 (cont'd) from wtPCP–Chl *a* (purple bands) and rPCP–Chl *b* (green bands), with the laser excitation spectrum (orange band) superimposed, as compared with the absorption spectra of five-coordinate[34] Chl *a* (red) and Chl *b* (green) in diethyl ether solution.[66] The Chl *a* and Chl *b* spectra are redshifted here along the frequency axis to align the Q_y transitions with those of wtPCP–Chl *a* and rPCP–Chl *b*, respectively. Assignments for the vibronic structure are marked for the Q_y band; the origin of the underlying Q_x band (00, for S_0 (v = 0) → S_1 (v = 0)) approximately coincides with the Q_y 01 (S_0 (v = 0) → S_1 (v = 1)) transition in five-coordinate Chls.[67,68]

In the present study, we have performed new 2DES experiments on the wtPCP–Chl *a* and rPCP–Chl *b* complexes, combined with the support of a new set of electronic structure calculations, to determine the pathway and mechanism that transfers excitation energy to the Chl acceptors from the peridinin excitons in the middle of the mid-visible absorption band, per1–per3 (Figure 3.1e). The results show for the first time that excitation energy transfer between carotenoids and Chls can involve a vibronically coherent mechanism, with retention of the vibronic phase coherence observed via wavepacket modulations in the Chl product exciton. The strongly coupled branching modes that control the nonadiabatic transfer of population through a cascade of CI seams between the exciton potential surfaces include out-of-plane deformations of the isoprenoid backbone of peridinin, which modulate the charge-transfer character of the donor excitons. In comparison with previous work on other light-harvesting complexes, where incoherent vibronic mechanisms are implicated, these findings raise the prospect that unusually efficient materials for solar energy applications can be designed by exploiting structural features that result in strong coupling of electronic states to key vibrational motions.

3.2 Experimental Procedures

3.2.1 Sample Preparation

PCP preparations containing Chl *a* acceptors (wtPCP–Chl *a*) were isolated by Professor Roger Hiller (Macquarie University) from *Amphidinium carterae* cells using a previously published method.[69] Reconstituted PCP complexes containing Chl *b* (rPCP–Chl *b*) were made with N-terminal domain PCP apoprotein expressed in *Escherichia coli* and reconstituted with peridinin and Chl *b* using previously reported procedures.[70] The expression construct for the N-terminal domain apoprotein from PCP was provided by Professor Hiller. The construct was transformed into *E. coli* JM109 cells (Sigma-Aldrich), and the resulting protein was then expressed and purified. Reconstitution of the apoprotein with Chl *b* was performed as described previously[70] with the minor change that pre-packed HiTrap DEAE fast-flow columns (GE Healthcare) were used instead of DEAE Tris-acryl columns for the final purification step. Reconstituted complexes were concentrated using YM-30 Amicon Centriplus filters.

3.2.2 Femtosecond Spectroscopy

2DES experiments were performed with a newly constructed spectrometer employing a two-beam, pump-probe configuration with adaptive pulse shaping.[71] Excitation pulses were obtained from a noncollinear optical parametric amplifier (NOPA, Spectra-Physics Spirit-NOPA-3H), which was pumped by the third harmonic of a 1.04 μm amplified Yb laser (Spectra Physics Spirit-4W, 400 fs pulses at a 100 kHz repetition rate, 4 W average power). The NOPA's signal beam output spectrum (Figure 3.1ef) was centered at 530 nm (~30 nm FWHM; 495-575 nm usable range). The NOPA's output was split into pump and probe beams by a broadband dielectric beamsplitter (Layertec, Mellingen). Each beam was then processed by an adaptive pulse shaper (FemtoJock and FemtoJock P, respectively, Biophotonic Solutions Inc.) and

compressed by a pair of broadband chirped mirrors (Ultrafast Innovations, Munich). Pulse durations of 15 fs for each beam were determined by running multiphoton intrapulse interference phase scans (MIIPS)[72] on the pump and probe pulse shapers. This procedure was conducted with a thin (<10 μm thickness) β-barium borate second-harmonic generation crystal positioned at the sample's position in the 2DES spectrometer after the laser beams passed through a fused silica cuvette window. The visible fundamental and UV second-harmonic spectra from the crystal were recorded with a compact fiber optic spectrometer and CCD detector (Ocean Optics USB-4000). The residual phase measured at the sample for the optimized pump and probe pulses is shown in Figure A3.1 in the Appendix.

A scanned pair of pump pulses separated by the time interval τ in the three-pulse, stimulated photon-echo pulse sequence for 2DES experiment was then generated by programming the pump beam's pulse shaper to add an additional phase and amplitude mask to that for the optimized pulse at the sample position. A reflective retroreflector in a time-of-flight delay line was scanned to increment the waiting time interval between the second pump pulse and probe pulse, *T*. The detection axis of the 2DES spectrum was measured directly by measuring the pump-induced change in probe transmission of the sample with a home-built 0.2 m spectrograph (300 gr/mm diffraction grating) and a fast CCD detector (Andor Newton 940) using a phase-sensitive detection protocol performed with amplitude modulation of the pump pulses.[73] Blocks of spectra acquired during a 800 ms integration (80000 excitation pulse pairs at a 100 kHz pulse-repetition frequency and 400 Hz amplitude modulation of the pump beam by a mechanical chopper, with a full-width spectral acquisition frequency of 1 kHz) were transferred to the spectrometer's computer using the CCD's kinetic readout mode. The 2048 pixels in the CCD spectra were binned by a factor of eight, yielding 256 channels across the laser bandwidth.

The pump-induced transmission signal was then isolated by Fourier transformation of the modulated spectral time series at each detection wavelength. Fourier transformation of the signal amplitude with respect to the interpulse time interval τ obtains the excitation axis of the 2DES spectrum.

The pump and probe beams were measured to be highly polarized upon exiting the pulse shapers and passing through the chirped mirror pairs; aside from thin neutral density filters, which were used to attenuate the excitation pulse energy to 2 nJ per pulse as measured at the sample, only reflective optics were used to route the two beams to the sample's position. The pump and probe beams were overlapped spatially just after the front cuvette window after focusing with off-axis parabolic mirrors, with the linear planes of polarization of the two beams oriented in parallel.

For use in the 2DES experiments, wtPCP–Chl *a* and rPCP–Chl *b* preparations were suspended in a buffer solution at pH 7.5 containing 50 mM tricine–NaOH and 20 mM KCl. The optical density of the samples was set to 0.3 at 530 nm for a 1 mm optical path length in a static fused silica cuvette. The cross sectional diameter of the laser beams in the overlapped region in the sample was estimated as >100 μm with a Coherent LaserCam-HR II beam profiling camera. Linear absorption spectra were recorded at room temperature with a Shimadzu UV-2600 spectrophotometer. The absorption spectra were recorded before and after the 2DES experiments to determine whether there were any changes due to photochemistry or decomposition of the samples. No changes were noted during these experiments.

Global Target Analysis. Models for the time evolution of the 2DES spectra recorded from the PCP complexes were optimized by global and target analyses with the CarpetView package (Light Conversion). Preliminary models for the amplitude kinetics at marked

coordinates in the 2DES spectra from PCP complexes were determined with the pro Fit (Quantum Software) package using a nonlinear least-squares gradient optimizer and a pascal fit function implementing an iterative reconvolution with the instrument response function. 95% confidence intervals were obtained by modeling the sum of nine 2DES spectra. The amplitudes are plotted with error bars reporting +/− one standard deviation from the average value.

3.3 Results

3.3.1 Linear Spectroscopy and Chromophore Assignments in the PCP complexes

In order to photoselect the per1–per3 peridinin excitons (Figure 3.1ef), we performed new 2DES experiments on the wtPCP–Chl *a* and rPCP–Chl *b* complexes with a laser spectrum centered at 530 nm (15 fs pulse durations), tuned farther to the blue than in our previous work.[30,74] The same laser spectrum was used in the experiments with both complexes in order to allow a strict comparison of the two 2DES data sets. The transition wavelengths corresponding to the excitations of the per1–per3 and Chl excitons in each complex are listed in Table 3.1. These values were determined in previous work by linear absorption spectroscopy[64,65] and are consistent with the assignments of the 2DES spectra that follow. Supporting calculations indicate that optical transitions at 510 nm populate the per2 and per3 excitons, which are predominantly located on peridinin chromophores 611 and 613, respectively (as numbered in Figure 3.1b, following that in the crystal structure).[27,28] Per1, which is principally on peridinin 614, is populated by optical transitions at 540 nm.[27,28] This assignment is in agreement with the spectral reconstruction performed by Ilagan et al.,[64] who identified the peridinin chromophore with the longest wavelength absorption transition via site-directed mutagenesis. Note that the peridinin transitions noted here (and in Figure 3.1ef) indicate the absorption maxima, which correspond to

the 0–1 vibronic transitions with respect to the principal resonance Raman-active C-C/C=C bond-stretching coordinates of the isoprenoid backbone.[27,28]

Table 3.1. Transition wavelengths marked in the 2DES spectra from wtPCP–Chl *a* (Figure 3.2) and rPCP–Chl *b* (Figure 3.3)

Excitation	wtPCP–Chl *a*	rPCP–Chl *b*
Per2,3	510 ± 15 nm	512 ± 17 nm
Per1	540 ± 12 nm	543 ± 11 nm
Chl Q_y 0–2	565 ± 10 nm	——

The red tail of the laser spectrum also spans the 560–575 nm onset of the partially resolved 0–2 absorption transition of the Q_y absorption band of Chl *a* in wtPCP–Chl *a* complexes (Figure 3.1ef). In contrast, in the rPCP–Chl *b* complexes, the 0-2 transition of Q_y for Chl *b* is blue shifted to 550 nm, whereas the overlapping onset of the 0-1 transition is just barely accessible at the red edge of the laser spectrum at >570 nm.

3.3.2 2DES spectra detect excitation energy transfer and electronic dephasing in PCP complexes

2DES experiments on PCP complexes were carried out with a newly constructed spectrometer employing adaptive pulse shapers[72,75] to compress the laser pulses and to apply the three-pulse, stimulated photon echo excitation sequence[21] using a two-beam, pump-probe configuration.[71,76,77] The time interval between the two pump pulses, τ, was scanned by a pulse shaper in the pump beam from 0 fs to 75 fs with 0.5 fs steps to obtain the excitation axis of the 2DES spectrum after Fourier transformation. Longer τ scans produced identical spectra but with a lower signal/noise ratio. Fourier transformation of the signal amplitudes with respect to τ obtains the excitation axis of the 2DES spectrum. The detection axis of the 2DES spectrum is determined directly from the pump-induced change of transmission of the delayed probe pulse

through the sample, which is measured using a spectrograph and a CCD detector. The waiting time interval between the second pump pulse and the probe pulse, *T*, was scanned from 0 fs to 25 fs with a 2.5 fs spacing; the 25 fs to 300 ps range was then sampled with an interval increasing from 5 fs to 100 ps. Owing to the use of the pump–probe experimental geometry and amplitude modulation of the pump-pulse pair, the 2DES spectra are intrinsically autophased.[71] The spectra obtained using this approach are the sum of the rephasing and non-rephasing nonlinear optical pathways.[78] Each spectrum reported in this work was obtained as the average from that acquired in nine τ scans, and the reported amplitudes are normalized with respect to that of the global maximum in the entire (τ,*T*) dataset. Additional experimental details are reported below in the Experimental Procedures section.

Figures 3.2 and 3.3 compare a set of 2DES spectra from wtPCP–Chl *a* and rPCP–Chl *b* complexes recorded with the 530 nm laser pulses over the waiting time $T = 5–500$ fs range. The effective wavelengths for the per1–per3 transitions and for the Chl Q_y 0-2 transition (for wtPCP–Chl *a*) from Table 3.1 are marked on the $T = 5$ fs spectra in Figures 3.2 and 3.3. The Chl *b* Q_y 0–2 transition at 550 nm is not marked in Figure 3.3 because it underlies the much stronger per1 absorption transition.

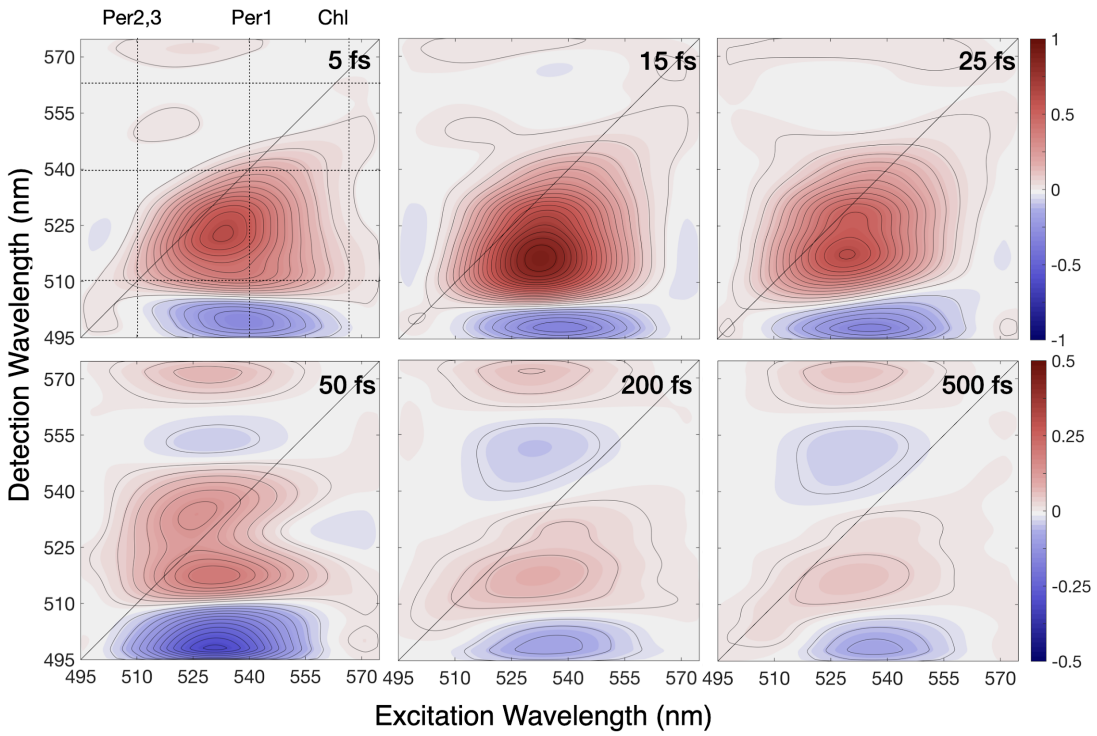

Figure 3.2. Time evolution of 2DES spectra measured at room temperature (23°C) with wtPCP–Chl *a* preparations over the waiting time $T = 5$ to 500 fs range.

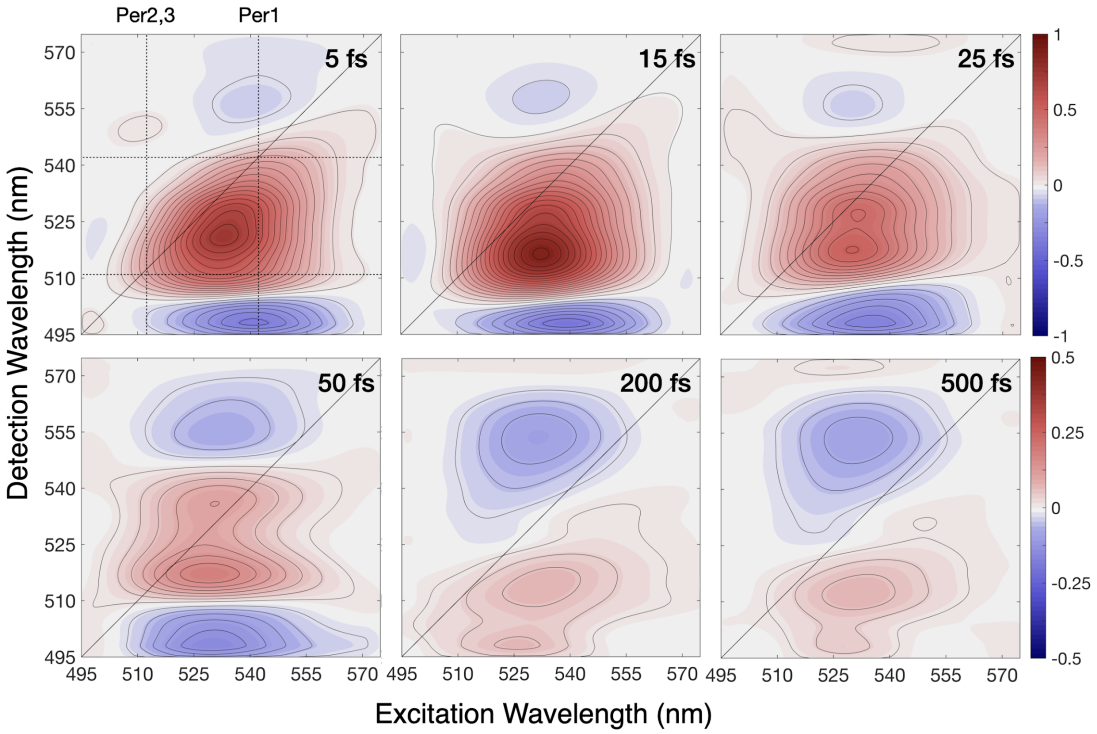

Figure 3.3. Time evolution of 2DES spectra measured at room temperature (23°C) with rPCP–Chl *b* over the waiting time $T = 5$ to 500 fs range.

By inspection of the 2DES spectra from the PCP complexes, one can easily identify several features arising from excitation energy transfer and from electronic dephasing. At short waiting times *T*, the 2DES spectra exhibit positive-going ground-state bleaching (GSB) and stimulated emission (SE) signals along the diagonal. As indicated by Figure 3.1, these signals principally arise from photoexcitation of the per1–per3 excitons over the 510–550 nm range, but the Chl acceptors also contribute at longer wavelengths. The GSB and SE signals are extensively broadened with respect to the antidiagonal direction by electronic dephasing even at short delays *T*. Negative-going excited-state absorption (ESA) signals are observed initially below the diagonal (to shorter detection wavelengths) but increasingly above the diagonal (to longer detection wavelengths) at longer waiting times in both complexes. The latter were detected previously in one-dimensional heterodyne transient grating experiments.[29] Excitation energy

transfer processes are reported by the formation of positive-going cross peaks above the diagonal and by the decay of the diagonal GSB and SE signals as excitation energy flows from the effectively degenerate per2 or per 3 (per2,3 in the following) excitons to the per1 exciton and then to the Chl acceptor in <50 fs in both complexes. In fact, the main difference between the 2DES spectra from wtPCP–Chl *a* and rPCP–Chl *b* is the observation of the Chl cross peaks lining up with the $v = 2$ transition of Q_y for Chl *a* and only weakly at the blue edge of the $v = 1$ transition for Chl *b*. This difference definitively identifies these cross peaks as arising from population of the Chl acceptors.

3.3.3 Global and Target Modeling of the 2DES spectra from PCP complexes

The responses initiated by optical excitations of the per2,3 or per1 excitons (Table 3.1)[64,65] were isolated using global and target modeling.[79] The method we used describes the signal amplitudes for a given excitation in the 2DES spectra as a linear combination of the evolution-associated difference spectra (EADS) weighted by the time-dependent populations for each of the detected spectrokinetic species in a kinetic scheme. The results are shown in Figures 3.4–3.7. A more advanced approach was introduced by Thyrhaug et al.[80] in a recent 2DES study of excitation energy transfer in the Fenna−Matthews−Olson (FMO) BChl *a* complex; the exciton transitions were determined by the linear absorption spectrum, and then the global models for the responses for each excitation were simultaneously optimized. Niedringhaus et al.[13] subsequently used a similar global modeling approach with incorporation of the energies of charge-transfer intermediate states to analyze the 2DES spectra from the purple bacterial reaction center. A possible advantage of separately optimizing the models for each excitation, as performed here, is that one can compare the response for the per1 exciton following optical preparation of the per2,3 excitons with that following direct optical preparation of the per1 exciton to determine the

impact on the mechanism transferring excitation energy to the Chl acceptors. 2DES allows us to monitor these selective photoexcitations in parallel in the same experiment.[21]

The results from our previous heterodyne transient grating experiments on wtPCP–Chl *a*[29] and empirical multicomponent modeling of the 2DES signal amplitudes at selected coordinates (as presented in the Appendix) determined the framework of the initial kinetic scheme and the starting estimates for the time constants in the global models, respectively. The final kinetic schemes reported in Figures 3.4a–3.7a were obtained after multiple iterations of the global and target analysis. In these figures, the spectrokinetic species that contribute to the global model for a given excitation are framed by squares. The species that are not enclosed by squares in the kinetic schemes do not contribute signals for the given excitation. As an example, in Figures 3.5 and 3.7, the first square in the kinetic scheme is the optically excited per1 exciton. This species is labeled S_2 to identify the peridinin electronic state character. The time evolution of the population for each species is plotted in Figures 3.4b–3.7b using the same colors used for the boxes in the kinetic scheme. Figures 3.4c–3.7c then present the corresponding EADS. The optimized rate constants and confidence intervals for the global models are listed in Table 3.2.

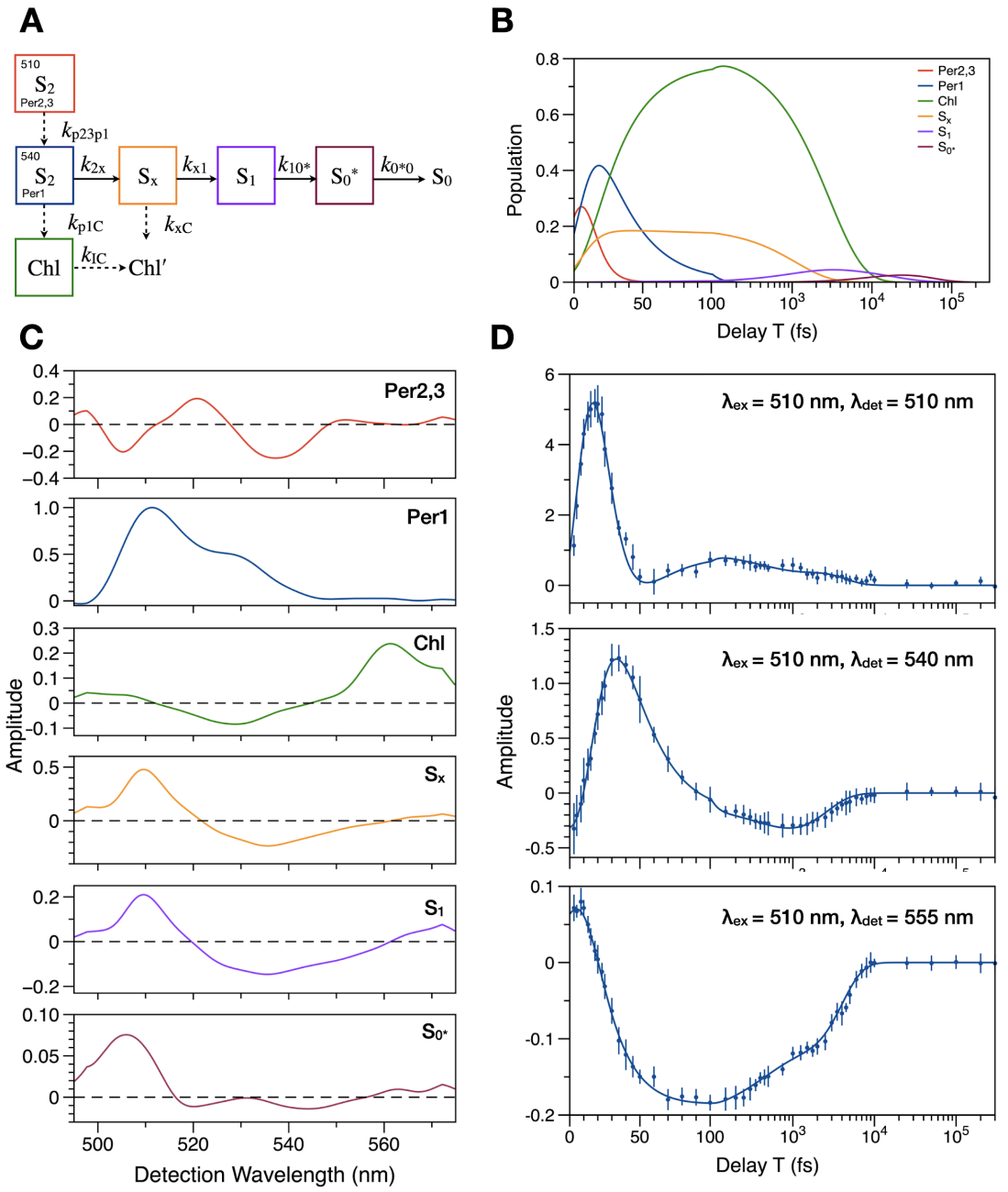

Figure 3.4. Global modeling of the response after optical excitation of the per2,3 excitons at 510 nm (Table 3.1) for the 2DES spectrum from wtPCP–Chl *a* (Figure 3.2): (a) Kinetic scheme, with the spectrokinetic species that contribute to the 2DES signal framed with colored boxes. (b) Semilogarithmic plots of the time evolution of the populations of the spectrokinetic species, with the time axis split at 100 fs and using the same color scheme. (c) Evolution associated difference spectra (EADS) for the spectrokinetic species. (d) Time evolution of the 2DES amplitude at selected coordinates, with the global model's amplitude superimposed; the bars report 95% confidence intervals for the amplitudes. The rate constants for the spectrokinetic scheme returned by the optimized global model are tabulated in Table 3.2.

Table 3.2. Time constants for the excitation energy transfer and nonradiative processes in the kinetic schemes for the global modeling (Figures 3.4–3.7) of the 2DES response after optical excitation of the per2,3 and per1 excitons (Table 3.1) in wtPCP–Chl *a* and rPCP–Chl *b*

	wtPCP–Chl *a*		**rPCP–Chl *b***	
	Per2,3	**Per1**	**Per2,3**	**Per1**
$\mathbf{1/k_{p23p1}}$	10 ± 3 fs	--	13 ± 2 fs	--
$\mathbf{1/k_{p1C}}$	24 ± 1 fs	26 ± 2 fs	29 ± 2 fs	28 ± 4 fs
$\mathbf{1/k_{IC}}$	3.2 ± 0.1 ps	2.9 ± 0.1 ps	3.1 ± 0.6 ps	3.2 ± 2.4 ps
$\mathbf{1/k_{2x}}$	35 ± 6 fs	38 ± 3 fs	35 ± 4 fs	37 ± 1 fs
$\mathbf{1/k_{x1}}$	3.7 ± 0.5 ps	3.6 ± 0.5 ps	3.7 ± 0.5 ps	3.5 ± 0.2 ps
$\mathbf{1/k_{xC}}$	1.3 ± 0.2 ps	1.2 ± 0.5 ps	1.9 ± 0.3 ps	2.2 ± 0.3 ps
$\mathbf{1/k_{10*}}$	17.5 ± 2.1 ps	18.1 ± 1.8 ps	17.3 ± 1.9 ps	18.0 ± 1.3 ps
$\mathbf{1/k_{0*0}}$	27.2 ± 3.0 ps	30.0 ± 2.2 ps	28.4 ± 3.0 ps	29.1 ± 2.8 ps

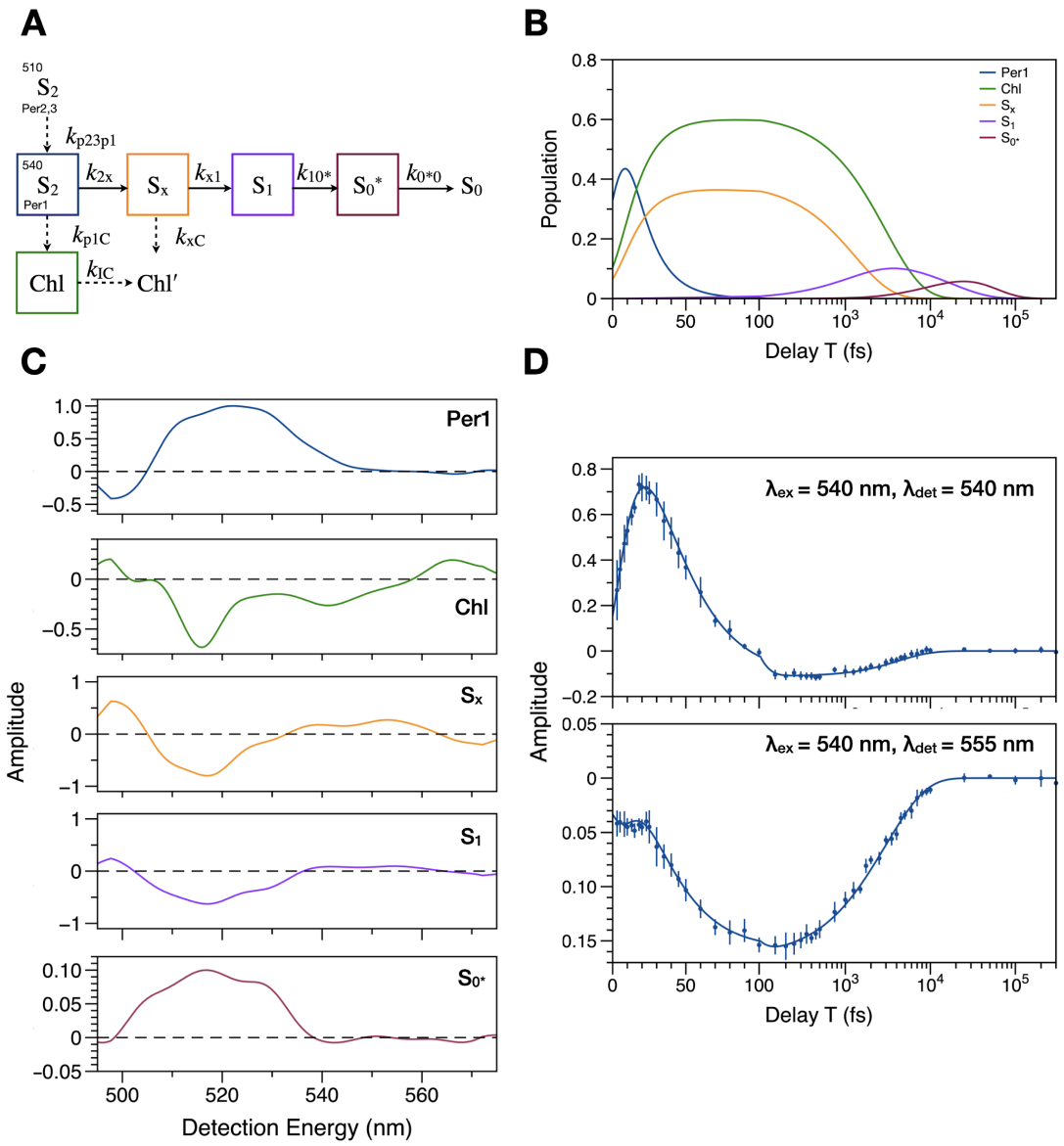

Figure 3.5. Global modeling of the response after optical excitation of the per1 exciton at 540 nm (Table 3.1) for the 2DES spectrum from wtPCP–Chl *a* (Figure 3.2): (a) Kinetic scheme, with the spectrokinetic species that contribute to the 2DES signal framed with colored boxes. (b) Semilogarithmic plots of the time evolution of the populations of the spectrokinetic species, with the time axis split at 100 fs and using the same color scheme. (c) EADS for the spectrokinetic species. (d) Time evolution of the 2DES amplitude at selected coordinates, with the global model's amplitude superimposed; the bars report 95% confidence intervals for the amplitudes. The rate constants for the spectrokinetic scheme returned by the optimized global model are tabulated in Table 3.2.

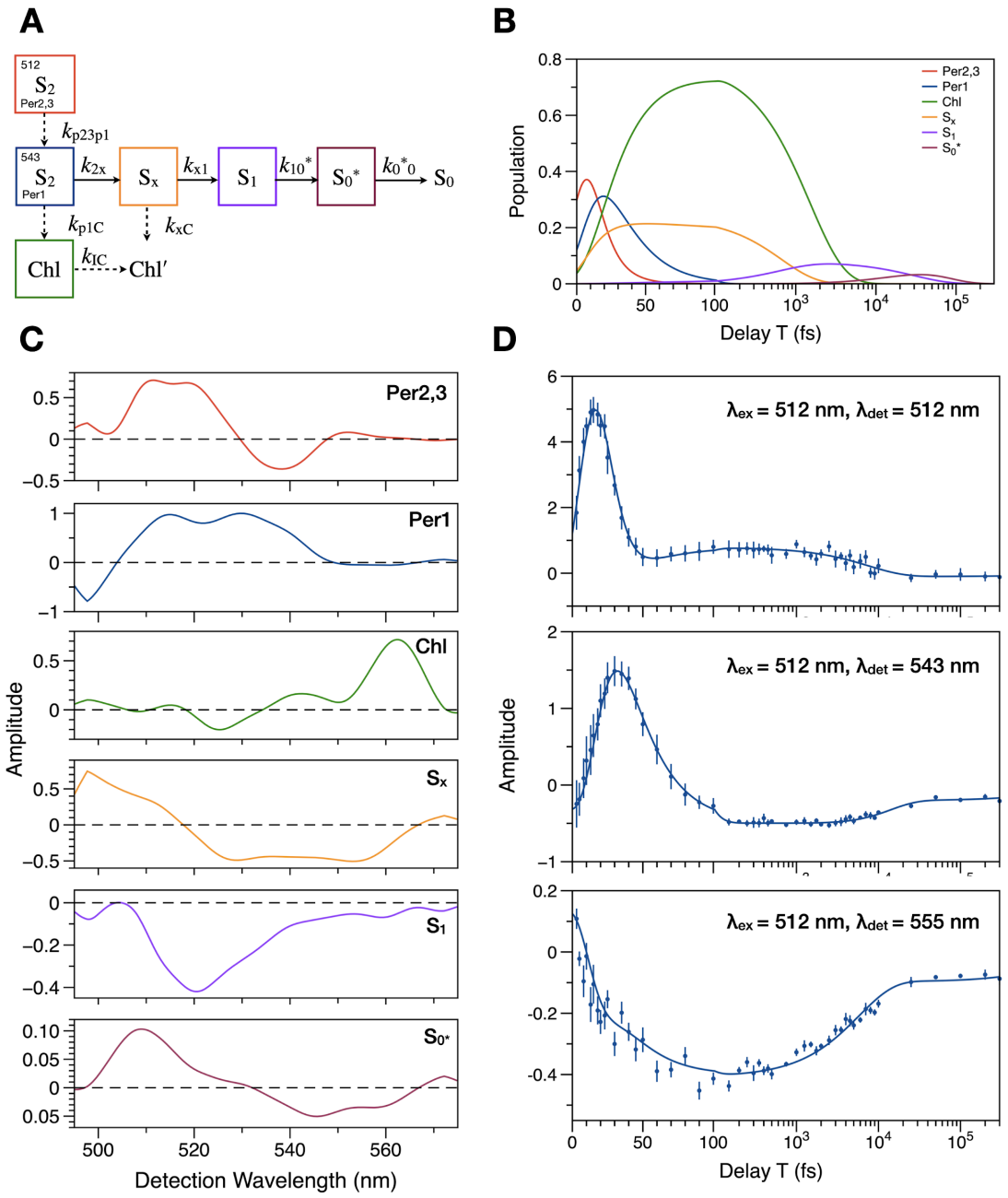

Figure 3.6. Global modeling of the response after optical excitation of the per2,3 excitons at 512 nm (Table 3.1) for the 2DES spectrum from rPCP–Chl *b* (Figure 3.3): (a) Kinetic scheme, with the spectrokinetic species that contribute to the 2DES signal framed with colored boxes. (b) Semilogarithmic plots of the time evolution of the populations of the spectrokinetic species, with the time axis split at 100 fs and using the same color scheme. (c) EADS for the spectrokinetic species. (d) Time evolution of the 2DES amplitude at selected coordinates, with the global model's amplitude superimposed; the bars report 95% confidence intervals for the amplitudes. The rate constants for the spectrokinetic scheme returned by the optimized global model are tabulated in Table 3.2.

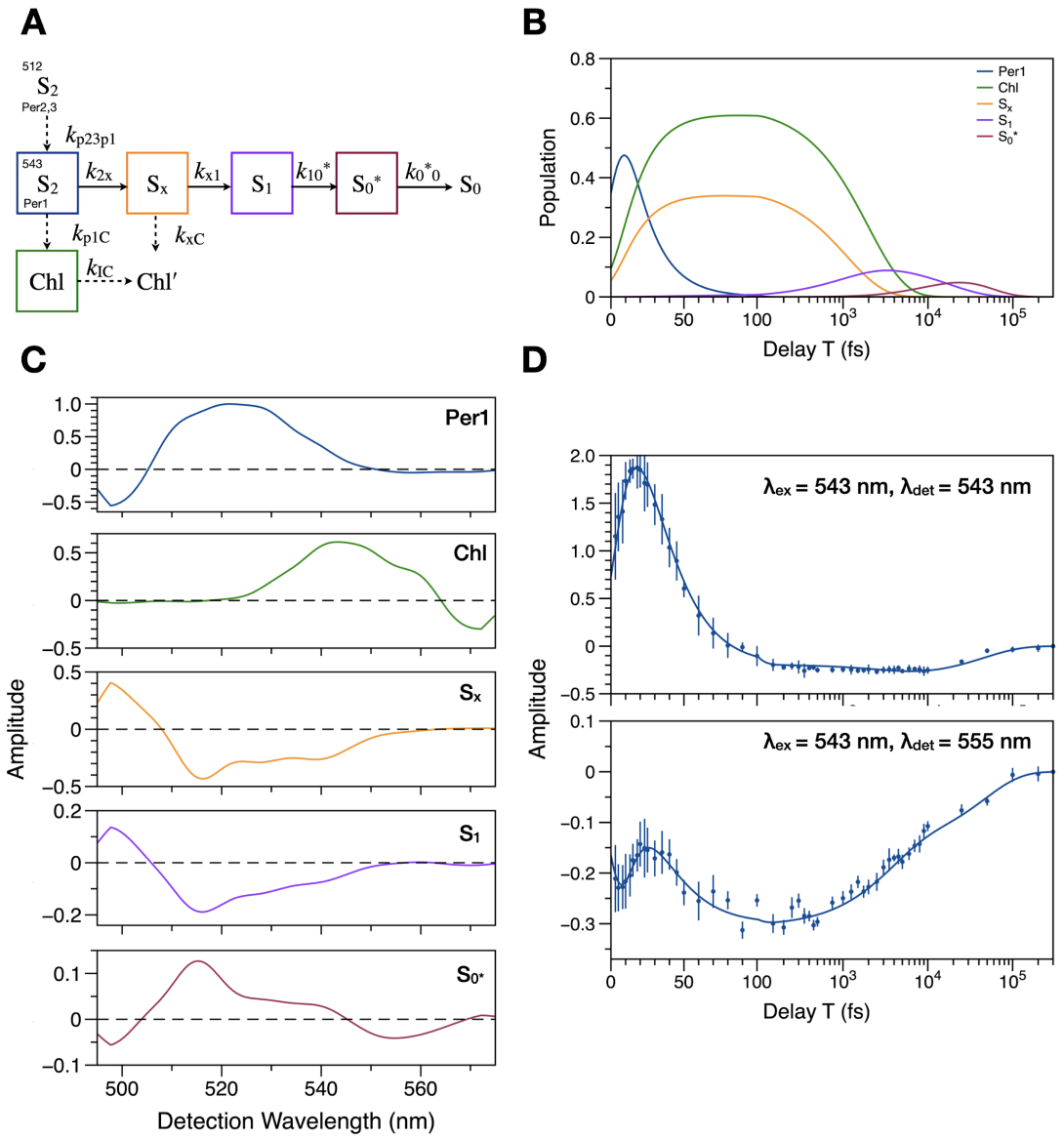

Figure 3.7. Global modeling of the response after optical excitation of the per1 exciton at 543 nm (Table 3.1) for the 2DES spectrum from rPCP–Chl *b* (Figure 3.3): (a) Kinetic scheme, with the spectrokinetic species that contribute to the 2DES signal framed with colored boxes. (b) Semilogarithmic plots of the time evolution of the populations of the spectrokinetic species, with the time axis split at 100 fs and using the same color scheme. (c) EADS for the spectrokinetic species. (d) Time evolution of the 2DES amplitude at selected coordinates, with the global model's amplitude superimposed; the bars report 95% confidence intervals for the amplitudes. The rate constants for the spectrokinetic scheme returned by the optimized global model are tabulated in Table 3.2.

The example transients shown with detection over the 510–555 nm region associated with the peridinin excitons in Figures 3.4d–3.7d show that the optimized global models provide an adequate description of the overall response reported in the 2DES spectra given the signal/noise ratio obtained. Comparison of the signal amplitude with the model response is well within the 95% confidence intervals reported by the error bars even at short waiting times *T* except where oscillatory signals from coherences were observed, as discussed below.

3.3.4 Detection of an Ultrafast Excitation Transfer Pathway in PCP complexes

The first result from the global and target analysis of the 2DES datasets, above, is that a two-step ultrafast excitation transfer pathway is observed in the PCP complex after optical excitation of the per2,3 excitons. The per1 exciton serves as an intermediate, accepting excitation from per2,3 and relaying it to the Chl acceptors in <50 fs. For wtPCP–Chl *a*, as an example, Figures 3.4d and 3.6d show directly that population from the optically prepared per2,3 exciton decays synchronously with the rise of population in the per1 exciton with a 10 fs time constant. This time constant is shorter than the 21-fs instrument response width estimated from the 15 fs excitation pulses, so it is likely to be only approximately determined despite the relatively tight confidence intervals reported in Table 3.2. The same ~25 fs time constant for the downhill kinetics from per1 to the Chl acceptor is observed, within experimental precision, if per1 is optically excited rather than via excitation energy transfer from per2,3. The excitation transfer times in rPCP–Chl *b*, ~13 fs and ~28 fs, respectively, are consistently longer than those in wtPCP–Chl *a* but only by a few fs.

For the 510 nm excitations in wtPCP–Chl *a* (Figure 3.4c) and rPCP–Chl *b* (Figure 3.6c), the EADS corresponding to instantaneous excitation of the per2 and per3 excitons have comparable features. The positive-going net GSB/SE character centered at 520 nm in these

EADS is apparently overlapped by an underlying broader region of ESA extending both to the blue and red. The ESA band largely disappears in the subsequent EADS from the per1 acceptor, when populated as an intermediate (Figures 3.4 and 3.6) or when optically excited directly at 540 nm in wtPCP–Chl *a* or rPCP–Chl *b* (Figures 3.5 and 3.7). As corroborated by supporting electronic structure calculations, this change in ESA character is consistent with a change in the extent of delocalization of the chromophore cluster in PCP as excitation moves down the pathway. As pointed out previously,[1,30,81,82] in addition to GSB and SE transitions, the exciton states for a chromophore cluster uniquely exhibit ESA transitions accessing a manifold of doubly excited exciton states. As the delocalization collapses in a chromophore cluster, these ESA transitions disappear because the doubly excited states vanish.

Next in the kinetic scheme, the Chl acceptor from per1 also exhibits a bipolar EADS, with a relatively weak region of negative-going ESA in the blue overlapping with a sharper net positive region from net PB/SE in the >545 nm region for wtPCP–Chl *a* and for the >535 nm region for rPCP–Chl *b*. The positive regions overlap with the Chl Q_y vibronic structure in the red part of the laser spectrum (Figure 3.1f). Given the decay of the diagonal regions of the 2DES spectra that accompanies the rise of population for the Chl acceptor in the global model, the Chl EADS should be assigned to a predominantly localized excitation. This conclusion is also supported by electronic structure calculations. These EADS are relatively noisy because the oscillator strength is weak for the Chl acceptor in the probed region of the spectrum; in both complexes, the positive spectral regions are subsumed by overlapping ESA signals in the 2DES spectra from peridinins in the S_x and S_1 states (Figures 3.2 and 3.3). Only in the 2DES spectra from wtPCP–Chl *a* (Figure 3.2) does the amplitude from the Chl acceptor rise enough to be identified clearly as a cross peak, which indicates a SE signal from population deposited in the

Q_y $v = 2$ vibronic band of Chl *a* (Figure 3.1f). As noted above, a weaker cross peak from the Chl acceptor in the rPCP–Chl *b* data set (Figure 3.3) is observed at detection wavelengths >570 nm. This spectral region is just at the blue edge of the Q_y $v = 1$ transition in Chl *b*. These observations clearly show that the $v = 1$ level of Q_y receives the excitation in the Chl *b* case instead of $v = 2$, which is almost degenerate with per1. The rates for the downhill excitation transfer from per1 to Chl in wtPCP–Chl *a* and rPCP–Chl *b* are nevertheless quite similar despite that for the latter requiring a somewhat larger energy gap.

The Chl components in the global models decay with essentially the same time constant, ~3.1 ps, in both complexes (Table 3.1). Given the long lifetime observed for the Chl S_1 (Q_y) state in PCP, which permits Chl-to-Chl excitation energy transfer in a given PCP monomer and between PCP monomers in the wtPCP–Chl *a* trimer with time constants of 6.8 ps and 350 ps, respectively,[34,41,64] an assignment of the 3.1 ps decay component to vibrational cooling and/or reorganizational dynamics should be considered first. Vibrational relaxation in metalloporphyrins typically occurs on the 3–10 ps timescale, with the actual time constant strongly dependent on the amount of vibrational energy to be dissipated and the nature of the surrounding media that sinks it.[83–85] The loss of positive signal here would principally involve a shift of the SE to longer wavelengths as the $v = 2$ or $v = 1$ population relaxes to establish a Boltzmann distribution at the temperature of the surroundings, leaving nearly all of the population in the Q_y $v = 0$ level. In fact, Bautista et al. observed a similar time constant, 3.2 ps, for a rising transient at 670 nm for Q_y $v = 0$ transition in pump-probe studies.[33] An additional possible contribution would be that arising from reorganization of the protein and chromophore-derived surroundings upon localization of excitation at the Chl acceptors,[8,86] which would contribute an additional red shift of the SE character.

3.3.5 Nonradiative Decay by Peridinins and Förster Excitation Transfer

The flow of excited-state population branches at the per1 exciton in the second row of the kinetic scheme in Figures 3.4–3.7, with the ultrafast excitation transfer pathway to Chl competing with a peridinin nonradiative decay pathway. (A parallel nonradiative decay pathway from per2,3 was not included in the kinetic scheme for simplicity and to favor convergence; further, the model indicates it would be strongly kinetically disfavored owing to the faster per2,3 to per1 step.) The nonradiative decay branch accounts for only about a third of the optically prepared population in the per2,3 or per1 excitons because nonradiative decay to yield the intermediate labelled S_x is slower than excitation transfer to the Chls, with time constants of ~36 fs and ~25 fs, respectively (Table 3.2). S_x then decays nonradiatively to yield the S_1 state in ~3.6 ps. These nonradiative time constants are essentially the same in the wtPCP–Chl *a* and rPCP–Chl *b* complexes (Table 3.2), which is consistent with an assignment of these kinetic phases in the responses to peridinin photophysics.

As was also observed in the earlier heterodyne transient grating experiments,[29] the EADS for S_x and S_1 are almost identical in shape over the probed region, with a broad region of ESA being the main features; note that earlier pump–continuum probe studies show that the ESA signal from S_1 extends well to the red of the limits of the present laser spectrum.[44] The ESA band from S_x is flanked by PB character in the blue and a weak SE character in the red in the present models. The observed ESA region for S_1 is somewhat stronger and very slightly blue shifted from that for S_x. This comparison suggests initially that the S_x species in the kinetic scheme could be assigned to a vibrationally excited (or "hot") S_1 state, the assignment suggested in nearly all of the previous studies of excitation transfer in PCP for the species produced promptly by nonradiative decay from the peridinin S_2 state.[33–39]

But as noted above, we continue to favor an alternative assignment of the S_x compartment to a dynamic intermediate, a conformationally distorted S_2 state structure, because S_x and S_1 have different electronic properties and are kinetically distinct in the global models.[58,60] S_x serves in the present models as an excitation energy transfer donor to Chl with a time constant of ~1.2 ps in wtPCP–Chl *a* and ~2.1 ps in rPCP–Chl *a*. The earlier transient grating results indicated that this segment of the kinetic scheme accounts for about a third of the overall ~90% yield of excitation transfer from peridinin to Chl in PCP.[29] The Chl' compartment that serves as the acceptor from S_x in the kinetic scheme does not contribute a signal over the probed bandwidth, so Chl' is probably the $v = 0$ level of the Q_y band. Note that this assignment indicates that pump–probe transients at measured at the $v = 0$ transition of Q_y are kinetically complicated due to inclusion of several components: an ultrafast component due to GSB when the $v = 2$ or $v = 1$ are populated by excitation transfer from per1, then an intermediate ps component due to GSB and SE owing to the Förster energy transfer from S_x in our models, and lastly a 3.2 ps SE component due to the vibrational cooling from $v = 2$ or $v = 1$. Thus, depending on the excitation pulse wavelength, bandwidth, and duration used in previous pump–probe experiments, a range of effective exponential rise times at $v = 0$ attributed to excitation energy transfer have been determined.

The second branch of the kinetic scheme at the S_x state corresponds to nonradiative decay with a 3.6 ps time constant to yield the S_1 state. The total yield of the S_1 state is about 10%. The S_1 compartment in the global models exhibits a long lifetime, ~18 ps, in both wtPCP–Chl *a* and rPCP–Chl *b*. As concluded previously,[29] the long lifetime excludes the S_1 compartment as serving as an excitation energy donor to the Chl acceptors because the decay is much slower than the Förster excitation energy transfer rate. Bautista et al. argued previously that this fraction of

the yield could play a role in photoprotection mechanisms.[33] In the kinetic scheme, S_1 then decays to yield a nonequilibrium ground state species, S_0*, which exhibits an even longer lifetime in both complexes, ~29 ps. This behavior is qualitatively consistent with that observed previously for β-carotene and peridinin in solution, where a nonequilibrium ground state species was detected in heterodyne transient grating signals by comparing the ground-state recovery time constants in the dispersion and absorption components of the third-order nonlinear optical signal.[57,58] The EADS detected here in the global models for S_0* exhibits a bipolar profile, which would be expected for the photoinduced absorption spectrum from a nonequilibrium ground-state intermediate. A possible structural assignment for S_0* would be a conformationally displaced peridinin species.[59,60]

3.3.6 Vibronic coherences are observed in the Chl product exciton

Relatively deep and rapidly damped amplitude modulations are observed for the Q_y $v = 2$ cross peak in the wtPCP–Chl *a* dataset with excitation of the per2,3 or per1 excitons and detection over the >565 nm region of the detection axis (Figure 3.8ab). With both peridinin excitations, the oscillations exhibit a rising modulation amplitude at short waiting times $T < 50$ fs. Direct optical excitation of the $v = 2$ transition for Chl *a* in wtPCP–Chl *a*, in contrast, results in an instrument-limited rise of the amplitude on the diagonal of the 2DES spectrum and much weaker and more slowly damped oscillations carried by a 3.2 ps exponential decay (Figure 3.8c). The $v = 2$ region of Q_y for Chl *b* lacks corresponding amplitude modulations in the rPCP–Chl *b* dataset (Figures 3.6d and 3.7d), but the onset of the $v = 1$ transition is deeply modulated at the red edge of the spectrum with excitation of per1 (Figure 3.8d). Especially because these modulations exhibit a delayed rise with peridinin excitations, these signals are unlikely to be artifacts arising from "coherence spike" overlaps of the pump and probe excitation pulses at short

waiting times T.[87] The oscillations remain significant with respect to the confidence intervals compared to the trend of the global models over at least the $T = 0$ – ~600 fs range.

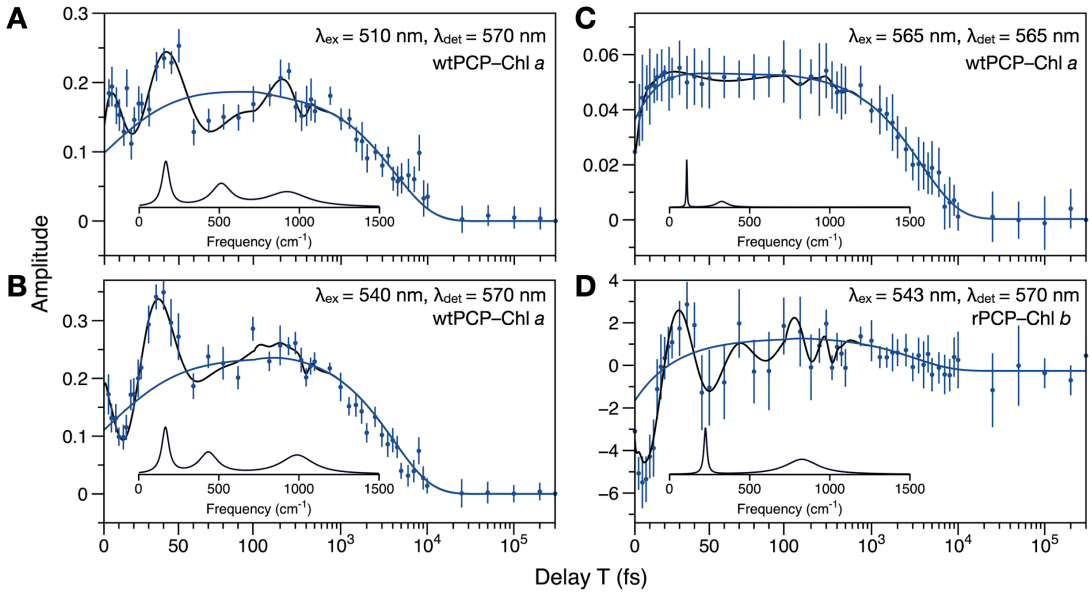

Figure 3.8. Amplitude transients detected at the Chl acceptor in the 2DES spectra from PCP complexes (Figures 3.2 and 3.3). In wtPCP–Chl *a*: (a) with excitation of the per2,3 exciton at 510 nm, (b) with excitation of the per1 exciton at 540 nm, and (c) with direct excitation of Chl *a* at 565 nm. In rPCP–Chl *b*: (d) with excitation of per1 at 543 nm. In (a,b, and d), the blue curves plots the amplitude of the global model with excitation of per2,3 (Figure 3.4) or per1 (Figures 3.5 or 3.7); the model in (c) is an single-exponential decay with a 3.2 ± 0.3 ps time constant, with convolution with the 21-fs instrument response function. Black curves plot models for the modulated residuals, as described by the parameters listed in Table 3.3 and by the spectra shown in the insets; each model is convoluted with the instrument response function. The blue bars report the 95% confidence intervals for the amplitudes at each point.

Table 3.3. Model parameters for the modulation components detected in the amplitude transients detected at the Chl acceptor at 570 nm in the 2DES spectra from PCP complexes (Figure 3.8).

PCP Complex and Excitation	***A***	**ω (cm^{-1})**	**φ (rad)**	**τ (fs)**
wtPCP–Chl *a* Per2,3[a,b]	0.023	930 ± 50	3.00	34 ± 8
	0.016	510 ± 20	1.40	71 ± 10
	0.019	170 ± 10	0.40	190 ± 80
wtPCP–Chl *a* Per1[a,c]	0.019	990 ± 50	0.90	43 ± 10
	0.012	430 ± 20	3.10	76 ± 20
	0.010	170 ± 10	0.80	200 ± 60
rPCP–Chl *b* Per1[a,d]	0.017	825 ± 60	1.50	40 ± 10
	0.035	220 ± 20	0.60	170 ± 70
wtPCP–Chl *a* Chl[e]	0.0019	330 ± 50	0.50	120 ± 10
	0.0012	110 ± 30	0.40	320 ± 90

a. sum of rising, damped cosinusoids, $A_r\ (1 - \exp(-T/\tau_r))\ \Sigma_i\ A_i \cos(\omega_i T - \varphi_i) \cdot \exp(-T/\tau_i)$
b. $A_r = 0.028$, $\tau_r = 24 \pm 3$ fs
c. $A_r = 0.021$, $\tau_r = 23 \pm 3$ fs
d. $A_r = 0.016$, $\tau_r = 25 \pm 5$ fs
e. sum of damped cosinusoids, $\Sigma_i\ A_i \cos(\omega_i T - \varphi_i) \cdot \exp(-T/\tau_i)$.

Although full Fourier amplitude maps of the amplitude modulations detected over a whole 2DES spectrum have been used previously[17,88] especially to identify stimulated Raman coherences in light-harvesting proteins, we have chosen here to apply kinetic models with convolution with the instrument response function for the modulated Chl cross peak signals in order to quantify the delayed rising character, which is likely to be of dynamical and mechanistic significance. The initial oscillations in the waveforms observed when per2,3 or per1 is optically excited in wtPCP–Chl *a* are detected ~10 fs earlier for the per1 excitation (Figure 3.8b) compared to those for the per2,3 excitation (Figure 3.8a). This time shift corresponds almost exactly to that for moving the excitation from per2,3 to the per1 intermediate (Table 3.2). The per1 transient in rPCP–Chl *b* at the the Chl *b* $v = 1$ transition (Figure 3.8d) has a comparable delayed rising profile. Further, the modulation amplitude in these signals rises with a 23 fs time constant (Table 3), which exactly matches the time constant in the global models for the per1 to Chl excitation transfer step (Table 3.2). These observations indicate that the oscillations report the transfer of excited-state population from per1 to the Chl acceptor rather than arising from an electronic quantum beating response. This point will be further clarified when we discuss the electronic quantum beat signals detected below the diagonal of the 2DES spectrum from wtPCP–Chl *a*.

The models for the oscillatory signals observed in the Chl *a* cross peak with excitation of the per2,3 or per1 excitons include essentially the same set of three damped modulation components (Figures 3.8ab) but with different relative intensities, possibly due to the short damping times. The corresponding spectral lineshapes for the modulation components are very broad (as shown in the insets in Figure 3.8), hence the mode frequencies are relatively poorly determined due to covariance with the damping time constants. Still, the frequencies are centered

in characteristic ranges that allow reasonable structural assignments. The modulation component at 510 cm^{-1} and 430 cm^{-1}, respectively, has a somewhat lower frequency than that normally associated with local C=C torsional distortions of a conjugated polyene,[89] so this component likely corresponds to torsional motions of a larger segment of the isoprenoid backbone of peridinin. The more rapidly damped 930 cm^{-1} or 980 cm^{-1} component, however, closely matches the range of frequencies expected for a hydrogen out-of-plane (HOOP) deformation mode of a carotenoid.[90] Both of these components are associated with twisting or pyramidal distortions of the isoprenoid backbone of a peridinin chromophore.

The third oscillatory component carried by the Chl cross peak signals in Figures 3.8ab has a lower frequency, 170 cm^{-1}, and a longer damping time, ~200 fs, than the other components. This component is consistent with vibrational motions from the Chl acceptor. The frequency is in the range previously reported for out-of-plane deformations of chlorophyll and porphyrin macrocycles in resonance Raman studies,[91] and a similar frequency was observed in 2DES studies of excitation transfer in the FMO BChl *a* complex.[17] Note that strong coupling of vibrational modes with low frequencies in Chls is thought to arise via out-of-plane modulation of the π orbital overlap with neighboring chromophores.[91,92] The damping time for this modulation component is still shorter than that usually associated with a stimulated Raman coherence. In comparison, the weaker modulations observed at the diagonal Chl *a* signal (Figure 3.8c) are somewhat more slowly damped than their counterparts in the signals observed with peridinin excitations.

The model presented for the modulated signal observed in the Chl cross peak in the rPCP–Chl *b* complex (Figure 3.8d) includes only two rising cosinusoidal components, given the lower signal/noise ratio and the stronger ESA background observed at the red limit of the

spectrum. The signal nevertheless is comparable in rise time and shape to that for the per1 excitation in wtPCP–Chl *a* (Figure 3.8b), which supports assignment of this signal to the cross peak in the rPCP–Chl *b* complex. Given the broader confidence intervals, the 850 cm^{-1} component corresponds to the rapidly damped peridinin HOOP mode, and the more slowly damped 220 cm^{-1} component is likely the Chl mode.

3.3.7 Electronic decoherence and coherence transfer between the exciton levels in PCP

We can refine the preliminary conclusion that the oscillatory transients observed at the Chl cross peaks arise from population transfer from the optically prepared peridinin excitons by comparing them to those involving electronic quantum beating and by estimating the timescales for electronic decoherence in the PCP complex using the rate of linebroadening in the 2DES spectra. Figure 3.9 compares the instantaneous 2D-EADS from wtPCP–Chl *a* and rPCP–Chl *b*, which were determined by global modeling over the entire excitation axis range of the 2DES spectra. The 2D-EADS spectrum is useful because it is calculated with deconvolution with respect to the waiting time *T* of the instrument response function's 21-fs width. Accordingly, especially in the spectrum from wtPCP–Chl *a* (Figure 3.9a), there is partial relief from the effects of inhomogeneous linebroadening, which very rapidly broadens the 2DES spectrum in the antidiagonal direction. Further, the sharpened instantaneous 2D-EADS spectrum from wtPCP–Chl *a* reveals cross peaks arising from quantum coherence across the chromophores in the excitation energy transfer pathway.

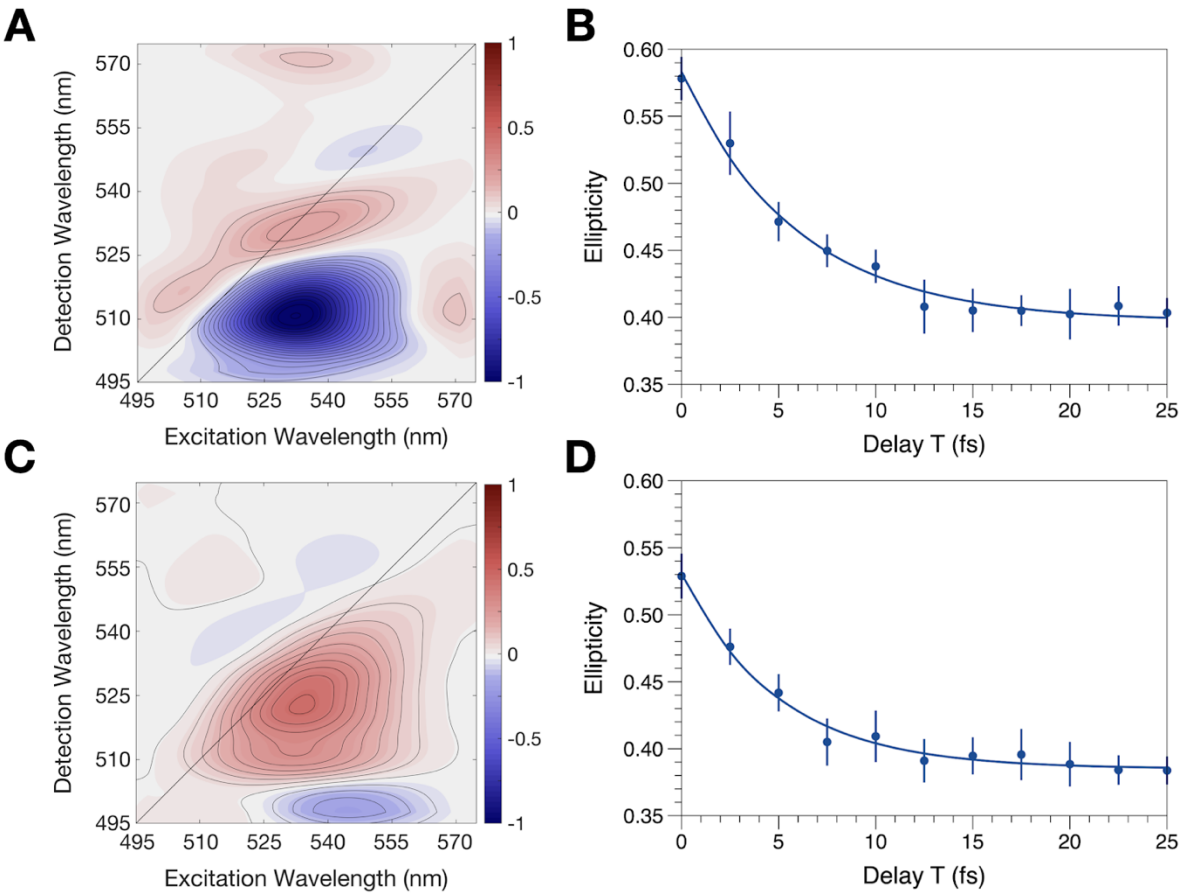

Figure 3.9. Electronic decoherence in wtPCP–Chl *a* and rPCP–Chl *b*. (a,c) Instantaneous EADS returned by a 2D global analysis of the 2DES spectrum for wtPCP–Chl *a* (Figure 3.2) and rPCP–Chl *b*. (b,d) Decay of the ellipticity of the diagonal GSB/SE signal in the 2DES spectra for wtPCP–Chl *a* (9.5 ± 2 fs time constant) and rPCP–Chl *b* (7.5 ± 1 fs time constant), as measured from antidiagonal half widths. The blue bars report the 95% confidence intervals for the ellipticities at each point.

The effective S_0–S_2 electronic decoherence time for the peridinin excitons can be estimated by measuring the decay of the ellipticity of the diagonal GSB/SE features in the 2DES spectra. The ellipticity compares the breadth of the homogeneously broadened spectral line shape along the antidiagonal with that of the inhomogeneously broadened line shape along the diagonal of the 2DES spectrum.[19,93] Here we used the below-diagonal (to shorter detection wavelengths) half-width for this measurement to avoid contributions as much as possible from fast excitation transfer, which contributes markedly to the evolution of the signal above the diagonal. The

decoherence time estimated from the ellipticity is 9.5 fs for wtPCP–Chl *a* and 7.5 fs for rPCP–Chl *b* (Figure 3.10bd). Just from an inspection of the instantaneous 2D-EADS spectra from the two complexes (Figure 3.9ac), however, one can tell that decoherence is significantly more rapid in rPCP–Chl *b* than in wtPCP–Chl *a* by comparing the deconvoluted antidiagonal widths. In previous work, we proposed that the faster decoherence in rPCP–Chl *b* arises from the increased system–medium coupling due to Chl *b*'s polar formyl substituent,[31] but additionally there may be contributions from the dynamics of the different peptide environments and aggregation states in the wtPCP–Chl *a* and rPCP–Chl *b* complexes. The ellipticity time constants determined in Figure 3.9 are somewhat shorter than those returned by the global model for the initial excitation transfer step from per2,3 to per1 (Table 3.2).

Also relevant to the ultrafast peridinin-to-Chl excitation energy transfer pathway in PCP are the decoherence times for pairs of exciton states, which might be expected to be longer than that for the S_0–S_2 energy gaps of the peridinins. The interexciton dephasing time constants can be measured from the damping of electronic quantum beating. The below-diagonal (540 nm, 510 nm) coordinate in the 2DES spectrum from wtPCP–Chl *a* would measure beating due to optical preparation of the $|\mathrm{per}\rangle\langle 1\mathrm{per2,3}|$ coherence, but the signal amplitude there is dominantly from population signals and is not strongly modulated (Figure 3.10a). However, a cross peak due to electronic quantum beating is clearly observed in the instantaneous 2D-EADS from wtPCP–Chl *a* (Figure 3.9a) and in the 2DES spectra at the earliest waiting times *T* (Figure 3.2) below the diagonal at (570 nm, 510 nm), which measures the $|\mathrm{Chl}\rangle\langle \mathrm{per2,3}|$ coherence. The amplitude transient at this coordinate exhibits a rapidly damped cosinusoidal oscillation in a region of the 2DES spectrum (Figures 3.2 and 3.10b) that is free of strong background from peridinin population signals. In contrast to the population transients at the Chl cross peaks discussed

above, which exhibit rising modulated profiles corresponding to the excitation energy transfer times (Figure 3.8), the quantum beating transient observed here is damped from a maximum at short waiting times *T*. The principal modulation component (Table 3.4) has a frequency of 1150 cm^{-1}, about half of the ~2060 cm^{-1} energy gap expected from the Chl exciton to the per2,3 excitons, but the waveform here would be expected to be aliased to a lower frequency by the 21-fs width of the instrument-response function. The 43-fs damping time observed at this coordinate is notably somewhat longer than the excitation transfer time constants along the pathway from per2,3 to the Chl acceptor (Table 3.2).

An additional possible contribution to the lower beating frequency detected at the |Chl⟩⟨per2,3| coherence is damping by coherence transfer[94–96] to the |Chl⟩⟨per1| coherence, which contributes an obvious cross peak at the (570 nm, 540 nm) coordinate in the 2DES spectrum (Figure 3.2) and in the instantaneous 2D-EADS (Figure 3.9a). The suggestion that the electronic coherence is transferred from |Chl⟩⟨per2,3| to |Chl⟩⟨per1| is made because the cross peak for the latter coherence is stronger in the instantaneous 2D-EADS despite being in a region of weak laser intensity. Figure 3.10c further shows that the amplitude transient at the (570 nm, 540 nm) coordinate also exhibits a rapidly damped quantum beating, with the modulation component at 885 cm^{-1} corresponding fairly well given the confidence interval to the expected 975 cm^{-1} energy gap between the Chl and per1 excitons. The damping time for the quantum beating here is the same as that at the |Chl⟩⟨per2,3| coherence (Table 3.4).

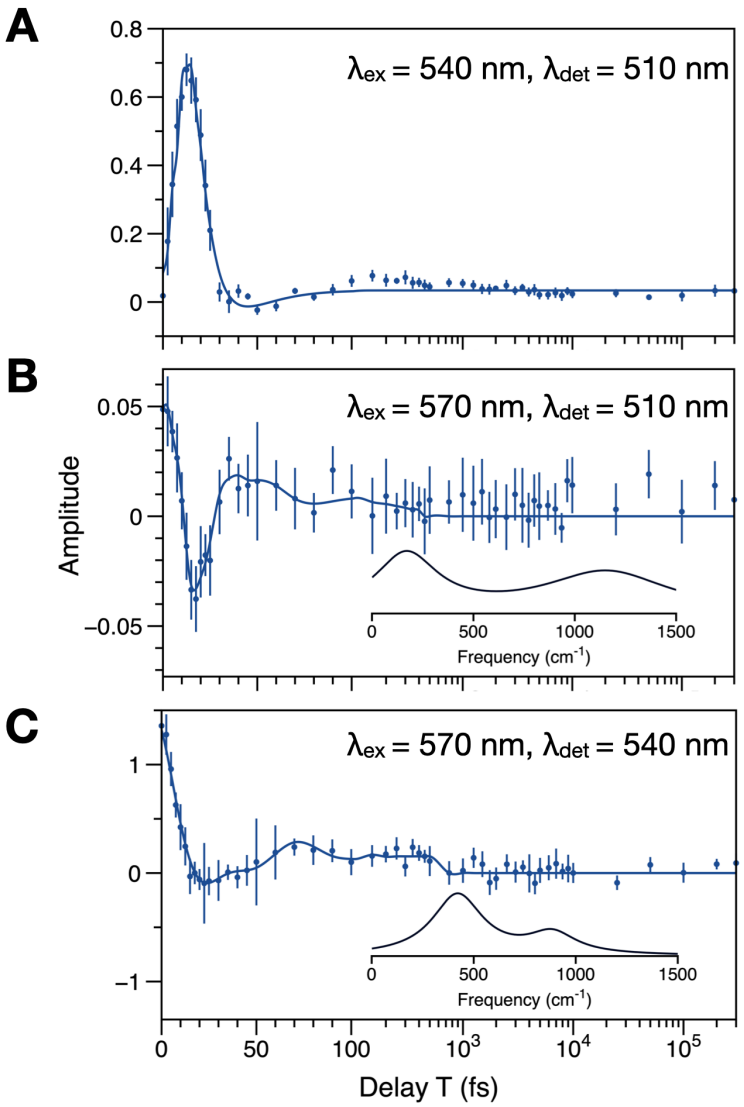

Figure 3.10. 2DES signal amplitude transients detected below the diagonal in the 2DES spectra from wtPCP–Chl *a* (Figure 3.2): (a) with optical excitation at 540 nm and detection at 510 nm; (b) with optical excitation at 570 nm and detection at 510 nm; (c) with optical excitation at 570 nm and detection at 540 nm. The semilogarithmic waiting time *T* axis is split at 100 fs. In (a), the data points are superimposed upon the amplitude of the population signal determined by the global model for per1 (panel a, from Figure 3.5). In (b,c), the data points are superimposed upon fitted models including two damped cosinusoids, with the parameters reported in Table 3.4. Each model is convoluted with the 21-fs instrument response function. The insets show the corresponding modulation spectrum in each case. The blue bars report the 95% confidence intervals for the amplitudes at each point.

Table 3.4. Model parameters for the modulation components detected in the quantum beating amplitude transients (Figure 3.10bc) with excitation of the Chl *a* exciton at 570 nm in the 2DES spectra from wtPCP–Chl *a* (Figure 3.2).

Detection (nm)	***A***	**ω (cm^{-1})**	**φ (rad)**	**τ (fs)**
510	0.141	176 ± 30	0.93	71 ± 8
	0.062	1150 ± 120	3.10	43 ± 3
540	0.283	420 ± 50	0.35	41 ± 6
	0.120	885 ± 160	0.20	38 ± 5

3.4 Discussion

Nonadiabatic mechanisms,[97–100] involving concerted vibrational and electronic motions, have been discussed in a number of previous studies of excitation energy transfer in photosynthetic light harvesting systems in the intermediate electronic coupling regime. The extent of delocalization over a chromophore cluster and the excitation energy transfer rate can be enhanced by vibronic resonance, the condition obtained when the vibrational quanta of the included chromophores match the gaps between the exciton energy levels. This principle was recognized early on in the work of Moran and coworkers[101,102] on the isostructural phycobiliproteins allophycocyanin and *C*-phycocyanin. The rate of excitation transfer to the lowest energy exciton in allophycocyanin was determined to be ten times faster than that in *C*-phycocyanin because environmental tuning of one of the site energies of the paired phycocyanobilin chromophores in the latter results in vibronic resonance with a HOOP promoting mode. Tiwari et al.[103,104] subsequently showed that vibronic resonance involving weakly coupled anticorrelated vibrations can promote excitation energy transfer when the

vibrations are delocalized over a pair of electronic chromophores. The excitation transfer mechanism in this situation is effectively an internal conversion between exciton potential surfaces arranged in a nested funnel. Scholes and coworkers[105,106] conclude, however, that the promoting vibrations in the complexes studied in prior work would serve as incoherent spectators with respect to the reaction coordinate for the excitation transfer process.

One of the novel findings of the present work, then, is that the ultrafast excitation transfer rates in PCP are observed to be relatively insensitive to the changes in the donor–acceptor energy gaps that accompany replacement of the Chl *a* acceptors with Chl *b*. The rates might have been expected to be considerably slowed in PCP when Chl *b* is present owing to a significant detuning from the energy level spacings for the natural, Chl *a*-containing complex, but the per1 to Chl step is slowed in rPCP–Chl *b* at most by a few fs (Table 3.2). The electronic dephasing rate was measured in the 2DES ellipticity measurements to be somewhat faster in rPCP–Chl *b*, as noted previously,[31] which would apply an additional disadvantage. These observations require us to go beyond an incoherent vibronic model to account for the excitation energy transfer dynamics in PCP complexes.

The vibrationally impulsive and phased amplitude modulations detected at the Chl cross peak in the wtPCP–Chl *a* and rPCP–Chl *b* complexes indicate that vibrational phase coherence is retained in the product Chl exciton following passage through a CI with the potential surface of the per1 exciton, as depicted in the cartoon shown in Figure 3.11. This finding is consistent with a vibronically coherent mechanism involving strongly coupled vibrations of the delocalized electronic chromophores as controlling the reaction coordinate. The dynamics in PCP are evidently analogous to that of an organic molecule undergoing vibronically coherent nonradiative transitions,[107–110] but to be clear the observations here in PCP are the signature of

strongly coupled and rapidly damped[111] wavepacket motions in an electronically excited product state. Similar observations of excited-state vibrational phase coherence involving strongly coupled vibrations[112] were reported for photoinduced CT reactions in a model reaction center composed of a carotenoid–porphyrin–fullerene triad[113] and in organic photovoltaic blends containing conjugated polymers and fullerenes.[114] Nonradiative decay to emitting states in DNA-templated silver nanoclusters may involve a comparable vibronic regime of nonadiabatic dynamics.[95]

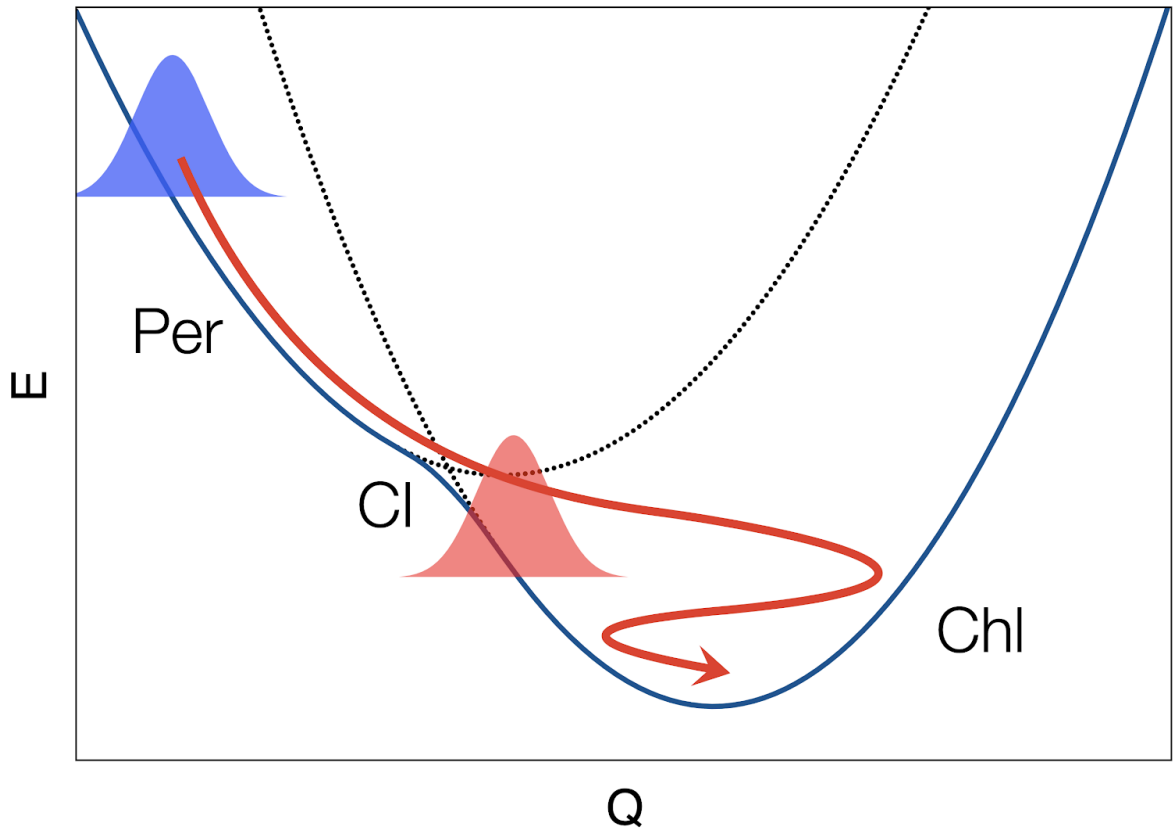

Figure 3.11. Cartoon representation of nonadiabatic passage of a vibronic wavepacket initially on peridinin exciton 1 (Per, blue wavepacket) through a conical intersection (CI) to reach the Chl *a* acceptor, where its motion is damped (red wavepacket), as plotted with respect to a generalized vibrational coordinate, Q.

The out-of-plane peridinin vibrations that we identified in the coherent wavepacket motions at the Chl acceptor are reasonable candidates for the branching (or tuning and coupling) modes that modulate the degeneracy between the donor and acceptor states over a seam of CIs, where nonadiabatic transitions are the most probable.[100,115–121] In a multistep pathway, such as that detected here for PCP, the CIs are likely to be linked together to form a cascade,[122–125] effectively forming a vibronic conduit between the optically excited and lowest energy emissive states in a manifold. The peridinin vibrational modes that promote passage from the peridinin to the Chl exciton potential energy surfaces exhibit relatively short damping times, not much longer than the excitation transfer time constants. Spectator vibrations, not strongly coupled to the reaction coordinate, would be expected to be more slowly damped.[126] The damping times of these modes are not affected by replacement of Chl *a* by Chl *b* in the PCP complexes, which indicates that the effect of vibrational resonance with the acceptor exciton is pretty small in this regime of dynamics. It is probably significant, however, that the Chl-specific modes detected in the vibronic coherence have significantly longer damping times than the peridinin modes given that the excitation transfer event eventually results in a localized Chl excited state.

The interactions between the peridinins and the Chl acceptors in PCP involve a combination of static and dynamic couplings of the vibrational modes to the exciton states, and the latter are likely to be the origin of the coherent nonadiabatic dynamics. Owing to its carbonyl substituent, peridinin has an ICT character that is revealed in Stark absorption spectroscopy measurements[47,127] that would contribute to a stronger mixing with the Chl electronic states. The ICT character is enhanced by static out-of-plane deformations of the isoprenoid backbone,[128] including those imposed on the peridinins by the binding sites in the chromophore cluster in PCP,[45] but the the torsional and pyramidal distortions that follow optical excitation to the S_2 state

would result in even larger enhancements.[29,58–60] This dynamic ICT character very likely determines the coherent dynamics we observed in PCP because steeper energy trajectories would be achieved near the CI seams towards the Chl acceptors as the out-of-plane modes are displaced. Much weaker vibronic interactions are observed in the incoherent regime, such as in LH2[52,129] or the FMO complex, where the dynamic couplings of the unsubstituted carotenoids and bacteriochlorophyll chromophores, respectively, are likely to be much less significant.

Of course, operation of the coherent vibronic regime in PCP would involve a delicate balance between coherent excitation transfer and dynamic exciton localization[16,29] because the dynamic coupling of the out-of-plane peridinin vibrations will eventually overwhelm the intermediate strength of electronic coupling between the chromophores. The temporal window that allows the ultrafast excitation energy transfer mechanism to operate in PCP is very short because the same out-of-plane vibrational motions of the peridinins that drive the excitation transfers to the Chl acceptors eventually result in localized excitations in a fraction of events. A related balance exists between ultrafast excitation transfer and trapping of excitation via charge-transfer reactions; small changes in the geometry of delocalized chromophore clusters due to conformational changes in the protein surroundings may be able to transform an efficient excitation transfer pathway into one that leads to a trapping site, for example in photoprotective nonphotochemical quenching mechanisms.[130]

An important implication of this study beyond natural photosynthesis is the possibility that smart light-harvesting structures or materials can be designed to operate with coherent control of the directionality and yield of excitation energy transfer. The key may be to employ chemical modifications that obtain relatively strong nonadiabatic couplings, especially using vibrational coordinates or dopants that vary the charge-transfer character.[131,132] Given knowledge

of the conditions that favor coherent nonadiabatic excitation energy transfers, unusually efficient excitation transfer processes might be obtained despite the competition with the ultrafast nonradiative processes that quench captured excitations and destroy the initial quantum coherence.

APPENDIX

A3.1 Residual Phase

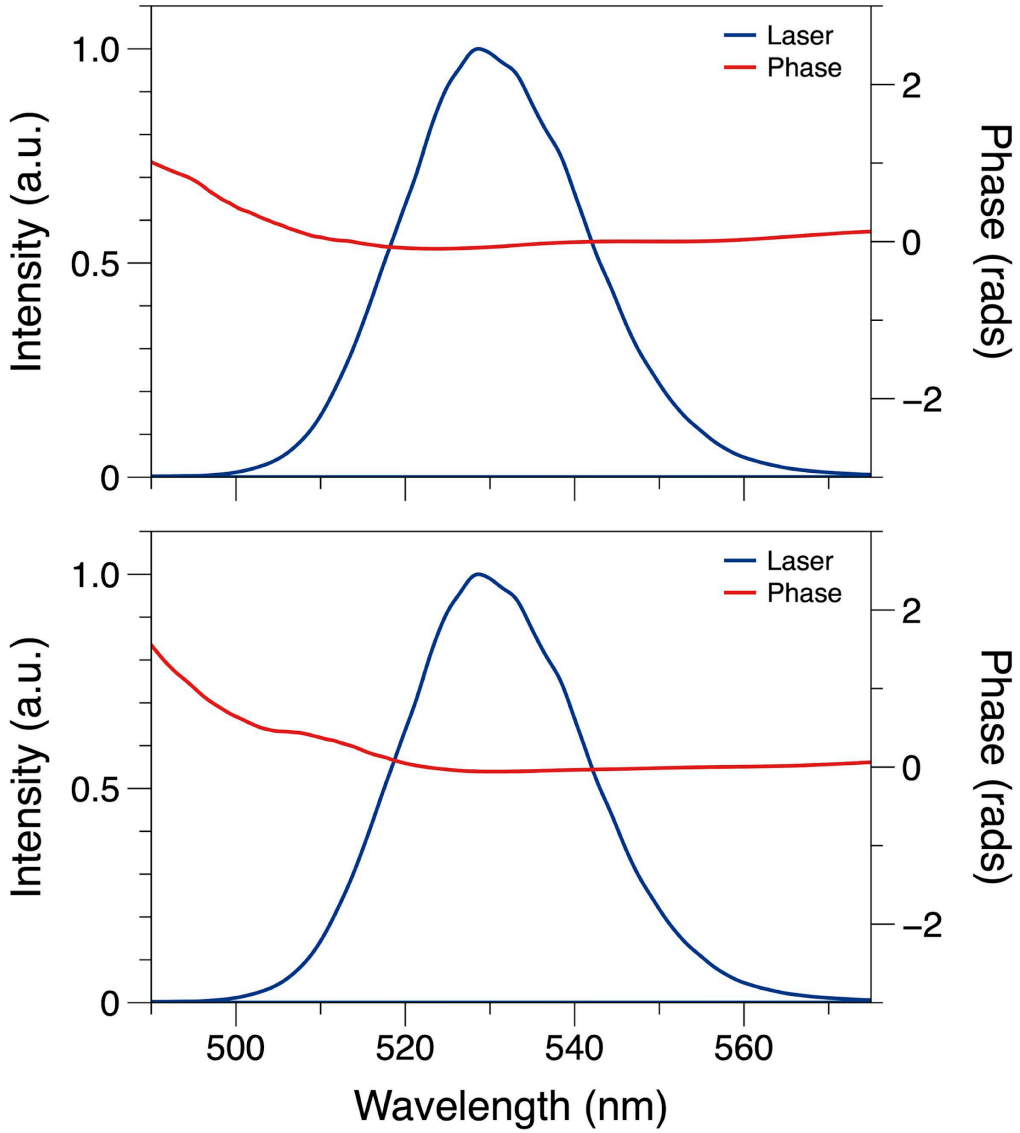

Figure A3.1. NOPA output spectra (blue) of pump (top) and probe (bottom) pulses. Superimposed are the optimized residual phases (red), as determined by MIIPS scans.

A3.2 Preliminary Analysis of Excitation Energy Transfer and Peridinin Nonradiative Decay Kinetics

Prior to carrying out the global target analysis discussed in the main chapter, a preliminary analysis of the amplitude kinetics at marked coordinates in the 2DES spectra from PCP complexes was conducted using sums-of-exponential models. The results from this analysis are shown in the following Figures A3.2–A3.4. The models were optimized using a nonlinear least-squares gradient optimizer coded in pascal for the Pro Fit (Quantum Software) package. The optimization was conducted with iterative reconvolution of the 21-fs instrument response function, as estimated from the 15 fs pulse durations determined by the MIIPS scans as detailed above and assuming Gaussian electric-field envelopes. The fit parameters for the multiexponential models include confidence intervals, which were obtained from fitting the average of the amplitudes from 9 2DES spectra. The amplitudes are plotted with error bars reporting the 95% confidence intervals (+/− one standard deviation from the average value).

Models: amplitudes $A_i < 0$ denote rising components, $A_i > 0$ denote falling components; A_0 are non-decaying.

$$A(t) = A_1\,\mathrm{e}^{-k_{2x}T} + A_2\,\mathrm{e}^{-(k_{xc}+k_{x1})T} + A_3\,\mathrm{e}^{-k_{10}T} + A_0$$

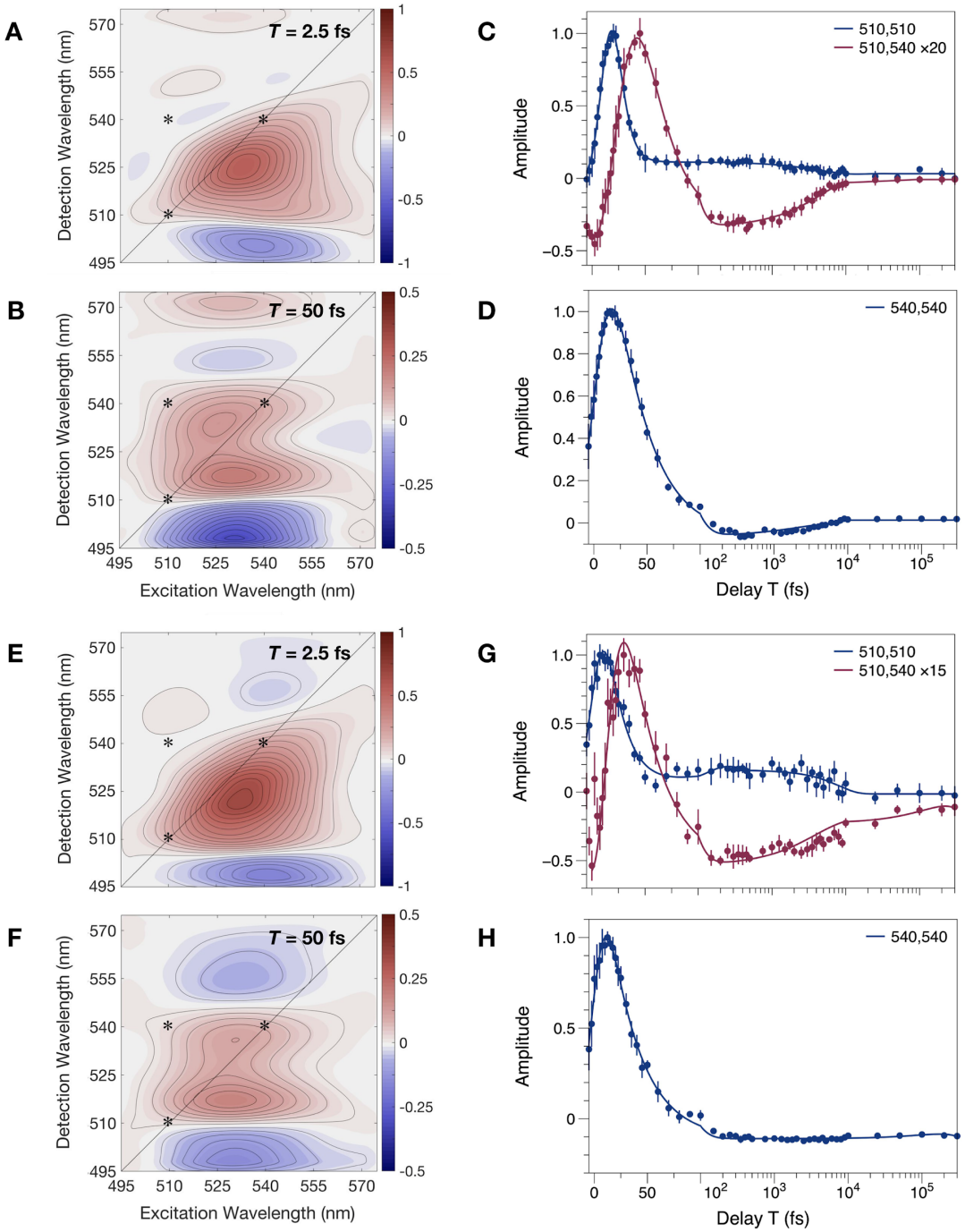

Figure A3.2. Time evolution of 2DES spectra in wtPCP–Chl *a* and rPCP–Chl *b* at room temperature (23 °C) and absolute amplitudes for diagonal and off-diagonal signals from peridinin excitons. (a,b) Phased absorptive 2DES spectra measured at room temperature (23 °C) at waiting times $T = 2.5$ and 50 fs in wtPCP–Chl *a*. The amplitudes are plotted with evenly spaced contour lines and tinted with a color bar ranging from red for positive signals (ground-state bleaching (GSB) and stimulated emission (SE)) to blue for negative signals (excited state absorption (ESA)). (c,d) Absolute amplitudes with 95% confidence intervals and fitted models for the signals at the marked coordinates in the 2DES spectra for wtPCP–Chl *a*. (e,f) Phased absorptive

2DES spectra at waiting times $T = 2.5$ and 50 fs in rPCP–Chl *b*. (g,h) Absolute amplitudes with 95% confidence intervals and fitted models for the signals at the marked coordinates in the 2DES spectra for rPCP–Chl *b*. As plotted, the amplitudes are normalized with respect to the intensity of the laser spectrum. Parameters for the multiexponential models are reported in Tables A3.2.

Table A3.2a. Model exponential decay parameters for the amplitude transient shown in Figure A3.2 for wtPCP–Chl *a* at (λ_{ex} = 510 nm, λ_{det} = 510 nm).

Amplitude	**Time constant (fs)**
1.9 ± 0.3	9 ± 1
0.12 ± 0.02	2981 ± 530

Table A3.2b. Model parameters for the amplitude transient shown in Figure A3.2 for wtPCP–Chl *a* at (λ_{ex} = 510 nm, λ_{det} = 540 nm).

Amplitude	**Time constant (fs)**
-0.95 ± 0.17	12 ± 1
0.27 ± 0.04	25 ± 2
-0.17 ± 0.08	1726 ± 403

Table A3.2c. Model parameters for the amplitude transient shown in Figure A3.2 for rPCP–Chl *b* at (λ_{ex} = 510 nm, λ_{det} = 510 nm).

Amplitude	**Time constant (fs)**
2.09 ± 0.11	11.5 ± 1
0.19 ± 0.01	3650 ± 952

Table A3.2d. Model exponential decay parameters for the amplitude transient shown in Figure A3.2 for rPCP–Chl *b* at (λ_{ex} = 510 nm, λ_{det} = 540 nm).

Amplitude	**Time constant (fs)**
-0.33 ± 0.07	12 ± 2
0.28 ± 0.01	27 ± 3
-0.13 ± 0.52	2804 ± 779
-0.04 ± 0.35	23085 ± 1681

Table A3.2e. Model parameters for the amplitude transient shown in Figure 3.2 for wtPCP–Chl *a* at (λ_{ex} = 540 nm, λ_{det} = 540 nm).

Amplitude	**Time constant**	**Assignment**
0.87 ± 0.14	30 ± 2 fs	$1/(k_{2x} + k_{2C})$
-0.17 ± 0.03	2681 ± 316 fs	S_x

Table A3.2f. Model parameters for the amplitude transient shown in Figure 3.2 for rPCP–Chl *b* at (λ_{ex} = 540 nm, λ_{det} = 540 nm).

Amplitude	**Time constant**	**Assignment**
0.83 ± 0.12	29 ± 4 fs	$1/(k_{2x} + k_{2C})$
-0.09 ± 0.04	non-decaying	S_x

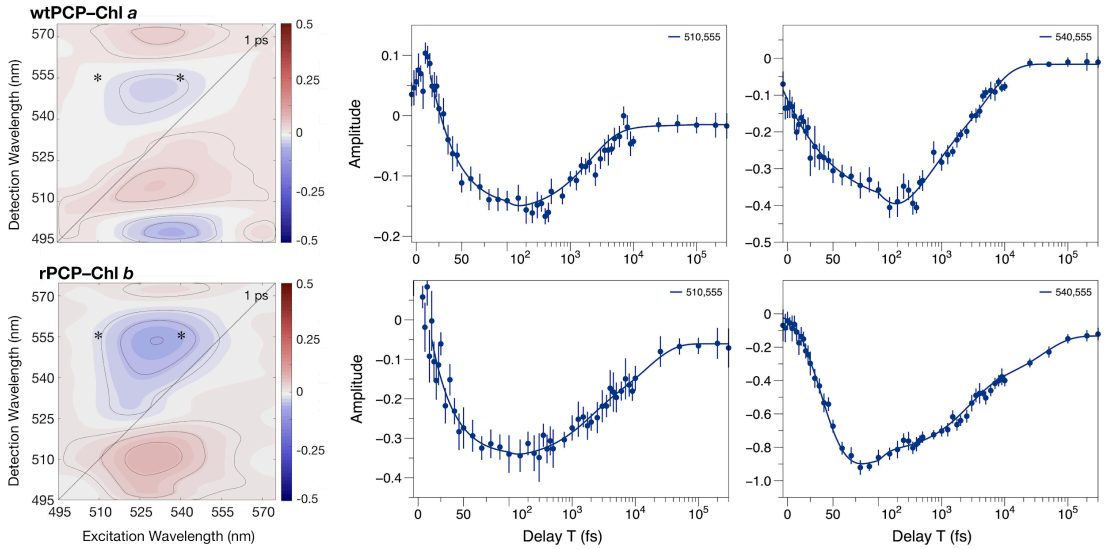

Figure A3.3. Kinetics of above-diagonal ESA signals in the 2DES spectra from (*top*) wtPCP–Chl *a* and (*bottom*) rPCP–Chl *b* with excitation at 510 nm and 540 nm. (*Left*) Phased absorptive 2DES spectra at waiting time $T = 1$ ps. (*Right*) Amplitudes for the marked coordinates ($\lambda_{ex} = 510$ nm, $\lambda_{det} = 555$ nm and $\lambda_{ex} = 540$ nm, $\lambda_{det} = 555$ nm), as plotted against a semilogarithmic axis split at $T = 100$ fs. Parameters for the multiexponential models are reported in Tables A3.3.

Table A3.3a. Model parameters for the amplitude transient shown in Figure A3.3 for wtPCP–Chl *a* at ($\lambda_{ex} = 510$ nm, $\lambda_{det} = 555$ nm).

Amplitude	**Time constant**
0.40 ± 0.10	38 ± 3 fs
-0.26 ± 0.15	1.8 ± 0.2 ps
-0.07 ± 0.04	18.1 ± 1 ps
-0.01 ± 0.01	non-decaying

Table A3.3b. Model parameters for the amplitude transient shown in Figure A3.3 for wtPCP–Chl *a* at (λ_{ex} = 540 nm, λ_{det} = 555 nm).

Amplitude	**Time constant**
0.74 ± 0.11	44 ± 2 fs
-0.41 ± 0.30	1.9 ± 0.3 ps
-0.22 ± 0.16	18.0 ± 1 ps
-0.01 ± 0.03	non-decaying

Table A3.3c. Model parameters for the amplitude transient shown in Figure A3.3 for rPCP–Chl *b* at (λ_{ex} = 510 nm, λ_{det} = 555 nm).

Amplitude	**Time constant**
0.92 ± 0.10	32 ± 4 fs
-0.49 ± 0.08	2.5 ± 0.8 ps
-0.10 ± 0.05	18.7 ± 0.5 ps
-0.06 ± 0.02	non-decaying

Table A3.3d. Model parameters for the amplitude transient shown in Figure A3.3 for rPCP–Chl *b* at (λ_{ex} = 540 nm, λ_{det} = 555 nm).

Amplitude	**Time constant**
1.40 ± 0.20	37 ± 1 fs
-0.68 ± 0.19	2.3 ± 0.3 ps
-0.23 ± 0.04	23.1 ± 2.0 ps
-0.13 ± 0.17	non-decaying

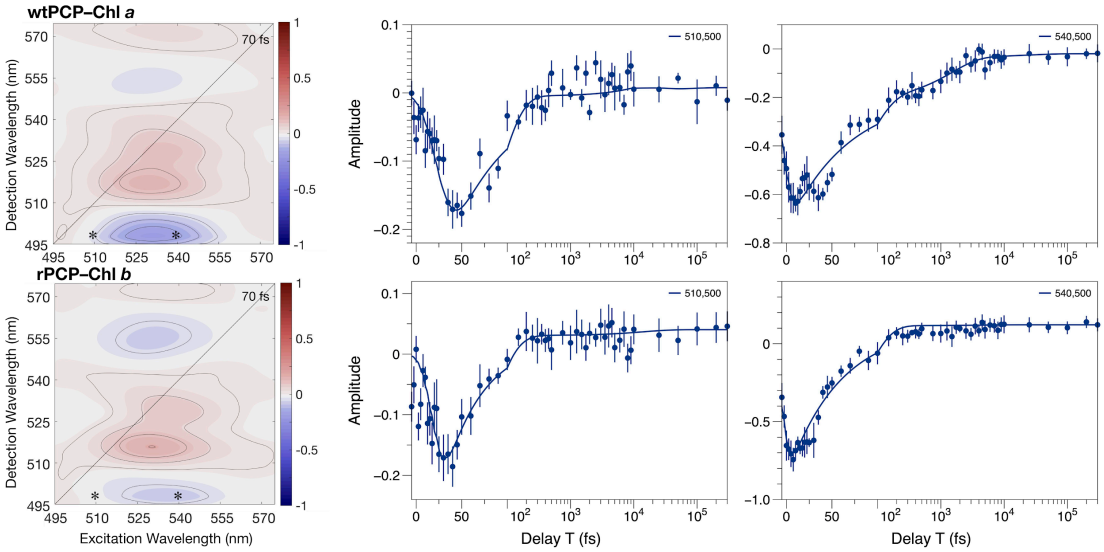

Figure A3.4. Kinetics of the below-diagonal ESA signals in the 2DES spectra from (*top*) wtPCP–Chl *a* and (*bottom*) rPCP–Chl *b* with excitation at 510 nm and 540 nm. (*Left*) Phased absorptive 2DES spectra at waiting time T = 70 fs. (*Right*) Amplitudes for the marked coordinates (λ_{ex} = 510 nm, λ_{det} = 500 nm and λ_{ex} = 540 nm, λ_{det} = 500 nm), as plotted against a semilogarithmic axis split at T = 100 fs. Parameters for the multiexponential models are reported in Tables A3.4.

Table A3.4a. Model exponential decay parameters for the amplitude transient shown in Figure A3.4 for wtPCP–Chl *a* at (λ_{ex} = 510 nm, λ_{det} = 500 nm).

Amplitude	**Time constant**
0.62 ± 0.22	14 ± 5 fs
-0.49 ± 0.18	61 ± 27 fs
-0.13 ± 0.07	25.7 ± 6.1 ps

Table A3.4b. Model exponential decay parameters for the amplitude transient shown in Figure A3.4 for wtPCP–Chl *a* at (λ_{ex} = 540 nm, λ_{det} = 500 nm).

Amplitude	**Time constant**
-1.22 ± 0.37	64 ± 3 fs
-0.58 ± 0.25	1.5 ± 0.4 ps

Table A3.4c. Model exponential decay parameters for the amplitude transient shown in Figure A3.4 for rPCP–Chl *b* at (λ_{ex} = 510 nm, λ_{det} = 500 nm).

Amplitude	**Time constant**
0.77 ± 0.21	13 ± 3 fs
-0.62 ± 0.44	59 ± 9 fs
-0.05 ± 0.38	non-decaying

Table A3.4d. Model exponential decay parameters for the amplitude transient shown in Figure A3.4 for rPCP–Chl *b* at (λ_{ex} = 540 nm, λ_{det} = 500 nm).

Amplitude	**Time constant**
-1.40 ± 0.20	58 ± 6 fs
0.19 ± 0.04	non-decaying

REFERENCES

REFERENCES

(1) Pullerits, T.; Chachisvilis, M.; Jones, M. R.; Hunter, C. N.; Sundström, V. Exciton Dynamics in the Light-Harvesting Complexes of *Rhodobacter Sphaeroides*. *Chem. Phys. Lett.* **1994**, *224* (3), 355–365.

(2) Bradforth, S. E.; Jimenez, R.; van Mourik, F.; van Grondelle, R.; Fleming, G. R. Excitation Transfer in the Core Light-Harvesting Complex (LH-1) of *Rhodobacter Sphaeroides*: An Ultrafast Fluorescence Depolarization and Annihilation Study. *J. Phys. Chem.* **1995**, *99* (43), 16179–16191.

(3) Edington, M. D.; Riter, R. E.; Beck, W. F. Evidence for Coherent Energy Transfer in Allophycocyanin Trimers. *J. Phys. Chem.* **1995**, *99* (43), 15699–15704.

(4) Pullerits, T.; Chachisvilis, M.; Sundström, V. Exciton Delocalization Length in the B850 Antenna of Rhodobacter Sphaeroides. *J. Phys. Chem.* **1996**, *100* (25), 10787–10792.

(5) Savikhin, S.; Buck, D. R.; Struve, W. S. Oscillating Anisotropies in a Bacteriochlorophyll Protein: Evidence for Quantum Beating between Exciton Levels. *Chem. Phys.* **1997**, *223* (2), 303–312.

(6) Engel, G. S.; Calhoun, T. R.; Read, E. L.; Ahn, T. K.; Mančal, T.; Cheng, Y. C.; Blankenship, R. E.; Fleming, G. R. Evidence for Wavelike Energy Transfer through Quantum Coherence in Photosynthetic Systems. *Nature* **2007**, *446*, 782–786.

(7) Collini, E.; Wong, C. Y.; Wilk, K. E.; Curmi, P. M. G.; Brumer, P.; Scholes, G. D. Coherently Wired Light-Harvesting in Photosynthetic Marine Algae at Ambient Temperature. *Nature* **2010**, *463* (7281), 644–647.

(8) Dahlbom, M.; Beenken, W.; Sundström, V.; Pullerits, T. Collective Excitation Dynamics and Polaron Formation in Molecular Aggregates. *Chem. Phys. Lett.* **2002**, *364* (5), 556–561.

(9) Ishizaki, A.; Fleming, G. R. Quantum Coherence in Photosynthetic Light Harvesting. *Annu. Rev. Condens. Matter Phys.* **2012**, *3* (1), 333–361.

(10) Mirkovic, T.; Ostroumov, E. E.; Anna, J. M.; van Grondelle, R.; Govindjee; Scholes, G. D. Light Absorption and Energy Transfer in the Antenna Complexes of Photosynthetic Organisms. *Chem. Rev.* **2017**, *117* (2), 249–293.

(11) Chenu, A.; Scholes, G. D. Coherence in Energy Transfer and Photosynthesis. *Annu. Rev. Phys. Chem.* **2015**, *66*, 69–96.

(12) Zinth, W.; Wachtveitl, J. The First Picoseconds in Bacterial Photosynthesis—Ultrafast Electron Transfer for the Efficient Conversion of Light Energy. *Chemphyschem* **2005**, *6* (5), 871–880.

(13) Niedringhaus, A.; Policht, V. R.; Sechrist, R.; Konar, A.; Laible, P. D.; Bocian, D. F.; Holten, D.; Kirmaier, C.; Ogilvie, J. P. Primary Processes in the Bacterial Reaction Center Probed by Two-Dimensional Electronic Spectroscopy. *Proc. Natl. Acad. Sci. U. S. A.* **2018**, *115* (14), 3563–3568.

(14) Jumper, C. C.; Anna, J. M.; Stradomska, A.; Schins, J.; Myahkostupov, M.; Prusakova, V.; Oblinsky, D. G.; Castellano, F. N.; Knoester, J.; Scholes, G. D. Intramolecular Radiationless Transitions Dominate Exciton Relaxation Dynamics. *Chem. Phys. Lett.* **2014**, *599*, 23–33.

(15) Proppe, A. H.; Li, Y. C.; Aspuru-Guzik, A.; Berlinguette, C. P.; Chang, C. J.; Cogdell, R.; Doyle, A. G.; Flick, J.; Gabor, N. M.; van Grondelle, R.; Hammes-Schiffer, S.; Jaffer, S. A.; Kelley, S. O.; Leclerc, M.; Leo, K.; Mallouk, T. E.; Narang, P.; Schlau-Cohen, G. S.; Scholes, G. D.; Vojvodic, A.; Yam, V. W.-W.; Yang, J. Y.; Sargent, E. H. Bioinspiration in Light Harvesting and Catalysis. *Nature Rev. Materials* **2020**, *5* (11), 828–846.

(16) Ishizaki, A.; Calhoun, T. R.; Schlau-Cohen, G. S.; Fleming, G. R. Quantum Coherence and Its Interplay with Protein Environments in Photosynthetic Electronic Energy Transfer. *Phys. Chem. Chem. Phys.* **2010**, *12* (27), 7319–7337.

(17) Thyrhaug, E.; Tempelaar, R.; Alcocer, M. J. P.; Žídek, K.; Bína, D.; Knoester, J.; Jansen, T. L. C.; Zigmantas, D. Identification and Characterization of Diverse Coherences in the Fenna-Matthews-Olson Complex. *Nat. Chem.* **2018**, *10* (7), 780–786.

(18) Halpin, A.; Johnson, P. J.; Tempelaar, R.; Murphy, R. S.; Knoester, J.; Jansen, T. L.; Miller, R. J. Two-Dimensional Spectroscopy of a Molecular Dimer Unveils the Effects of Vibronic Coupling on Exciton Coherences. *Nat. Chem.* **2014**, *6* (3), 196–201.

(19) Duan, H.-G.; Prokhorenko, V. I.; Cogdell, R. J.; Ashraf, K.; Stevens, A. L.; Thorwart, M.; Miller, R. J. D. Nature Does Not Rely on Long-Lived Electronic Quantum Coherence for Photosynthetic Energy Transfer. *Proc. Natl. Acad. Sci. U. S. A.* **2017**, *114* (32), 8493–8498.

(20) Beljonne, D.; Curutchet, C.; Scholes, G. D.; Silbey, R. J. Beyond Förster Resonance Energy Transfer in Biological and Nanoscale Systems. *J. Phys. Chem. B* **2009**, *113*, 6583.

(21) Jonas, D. M. Two-Dimensional Femtosecond Spectroscopy. *Annu. Rev. Phys. Chem.* **2003**, *54*, 425–463.

(22) Mimuro, M.; Tamai, N.; Ishimaru, T.; Yamazaki, I. Characteristic Fluorescence Components in Photosynthetic Pigment System of a Marine Dinoflagellate, Protogonyaulax Tamarensis, and Excitation Energy Flow among Them. Studies by Means of Steady-State and Time-Resolved Fluorescence Spectroscopy. *Biochimica et Biophysica Acta (BBA)-Bioenergetics* **1990**, *1016* (2), 280–287.

(23) Hofmann, E.; Wrench, P. M.; Sharples, F. P.; Hiller, R. G.; Welte, W.; Diederichs, K. Structural Basis of Light Harvesting by Carotenoids: Peridinin-Chlorophyll-Protein from *Amphidinium Carterae*. *Science* **1996**, *272* (5269), 1788–1791.

(24) Carbonera, D.; Giacometti, G.; Segre, U.; Hofmann, E.; Hiller, R. G. Structure-Based Calculations of the Optical Spectra of the Light-Harvesting Peridinin–chlorophyll–protein Complexes from *Amphidinium Carterae* and *Heterocapsa Pygmaea*. *J. Phys. Chem. B* **1999**, *103*, 6349–6356.

(25) Damjanović, A.; Ritz, T.; Schulten, K. Excitation Transfer in the Peridinin-Chlorophyll-Protein of *Amphidinium Carterae*. *Biophys. J.* **2000**, *79* (4), 1695–1705.

(26) Andreussi, O.; Knecht, S.; Marian, C. M.; Kongsted, J.; Mennucci, B. Carotenoids and Light-Harvesting: From DFT/MRCI to the Tamm–Dancoff Approximation. *J. Chem. Theory Comput.* **2015**, *11* (2), 655–666.

(27) Guberman-Pfeffer, M. J.; Greco, J. A.; Birge, R. R.; Frank, H. A.; Gascón, J. A. Light Harvesting by Equally Contributing Mechanisms in a Photosynthetic Antenna Protein. *J. Phys. Chem. Lett.* **2018**, *9* (3), 563–568.

(28) Guberman-Pfeffer, M. J.; Gascón, J. A. Carotenoid-Chlorophyll Interactions in a Photosynthetic Antenna Protein: A Supramolecular QM/MM Approach. *Molecules* **2018**, *23* (10), 1420–3049.

(29) Ghosh, S.; Bishop, M. M.; Roscioli, J. D.; LaFountain, A. M.; Frank, H. A.; Beck, W. F. Excitation Energy Transfer by Coherent and Incoherent Mechanisms in the Peridinin–chlorophyll *a* Protein. *J. Phys. Chem. Lett.* **2017**, *8*, 463–469.

(30) Roscioli, J. D.; Ghosh, S.; LaFountain, A. M.; Frank, H. A.; Beck, W. F. Quantum Coherent Excitation Energy Transfer by Carotenoids in Photosynthetic Light Harvesting. *J. Phys. Chem. Lett.* **2017**, *8* (20), 5141–5147.

(31) Roscioli, J. D.; Ghosh, S.; LaFountain, A. M.; Frank, H. A.; Beck, W. F. Structural Tuning of Quantum Decoherence and Coherent Energy Transfer in Photosynthetic Light Harvesting. *J. Phys. Chem. Lett.* **2018**, 5071–5077.

(32) Meneghin, E.; Volpato, A.; Cupellini, L.; Bolzonello, L.; Jurinovich, S.; Mascoli, V.; Carbonera, D.; Mennucci, B.; Collini, E. Coherence in Carotenoid-to-Chlorophyll Energy Transfer. *Nat. Commun.* **2018**, *9* (1), 3160.

(33) Bautista, J. A.; Hiller, R. G.; Sharples, F. P.; Gosztola, D.; Wasielewski, M.; Frank, H. A. Singlet and Triplet Energy Transfer in the Peridinin−Chlorophyll *a*−Protein from *Amphidinium Carterae*. *J. Phys. Chem. A* **1999**, *103* (14), 2267–2273.

(34) Kleima, F. J.; Hofmann, E.; Gobets, B.; van Stokkum, I. H.; van Grondelle, R.; Diederichs, K.; van Amerongen, H. Förster Excitation Energy Transfer in Peridinin-Chlorophyll-*a*-Protein. *Biophys. J.* **2000**, *78* (1), 344–353.

(35) Krueger, B. P.; Lampoura, S. S.; van Stokkum, I. H.; Papagiannakis, E.; Salverda, J. M.; Gradinaru, C. C.; Rutkauskas, D.; Hiller, R. G.; van Grondelle, R. Energy Transfer in the Peridinin Chlorophyll-*a* Protein of *Amphidinium Carterae* studied by Polarized Transient Absorption and Target Analysis. *Biophys. J.* **2001**, *80* (6), 2843–2855.

(36) Lampoura, S. S.; Krueger, B. P.; van Stokkum, I. H. M.; Salverda, J. M.; Gradinaru, C. C.; Rutkauskas, D.; Hiller, R. G.; van Grondelle, R. Energy Transfer in the Peridinin Chlorophyll *a* Protein of *Amphidinium Carterae* Studied by Polarized Absorption Measurements. *Int. J. Mod. Phys. B* **2001**, *15*, 3849–3852.

(37) Zigmantas, D.; Hiller, R. G.; Sundstrom, V.; Polivka, T. Carotenoid to Chlorophyll Energy Transfer in the Peridinin-Chlorophyll-*a*-Protein Complex Involves an Intramolecular Charge Transfer State. *Proc. Natl. Acad. Sci. U. S. A.* **2002**, *99* (26), 16760–16765.

(38) van Stokkum, I. H. M.; Papagiannakis, E.; Vengris, M.; Salverda, J. M.; Polívka, T.; Zigmantas, D.; Larsen, D. S.; Lampoura, S. S.; Hiller, R. G.; van Grondelle, R. Inter-Pigment Interactions in the Peridinin Chlorophyll Protein Studied by Global and Target Analysis of Time Resolved Absorption Spectra. *Chem. Phys.* **2009**, *357*, 70–78.

(39) Toa, Z. S. D.; deGolian, M. H.; Jumper, C. C.; Hiller, R. G.; Scholes, G. D. Consistent Model of Ultrafast Energy Transfer in Peridinin Chlorophyll-a Protein Using Two-Dimensional Electronic Spectroscopy and Förster Theory. *J. Phys. Chem. B* **2019**, *123* (30), 6410–6420.

(40) Polívka, T.; van Stokkum, I. H. M.; Zigmantas, D.; van Grondelle, R.; Sundström, V.; Hiller, R. G. Energy Transfer in the Major Intrinsic Light-Harvesting Complex from *Amphidinium Carterae*. *Biochemistry* **2006**, *45* (28), 8516–8526.

(41) Polívka, T.; Hiller, R. G.; Frank, H. A. Spectroscopy of the Peridinin–chlorophyll *a* Protein: Insight into Light-Harvesting Strategy of Marine Algae. *Arch. Biochem. Biophys.* **2007**, *458*, 111–120.

(42) Bautista, J. A.; Connors, R. E.; Raju, B. B.; Hiller, R. G.; Sharples, F. P.; Gosztola, D.; Wasielewski, M. R.; Frank, H. A. Excited State Properties of Peridinin: Observation of a Solvent Dependence of the Lowest Excited Singlet State Lifetime and Spectral Behavior Unique among Carotenoids. *J. Phys. Chem. B* **1999**, *103* (41), 8751–8758.

(43) Zigmantas, D.; Polívka, T.; Hiller, R. G.; Yartsev, A.; Sundström, V. Spectroscopic and Dynamic Properties of the Peridinin Lowest Singlet Excited States. *J. Phys. Chem. A* **2001**, *105* (45), 10296–10306.

(44) Zigmantas, D.; Hiller, R. G.; Yartsev, A.; Sundström, V.; Polívka, T. Dynamics of Excited States of the Carotenoid Peridinin in Polar Solvents: Dependence on Excitation Wavelength, Viscosity, and Temperature. *J. Phys. Chem. B* **2003**, *107* (22), 5339–5348.

(45) Shima, S.; Ilagan, R. P.; Gillespie, N.; Sommer, B. J.; Hiller, R. G.; Sharples, F. P.; Frank, H. A.; Birge, R. R. Two-Photon and Fluorescence Spectroscopy and the Effect of Environment on the Photochemical Properties of Peridinin in Solution and in the Peridinin-Chlorophyll-Protein from *Amphidinium Carterae*. *J. Phys. Chem. A* **2003**, *107* (40), 8052–8066.

(46) Chatterjee, N.; Niedzwiedski, D. M.; Kajikawa, T.; Hasegawa, S.; Katsumura, S.; Frank, H. A. Effect of π-Electron Conjugation Length on the Solvent-Dependent S_1 Lifetime of Peridinin. *Chem. Phys. Lett.* **2008**, *463*, 219–224.

(47) Kusumoto, T.; Horibe, T.; Kajikawa, T.; Hasegawa, S.; Iwashita, T.; Cogdell, R. J.; Birge, R. R.; Frank, H. A.; Katsumura, S.; Hashimoto, H. Stark Absorption Spectroscopy of Peridinin and Allene-Modified Analogues. *Chem. Phys.* **2010**, *373* (1), 71–79.

(48) Fuciman, M.; Enriquez, M. M.; Kaligotla, S.; Niedzwiedzki, D. M.; Kajikawa, T.; Aoki, K.; Katsumura, S.; Frank, H. A. Singlet and Triplet State Spectra and Dynamics of Structurally Modified Peridinins. *J. Phys. Chem. B* **2011**, *115*, 4436–4445.

(49) Enriquez, M. M.; Hananoki, S.; Hasegawa, S.; Kajikawa, T.; Katsumura, S.; Wagner, N. L.; Birge, R. R.; Frank, H. A. Effect of Molecular Symmetry on the Spectra and Dynamics of the Intramolecular Charge Transfer (ICT) State of Peridinin. *J. Phys. Chem. B* **2012**, *116* (35), 10748–10756.

(50) Wagner, N. L.; Greco, J. A.; Enriquez, M. M.; Frank, H. A.; Birge, R. R. The Nature of the Intramolecular Charge Transfer State in Peridinin. *Biophys. J.* **2013**, *104*, 1314–1325.

(51) Greco, J. A.; Wagner, N. L.; Frank, H. A.; Birge, R. R. The Forbidden $1^1B_u^-$ Excited Singlet State in Peridinin and Peridinin Analogues. *J. Phys. Chem. A* **2018**, *122* (1), 130–139.

(52) Ostroumov, E. E.; Mulvaney, R. M.; Cogdell, R. J.; Scholes, G. D. Broadband 2D Electronic Spectroscopy Reveals a Carotenoid Dark State in Purple Bacteria. *Science* **2013**, *340* (6128), 52–56.

(53) Beck, W. F.; Bishop, M. M.; Roscioli, J. D.; Ghosh, S.; Frank, H. A. Excited State Conformational Dynamics in Carotenoids: Dark Intermediates and Excitation Energy Transfer. *Arch. Biochem. Biophys.* **2015**, *572*, 175–183.

(54) Cerullo, G.; Polli, D.; Lanzani, G.; De Silvestri, S.; Hashimoto, H.; Cogdell, R. J. Photosynthetic Light Harvesting by Carotenoids: Detection of an Intermediate Excited State. *Science* **2002**, *298* (5602), 2395–2398.

(55) Polívka, T.; Sundström, V. Dark Excited States of Carotenoids: Consensus and Controversy. *Chem. Phys. Lett.* **2009**, *477*, 1–11.

(56) Tavan, P.; Schulten, K. Electronic Excitations in Finite and Infinite Polyenes. *Phys. Rev. B Condens. Matter* **1987**, *36* (8), 4337–4358.

(57) Ghosh, S.; Bishop, M. M.; Roscioli, J. D.; Mueller, J. J.; Shepherd, N. C.; LaFountain, A. M.; Frank, H. A.; Beck, W. F. Femtosecond Heterodyne Transient-Grating Studies of Nonradiative Decay of the S_2 ($1^1B_u^+$) State of β-Carotene: Contributions from Dark Intermediates and Double-Quantum Coherences. *J. Phys. Chem. B* **2015**, *119* (47), 14905–14924.

(58) Ghosh, S.; Bishop, M. M.; Roscioli, J. D.; LaFountain, A. M.; Frank, H. A.; Beck, W. F. Femtosecond Heterodyne Transient Grating Studies of Nonradiative Deactivation of the S_2 ($1^1B_u^+$) State of Peridinin: Detection and Spectroscopic Assignment of an Intermediate in the Decay Pathway. *J. Phys. Chem. B* **2016**, *120*, 3601–3614.

(59) Gurchiek, J. K.; Rose, J. B.; Guberman-Pfeffer, M. J.; Tilluck, R. W.; Ghosh, S.; Gascón, J. A.; Beck, W. F. Fluorescence Anisotropy Detection of Barrier Crossing and Ultrafast Conformational Dynamics in the S_2 State of β-Carotene. *J. Phys. Chem. B* **2020**, *124* (41), 9029–9046.

(60) Ghosh, S.; Roscioli, J. D.; Bishop, M. M.; Gurchiek, J. K.; LaFountain, A. M.; Frank, H. A.; Beck, W. F. Torsional Dynamics and Intramolecular Charge Transfer in the S_2 ($1^1B_u^+$) Excited State of Peridinin: A Mechanism for Enhanced Mid-Visible Light Harvesting. *J. Phys. Chem. Lett.* **2016**, *7* (18), 3621–3626.

(61) Miller, D. J.; Catmull, J.; Puskeiler, R.; Tweedale, H.; Sharples, F. P.; Hiller, R. G. Reconstitution of the Peridinin-Chlorophyll *a* Protein (PCP): Evidence for Functional Flexibility in Chlorophyll Binding. *Photosynth. Res.* **2005**, *86* (1-2), 229–240.

(62) Polívka, T.; Pascher, T.; Sundström, V.; Hiller, R. G. Tuning Energy Transfer in the Peridinin-Chlorophyll Complex by Reconstitution with Different Chlorophylls. *Photosynth. Res.* **2005**, *86* (1-2), 217–227.

(63) Schulte, T.; Hiller, R. G.; Hofmann, E. X-Ray Structures of the Peridinin-Chlorophyll-Protein Reconstituted with Different Chlorophylls. *FEBS Lett.* **2010**, *584* (5), 973–978.

(64) Ilagan, R. P.; Shima, S.; Melkozernov, A.; Lin, S.; Blankenship, R. E.; Sharples, F. P.; Hiller, R. G.; Birge, R. R.; Frank, H. A. Spectroscopic Properties of the Main-Form and High-Salt Peridinin-Chlorophyll a Proteins from *Amphidinium Carterae*. *Biochemistry* **2004**, *43* (6), 1478–1487.

(65) Schulte, T.; Niedwiedzki, D. M.; Birge, R. R.; Hiller, R. G.; Polívka, T.; Hofmann, E.; Frank, H. A. Identification of a Single Peridinin Sensing Chl-*a* Excitation in Reconstituted PCP by Crystallography and Spectroscopy. *Proc. Natl. Acad. U.S.A.* **2009**, *106*, 20474–20769.

(66) Kobayashi, M.; Akiyama, M.; Kano, H.; Kise, H. Spectroscopy and Structure Determination. In *Chlorophylls and Bacteriochlorophylls: Biochemistry, Biophysics, Functions and Applications*; Grimm, B., Porra, R. J., Rüdiger, W., Scheer, H., Eds.; Springer: Dordrecht, 2006; pp 79–94.

(67) Reimers, J. R.; Cai, Z. L.; Kobayashi, R.; Ratsep, M.; Freiberg, A.; Krausz, E. Assignment of the Q-Bands of the Chlorophylls: Coherence Loss via Q_x - Q_y Mixing. *Sci. Rep.* **2013**, *3*, 2761.

(68) Carbonera, D.; Di Valentin, M.; Spezia, R.; Mezzetti, A. The Unique Photophysical Properties of the Peridinin-Chlorophyll-*a*-Protein. *Curr. Protein Pept. Sci.* **2014**, *15* (4), 332–350.

(69) Sharples, F. P.; Wrench, P. M.; Ou, K.; Hiller, R. G. Two Distinct Forms of the Peridinin-Chlorophyll *a*-Protein from *Amphidinium Carterae*. *Biochem. Biophys. Acta* **1996**, *1276*, 117–123.

(70) Miller, D. J.; Catmull, J.; Puskeiler, R.; Tweedale, H.; Sharples, F. P.; Hiller, R. G. Reconstitution of the Peridinin-Chlorophyll *a* Protein (PCP): Evidence for Functional Flexibility in Chlorophyll Binding. *Photosynth. Res.* **2005**, *86* (1-2), 229–240.

(71) Shim, S. H.; Zanni, M. T. How to Turn Your Pump-Probe Instrument into a Multidimensional Spectrometer: 2D IR and Vis Spectroscopies via Pulse Shaping. *Phys. Chem. Chem. Phys.* **2009**, *11* (5), 748–761.

(72) Lozovoy, V. V.; Pastirk, I.; Dantus, M. Multiphoton Intrapulse Interference 4: Characterization and Compensation of the Spectral Phase of Ultrashort Laser Pulses. *Opt. Lett.* **2004**, *29*, 775–777.

(73) Augulis, R.; Zigmantas, D. Two-Dimensional Electronic Spectroscopy with Double Modulation Lock-in Detection: Enhancement of Sensitivity and Noise Resistance. *Opt. Express* **2011**, *19* (14), 13126–13133.

(74) Roscioli, J. D.; Ghosh, S.; LaFountain, A. M.; Frank, H. A.; Beck, W. F. Structural Tuning of Quantum Decoherence and Coherent Energy Transfer in Photosynthetic Light Harvesting. *J. Phys. Chem. Lett.* **2018**, *9*, 5071–5077.

(75) Weiner, A. M. Ultrafast Optical Pulse Shaping: A Tutorial Review. *Opt. Commun.* **2011**, *284* (15), 3669–3692.

(76) Myers, J. A.; Lewis, K. L.; Tekavec, P. F.; Ogilvie, J. P. Two-Color Two-Dimensional Fourier Transform Electronic Spectroscopy with a Pulse-Shaper. *Opt. Express* **2008**, *16* (22), 17420.

(77) Fuller, F. D.; Ogilvie, J. P. Experimental Implementations of Two-Dimensional Fourier Transform Electronic Spectroscopy. *Annu. Rev. Phys. Chem.* **2015**, *66*, 667–690.

(78) Hamm, P.; Zanni, M. *Concepts and Methods of 2D Infrared Spectroscopy*; Cambridge University Press: Cambridge, 2011.

(79) van Stokkum, I. H.; Larsen, D. S.; van Grondelle, R. Global and Target Analysis of Time-Resolved Spectra. *Biochim. Biophys. Acta* **2004**, *1657*, 82–104.

(80) Thyrhaug, E.; Žídek, K.; Dostál, J.; Bína, D.; Zigmantas, D. Exciton Structure and Energy Transfer in the Fenna–Matthews–Olson Complex. *J. Phys. Chem. Lett.* **2016**, *7* (9), 1653–1660.

(81) Mukamel, S. Communications: Signatures of Quasiparticle Entanglement in Multidimensional Nonlinear Optical Spectroscopy of Aggregates. *J. Chem. Phys.* **2010**, *132* (24), 241105.

(82) Scholes, G. D.; Smyth, C. Perspective: Detecting and Measuring Exciton Delocalization in Photosynthetic Light Harvesting. *J. Chem. Phys.* **2014**, *140* (11), 110901.

(83) Rodriguez, J.; Holten, D. Ultrafast Vibrational Dynamics of a Photoexcited Metalloporphyrin. *J. Chem. Phys.* **1989**, *91*, 3525–3531.

(84) Rodriguez, J.; Kirmaier, C.; Holten, D. Time-Resolved and Static Optical Properties of Vibrationally Excited Porphyrins. *J. Chem. Phys.* **1991**, *94*, 6020–6029.

(85) Enescu, M.; Steenkeste, K.; Tfibel, F.; Fontaine-Aupart, M.-P. Femtosecond Relaxation Processes from Upper Excited States of tetrakis(N-Methyl-4-Pyridyl)porphyrins Studied by Transient Absorption Spectroscopy. *Phys. Chem. Chem. Phys.* **2002**, *4*, 6092–6099.

(86) Timpmann, K.; Rätsep, M.; Hunter, C. N.; Freiberg, A. Emitting Excitonic Polaron States in Core LH1 and Peripheral LH2 Bacterial Light-Harvesting Complexes. *J. Phys. Chem. B* **2004**, *108* (29), 10581–10588.

(87) Perlík, V.; Hauer, J.; Šanda, F. Finite Pulse Effects in Single and Double Quantum Spectroscopies. *J. Opt. Soc. Am. B, JOSAB* **2017**, *34* (2), 430–439.

(88) Jumper, C. C.; van Stokkum, I. H. M.; Mirkovic, T.; Scholes, G. D. Vibronic Wavepackets and Energy Transfer in Cryptophyte Light-Harvesting Complexes. *J. Phys. Chem. B* **2018**, *122* (24), 6328–6340.

(89) Lin, S. W.; Groesbeek, M.; van der Hoef, I.; Verdegem, P.; Lugtenburg, J.; Mathies, R. A. Vibrational Assignment of Torsional Normal Modes of Rhodopsin: Probing Excited-State Isomerization Dynamics along the Reactive C11=C12 Torsion Coordinate. *J. Phys. Chem. B* **1998**, *102*, 2787–2806.

(90) Llansola-Portoles, M. J.; Pascal, A. A.; Robert, B. Electronic and Vibrational Properties of Carotenoids: From in Vitro to in Vivo. *J. R. Soc. Interface* **2017**, *14* (135). https://doi.org/10.1098/rsif.2017.0504.

(91) Diers, J. R.; Zhu, Y.; Blankenship, R. E.; Bocian, D. F. Q_y-Excitation Resonance Raman Spectra of Chlorophyll *a* and Bacteriochlorophyll *c*/*d* Aggregates. Effects of Peripheral Substituents on the Low-Frequency Vibrational Characteristics. *J. Phys. Chem.* **1996**, *100* (20), 8573–8579.

(92) Zhou, C.; Diers, J. R.; Bocian, D. F. Qy-Excitation Resonance Raman Spectra of Chlorophyll a and Related Complexes. Normal Mode Characteristics of the Low-Frequency Vibrations. *J. Phys. Chem. B* **1997**, *101* (46), 9635–9644.

(93) Roberts, S. T.; Loparo, J. J.; Tokmakoff, A. Characterization of Spectral Diffusion from Two-Dimensional Line Shapes. *J. Chem. Phys.* **2006**, *125* (8), 084502.

(94) Khalil, M.; Demirdöven, N.; Tokmakoff, A. Vibrational Coherence Transfer Characterized with Fourier-Transform 2D IR Spectroscopy. *J. Chem. Phys.* **2004**, *121* (1), 362–373.

(95) Thyrhaug, E.; Bogh, S. A.; Carro-Temboury, M. R.; Madsen, C. S.; Vosch, T.; Zigmantas, D. Ultrafast Coherence Transfer in DNA-Templated Silver Nanoclusters. *Nat. Commun.* **2017**, *8*, 15577.

(96) Sardjan, A. S.; Westerman, F. P.; Ogilvie, J. P.; Jansen, T. L. C. Observation of Ultrafast Coherence Transfer and Degenerate States with Polarization-Controlled Two-Dimensional Electronic Spectroscopy. *J. Phys. Chem. B* **2020**, *124* (42), 9420–9427.

(97) Tully, J. C. Nonadiabatic Molecular Dynamics. *Int. J. Quantum Chem.* **1991**, *40* (S25), 299–309.

(98) Yarkony, D. R. Current Issues in Nonadiabatic Chemistry. *J. Phys. Chem.* **1996**, *100* (48), 18612–18628.

(99) Tully, J. C. Perspective: Nonadiabatic Dynamics Theory. *J. Chem. Phys.* **2012**, *137* (22), 22A301.

(100) Curchod, B. F. E.; Martínez, T. J. Ab Initio Nonadiabatic Quantum Molecular Dynamics. *Chem. Rev.* **2018**, *118* (7), 3305–3336.

(101) Womick, J. M.; Moran, A. M. Exciton Coherence and Energy Transport in the Light-Harvesting Dimers of Allophycocyanin. *J. Phys. Chem. B* **2009**, *113* (48), 15747–15759.

(102) Womick, J. M.; Moran, A. M. Vibronic Enhancement of Exciton Sizes and Energy Transport in Photosynthetic Complexes. *J. Phys. Chem. B* **2011**, *115* (6), 1347–1356.

(103) Tiwari, V.; Peters, W. K.; Jonas, D. M. Electronic Resonance with Anticorrelated Pigment Vibrations Drives Photosynthetic Energy Transfer Outside the Adiabatic Framework. *Proc. Natl. Acad. Sci. U. S. A.* **2013**, *110* (4), 1203–1208.

(104) Tiwari, V.; Peters, W. K.; Jonas, D. M. Electronic Energy Transfer through Non-Adiabatic Vibrational-Electronic Resonance. I. Theory for a Dimer. *J. Chem. Phys.* **2017**, *147* (15), 154308.

(105) Jumper, C. C.; Rafiq, S.; Wang, S.; Scholes, G. D. From Coherent to Vibronic Light Harvesting in Photosynthesis. *Curr. Opin. Chem. Biol.* **2018**, *47*, 39–46.

(106) Cao, J.; Cogdell, R. J.; Coker, D. F.; Duan, H.-G.; Hauer, J.; Kleinekathöfer, U.; Jansen, T. L. C.; Mančal, T.; Miller, R. J. D.; Ogilvie, J. P.; Prokhorenko, V. I.; Renger, T.; Tan, H.-S.; Tempelaar, R.; Thorwart, M.; Thyrhaug, E.; Westenhoff, S.; Zigmantas, D. Quantum Biology Revisited. *Sci Adv* **2020**, *6* (14), 2375–2548.

(107) Wang, Q.; Schoenlein, R. W.; Peteanu, L. A.; Mathies, R. A.; Shank, C. V. Vibrationally Coherent Photochemistry in the Femtosecond Primary Event of Vision. *Science* **1994**, *266* (5184), 422–424.

(108) Levine, B. G.; Martínez, T. J. Isomerization through Conical Intersections. *Annu. Rev. Phys. Chem.* **2007**, *58*, 613–634.

(109) Polli, D.; Altoè, P.; Weingart, O.; Spillane, K. M.; Manzoni, C.; Brida, D.; Tomasello, G.; Orlandi, G.; Kukura, P.; Mathies, R. A.; Garavelli, M.; Cerullo, G. Conical Intersection Dynamics of the Primary Photoisomerization Event in Vision. *Nature* **2010**, *467* (7314), 440–443.

(110) Schapiro, I.; Ryazantsev, M. N.; Frutos, L. M.; Ferré, N.; Lindh, R.; Olivucci, M. The Ultrafast Photoisomerizations of Rhodopsin and Bathorhodopsin Are Modulated by Bond Length Alternation and HOOP Driven Electronic Effects. *J. Am. Chem. Soc.* **2011**, *133* (10), 3354–3364.

(111) Halpin, A.; Johnson, P. J. M.; Dwayne Miller, R. J. Comment on "Engineering Coherence among Excited States in Synthetic Heterodimer Systems." *Science* **2014**, *344* (6188), 1099–1099.

(112) De Sio, A.; Lienau, C. Vibronic Coupling in Organic Semiconductors for Photovoltaics. *Phys. Chem. Chem. Phys.* **2017**, *19* (29), 18813–18830.

(113) Rozzi, C. A.; Falke, S. M.; Spallanzani, N.; Rubio, A.; Molinari, E.; Brida, D.; Maiuri, M.; Cerullo, G.; Schramm, H.; Christoffers, J.; Lienau, C. Quantum Coherence Controls the Charge Separation in a Prototypical Artificial Light-Harvesting System. *Nat. Commun.* **2013**, *4*, 1602.

(114) Falke, S. M.; Rozzi, C. A.; Brida, D.; Maiuri, M.; Amato, M.; Sommer, E.; De Sio, A.; Rubio, A.; Cerullo, G.; Molinari, E.; Lienau, C. Coherent Ultrafast Charge Transfer in an Organic Photovoltaic Blend. *Science* **2014**, *344* (6187), 1001–1005.

(115) Atchity, G. J.; Xantheas, S. S.; Ruedenberg, K. Potential Energy Surfaces near Intersections. *J. Chem. Phys.* **1991**, *95* (3), 1862–1876.

(116) Michl, J. Historical Introduction. In *Conical Intersections: Electronic Structure, Dynamics & Spectroscopy*; Domcke, W., Yarkony, D., Köppel, H., Eds.; World Scientific: Singapore, 2004; pp ix – xiii.

(117) Matsika, S.; Krause, P. Nonadiabatic Events and Conical Intersections. *Annu. Rev. Phys. Chem.* **2011**, *62*, 621–643.

(118) Peters, W. K.; Smith, E. R.; Jonas, D. M. Femtosecond Pump-Probe Polarization Spectroscopy of Vibronic Dynamics at Conical Intersections and Funnels. In *Conical Intersections: Theory, Computation and Experiment*; Domcke, W., Yarkony, D. R., Köppel, H., Eds.; 2011; pp 715–745.

(119) Guo, H.; Yarkony, D. R. Accurate Nonadiabatic Dynamics. *Phys. Chem. Chem. Phys.* **2016**, *18* (38), 26335–26352.

(120) Kowalewski, M.; Bennett, K.; Mukamel, S. Cavity Femtochemistry: Manipulating Nonadiabatic Dynamics at Avoided Crossings. *J. Phys. Chem. Lett.* **2016**, *7* (11), 2050–2054.

(121) Mangaud, E.; Lasorne, B.; Atabek, O.; Desouter-Lecomte, M. Statistical Distributions of the Tuning and Coupling Collective Modes at a Conical Intersection Using the Hierarchical Equations of Motion. *J. Chem. Phys.* **2019**, *151* (24), 244102.

(122) Ben-Nun, M.; Martínez, T. J. Photodynamics of Ethylene: Ab Initio Studies of Conical Intersections. *Chem. Phys.* **2000**, *259* (2), 237–248.

(123) Larsen, R. E.; Schwartz, B. J. Nonadiabatic Molecular Dynamics Simulations of Correlated Electrons in Solution. 1. Full Configuration Interaction (CI) Excited-State Relaxation Dynamics of Hydrated Dielectrons. *J. Phys. Chem. B* **2006**, *110* (19), 9681–9691.

(124) Messina, F.; Pomarico, E.; Silatani, M.; Baranoff, E.; Chergui, M. Ligand-Centred Fluorescence and Electronic Relaxation Cascade at Vibrational Time Scales in Transition-Metal Complexes. *J. Phys. Chem. Lett.* **2015**, *6* (22), 4475–4480.

(125) Fazzi, D.; Barbatti, M.; Thiel, W. Modeling Ultrafast Exciton Deactivation in Oligothiophenes via Nonadiabatic Dynamics. *Phys. Chem. Chem. Phys.* **2015**, *17* (12), 7787–7799.

(126) Rafiq, S.; Scholes, G. D. From Fundamental Theories to Quantum Coherences in Electron Transfer. *J. Am. Chem. Soc.* **2019**, *141* (2), 708–722.

(127) Premvardhan, L.; Papagiannakis, E.; Hiller, R. G.; van Grondelle, R. The Charge-Transfer Character of the $S_0 \rightarrow S_2$ Transition in the Carotenoid Peridinin Is Revealed by Stark Spectroscopy. *J. Phys. Chem. B* **2005**, *109* (32), 15589–15597.

(128) Bonačić-Koutecký, V.; Koutecký, J.; Michl, J. Neutral and Charged Biradicals, Zwitterions, Funnels in S_1, and Proton Translocation: Their Role in Photochemistry, Photophysics, and Vision. *Angew. Chem. Int. Ed.* **1987**, *26* (3), 170–189.

(129) Perlík, V.; Seibt, J.; Cranston, L. J.; Cogdell, R. J.; Lincoln, C. N.; Savolainen, J.; Šanda, F.; Mančal, T.; Hauer, J. Vibronic Coupling Explains the Ultrafast Carotenoid-to-Bacteriochlorophyll Energy Transfer in Natural and Artificial Light Harvesters. *J. Chem. Phys.* **2015**, *142*, 212434.

(130) Ramanan, C.; Ferretti, M.; van Roon, H.; Novoderezhkin, V. I.; van Grondelle, R. Evidence for Coherent Mixing of Excited and Charge-Transfer States in the Major Plant Light-Harvesting Antenna, LHCII. *Phys. Chem. Chem. Phys.* **2017**, *19* (34), 22877–22886.

(131) Nelson, T.; Fernandez-Alberti, S.; Roitberg, A. E.; Tretiak, S. Electronic Delocalization, Vibrational Dynamics, and Energy Transfer in Organic Chromophores. *J. Phys. Chem. Lett.* **2017**, *8* (13), 3020–3031.

(132) Ferrari, A. C. Raman Spectroscopy of Graphene and Graphite: Disorder, Electron–phonon Coupling, Doping and Nonadiabatic Effects. *Solid State Commun.* **2007**, *143* (1), 47–57.

Chapter 4: Vibronic Coherences in Colloidal Quantum Dots

In strongly-confined quantum dots (QDs), surface ligands are an integral part of the QD's electronic structure. Depending on the strength of the coupling between the vibration modes of the ligands and the core electronic states of the QD, the ligands can strongly promote or attenuate, respectively, the extension of the exciton wavefunction outside the QD core. Here we demonstrate experimentally the presence and tuning of vibronic coherence in CdSe QDs of different sizes and surface composition. Broadband two-dimensional electronic spectroscopy reveals resolved vibronic progression at short time in amine-capped CdSe QDs, as well as deep, rapidly damped modulations corresponding to mid-frequency ligand modes. Oleate-capped CdSe QDs are reported to exhibit attenuated modulations at lower frequencies, as well as a much slower rate of hot carrier relaxation. These findings demonstrate the ability to control hot carrier cooling by varying surface composition in strongly confined QDs.

† The work presented in this chapter features contributions from Dr. P. Gregory Van Patten at Middle Tennessee State University.

4.1 Introduction

Colloidal semiconductor quantum dots (QDs) are quantum confined nanomaterials, exhibiting tunable electronic properties dependent on the size, shape, and composition of the crystal.[1–4] The quantum confinement effects of these colloidal QDs have been of considerable interest due to their photoluminescent properties,[5] and as laser gain media.[6–10] However, QDs are most notable for their potential in photocatalysis applications[11,12] and photovoltaic devices.[13] Colloidal QDs, however, perform inefficiently due to ultrafast nonradiative relaxation of optically prepared hot carriers, as the excess energy is dissipated rapidly via an Auger mechanism.[14,15]

Several studies have shifted focus to their multicarrier exciton generation properties,[13,16–18] or their potential in solar luminescent concentration devices[19] as alternative approaches to photovoltaic applications. More interestingly, recent developments have focused on the role of surface trapping states and organic capping ligands in the hot carrier cooling process.[20,21] One hypothesis implicates the vibrations of surface ligands merely as classical promoting (or bath) modes, which would accept the excess energy of the donor state in an incoherent energy transfer mechanism.[20,22–24]

Instead, in this study we propose a nonradiative process involving *vibronic excitons*, arising from quantum coherent mixing of ligand vibrations with the extensively delocalized core electronic states (Figure 3.1). Using femtosecond broadband two-dimensional electronic spectroscopy (2DES), we provide the first evidence that coherent vibronic wavepacket motions involving mid-frequency modes of the surface ligands control the rate of cooling of carrier states to the band edge by a nonadiabatic mechanism. An important implication of these findings is that

the QDs present an opportunity to learn how the structural features of an energy material can be manipulated to optimize its function through control of its coherence properties.

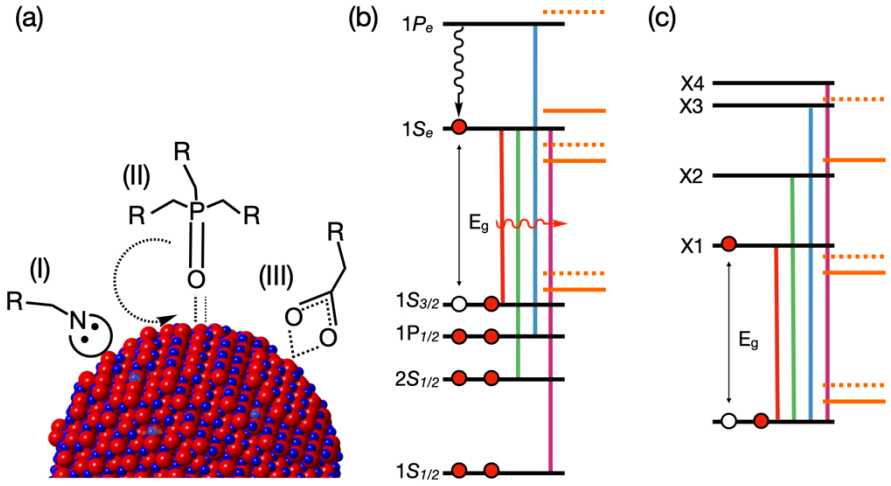

Figure 4.1. Example of CdSe QD capped with organic surface ligands and possible coupling of core electronic states in QDs with ligand vibrations, after Lifshitz.[21] (a) Alkylamine (I), trioctylphosphineoxide (TOPO, II), and alkylcarboxyl (III) ligands and ligation to metal cation (e.g. Cd^{2+}) and anion (chalcogen, e.g. Se^{2-}) sites, with R representing alkane or alkene substituents. (b) Coupling of core QD electronic (black) states and ligand bonding (solid red) and antibonding (dashed red) states. (c) Exciton manifold for the first four bound electron-hole pairs formed upon excitation, labeled X1 through X4.

4.2 Experimental

4.2.1 Sample Preparation

In our studies, CdSe QDs were synthesized and provided through collaboration with the Van Patten laboratory. The QDs were synthesized following a refined procedure based on methods applied by Wu et al.[25] and Jasieniak et al.[26] The method involves a hot injection technique that employs cadmium stearate, hexadecylamine (HDA), hexadecyl palmitate (HP), trioctylphosphine (TOP), and trioctylphosphine selenide (TOPSe) as reactive and growth control agents throughout the reaction. In this procedure, the selenide precursor is introduced to the reaction mixture at temperatures of 260-330 °C, with growth temperatures ranging from 250-270 °C. The growth of larger particles, as featured in this chapter, require additional, gradually

injected Cd and Se precursors at the growth temperature. Approximately 1 mL of precursors is introduced over a growth period of ~30 mins. Further optimization of shape and crystallinity is achieved with incubation ah 150 °C for a few hours. This final step results in an improved photoluminescence quantum yield. The particles exhibit a mixture of predominantly wurtzite phase and signatures of zincblende.

The particles produced exhibited uniform spherical structure with a size polydispersity on the order of 5-6 % (See Appendix). This degrees of size and shape monodispersity is highly unusual, especially for larger-sized particles.[27–31] This preparation provide a significant advantage in the study of hot carrier cooling through the ability to reduce the static inhomogeneity arising from broad size and shape polydispersity, as featured in previous work in other groups.[32–36]

The characterization of the QDs follows a delicate purification technique. Aliquots of the QD reaction mixture are combined with equal amounts of ethanol (or methanol), and a small volume (three drops) of acetone. The solution is then subject to centrifugation at 13 G for 1 minute. The precipitate QDs are resuspended in either toluene or chloroform, and subject to a second round of treatment.

As synthesized, the CdSe QDs are capped with a variety of organic ligands present in the initial reaction mixture. These ligands include HDA, stearate, and TOP oxide (TOPO). The application of FTIR, NMR, and direct analysis in real time mass spectrometry (DART-MS) successfully confirmed the presence of ligands at the surface of the QDs (see Appendix). In this present study, one ligand exchange procedure was performed on a small sample of CdSe QDs. This procedure involved the addition of an excess amount of oleic acid to CdSe QDs suspended

in chloroform, heated to 50 °C for 15 mins. The QDs were again purified and resuspended in toluene for the 2DES experiment.

In this study, we were provided two samples of CdSe QDs, each capped with HDA, stearates, and TOPO. The samples were 6.9 nm and 6.0 nm in diameter, and exhibited high size and shape monodispersity. The smaller 6.0 nm QDs were subject to a post-synthesis ligand exchange, as mentioned above. The HDA, stearate and TOPO ligands were replaced, predominantly, with oleate ligands.

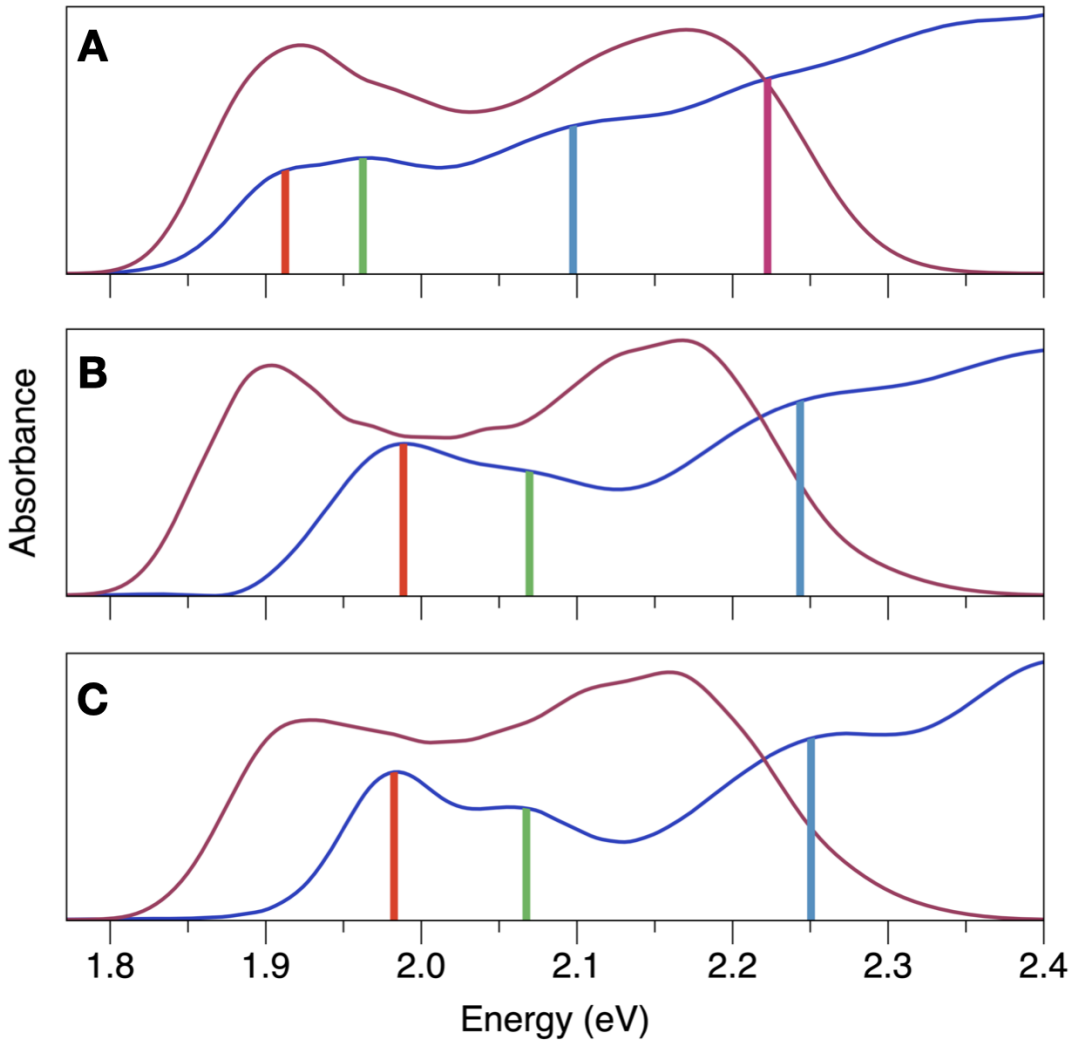

Figure 4.2. Linear absorption spectra (*blue*) of CdSe QDs, with broadband laser spectrum superimposed (*red*). (a) CdSe QDs of 6.9 nm diameter size, capped in HDA, stearates, and TOP/TOPO; (b) CdSe QDs of 6.0 nm diameter, capped with HDA, stearates, TOP/TOPO; (c) CdSe QDs of 6.0 nm diameter, capped in oleates. Vertical colored bars represent exciton transitions (Figure 3.1): X1 (*red*), X2 (*green*), X3 (*blue*), X4 (*purple*).

4.2.2 Femtosecond Spectroscopy

The experiments featured in this chapter employ broadband two-dimensional electronic spectroscopy (2DES). The 2DES experiment is a third-order nonlinear spectroscopy applying a sequence of three excitation pulses with two scanned interpulse time intervals.[37] In the current implementation of the technique in the Beck laboratory, which is derived from the approach using pulse shapers described by Zanni and coworkers[38,39] and by Ogilvie and coworkers[40,41] these pulses are delivered to the sample into two beams, the pump (excitation) and probe (detection) beams. An adaptive pulse shaper is inserted in each beam to correct the residual second- and third-order optical phase terms measured at the sample position, obtaining a Fourier transform-limited bandwidth–duration relationship.[42] During the experiment, an additional phase mask is added by the pump beam's shaper to prepare a pair of pump pulses with a relatively short time interval between them, the coherence delay, $\tau < 50$ fs. These pulses arrive at fixed waiting (or population) time, T, prior to the arrival of a single probe pulse at the sample. The detection axis (ωt) of the 2D spectrum is obtained directly by measuring the pump-induced change in probe transmission of the sample, with the dispersed signal acquired fully across the laser spectrum. This measurement is performed by detecting the amplitude of the transmitted probe beam using a spectrograph and a fast CCD detector with a pump-amplitude modulation, lock-in detection scheme similar to that described by Augulis and Zigmantas.[43] The excitation axis of the 2D spectrum (ω_τ) is determined by scanning the delay τ between the two pump pulses, usually at 0.5 fs intervals over the 0–50 fs range, and Fourier transforming the resulting signal time series.

The 2DES spectrum can be interpreted qualitatively as a correlation spectrum:[37] for a particular waiting time *T*, the signal amplitude at a given (*x*,*y*) coordinate is the result of the action of a specific optical frequency *x* from the excitation pulses ($\omega\tau$) followed by action of a

certain frequency y from the probe pulse (ω_t). By varying T, one can observe the time evolution of the populations and coherences prepared by the excitation pulses. This feature of 2DES allows one to correlate the mechanisms that mediate hot carrier cooling to the band edge following photoexcitation of the strong exciton transitions in QDs. Further, a powerful feature of 2DES is its ability to improve the resolution of congested spectral line shapes. Colloidal QDs exhibit static inhomogeneity owing to size and shape dispersion and inhomogeneous line broadening from random energy fluctuations particularly in the surroundings.

4.3 Results and Discussion

In order to identify the nonradiative relaxation mechanism of the hot carrier in semiconductor QDs, we performed new 2DES experiments on CdSe QDs with dominantly wurtzite crystal phase and two differently sized diameters: 6.0 nm and 6.9 nm. The 2DES experiment employed 6.5-7.5 fs laser pulses with 520-710 nm (1.75-2.4 eV) bandwidth which photoselects the three lowest-lying exciton transitions (Figure 3.2): $1S_h \rightarrow 1S_e$ (X1), $2S_h \rightarrow 1S_e$ (X2), and $1P_h \rightarrow 1P_e$ (X3). Replacement of amine ligands with carboxylate ligands in the 6.0 nm CdSe QDs resulted in a complete transformation of the mid-frequency coherent wavepacket motions and a dramatic effect on the hot carrier cooling kinetics.

Table 4.1. Energy of the exciton transitions photoselected in the 2DES experiments.

QD	X1 (eV)	X2 (eV)	X3 (eV)	X4 (eV)
6.9 nm HDA/stearate/TOPO	1.91	1.96	2.10	2.22
6.0 nm HDA/stearate/TOPO	1.99	2.07	2.25	-
6.0 nm oleate	1.98	2.06	2.25	-

Figure 4.3 shows the evolution of the 2DES spectra from 6.9 nm CdSe QDs capped with stearates, HDA, and TOP, recorded with the 6.5 fs laser pulses over a waiting time T = 2.5-1000 fs range. The effective exciton transition energies are reported in Table 4.1, and are represented by vertical lines in the linear absorption spectrum to the right of Figure 4.2. Exciton transition coordinates corresponding to X1 and X3 are marked on the diagonal in Figure 4.3 (A, B). The off-diagonal, B, marks the arrival of population at the bandedge following optical excitation of the X3 exciton.

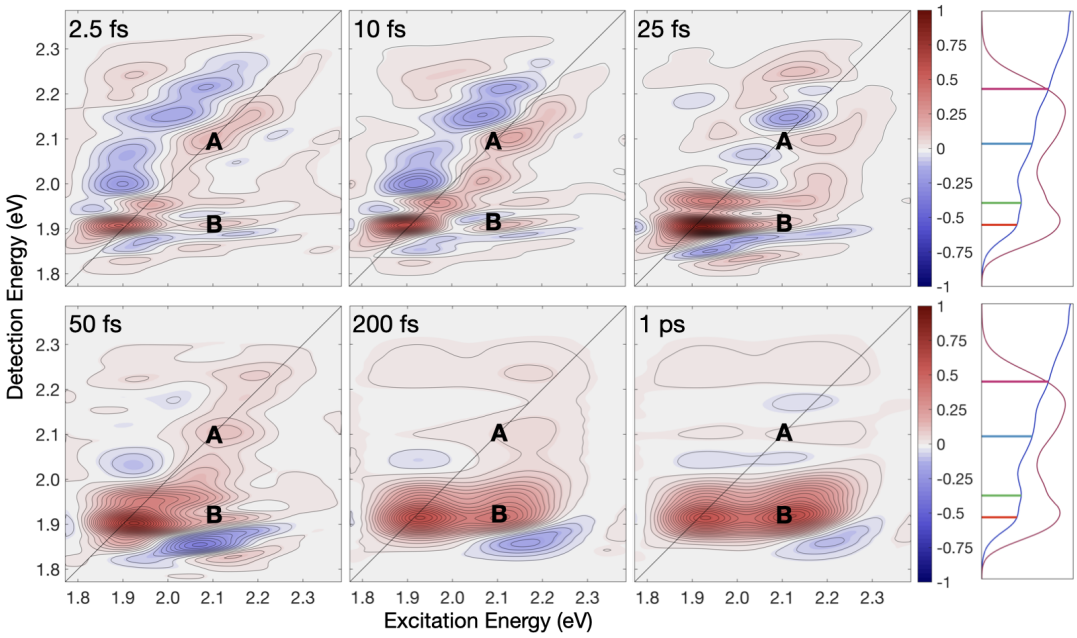

Figure 4.3. Phased absorptive 2DES spectra at waiting times T = 2.5, 10, 25, 50, 200 and 1000 fs in CdSe QDs (6.9 nm) with hexadecylamine, stearate and trioctylphosphine capping ligands in toluene solvent. The spectra are presented with evenly spaced contours and are tinted with colors indicating positive (red, GSB/SE) and negative (blue, ESA/PA) signals. The right panel shows the overlap of the three lowest exciton transitions in the linear absorption spectrum from the QDs with the laser spectrum (from 7.5 fs pulses centered at 595 nm). Coordinates A (on diagonal GSB/SE) and B (off-diagonal SE cross peak) follow preparation of the $1P_e$ state via the X3 transition and the subsequent formation of the $1S_e$ state via hot carrier cooling, respectively. C marks the on-diagonal GSB/SE signal from the X1 $1S_h \rightarrow 1S_e$ band-edge transition. Figure 4.4 shows amplitude transients for the marked coordinates.

Upon initial analysis of the 2DES spectra at early time, one can easily identify positive-going ground-state bleaching (GSB) of the different exciton transitions of the CdSe QDs along the diagonal. Each GSB response on the diagonal corresponds to a specific exciton transition, X1 through X4 (Figure 4.1). Resolved excited state absorption (ESA) responses are present above and below the diagonal at early time. The ESA responses can be assigned to different photophysical dynamics, including surface traps,[2,36,44,45] stark-effect,[46,47] and biexcitons.[33,34,48,49]

At early waiting times (T < 15 fs), several off-diagonal peaks are resolved in the 2DES spectra. While some of these responses can be assigned to possible instantaneous stark-shift, another possibility would be to describe the grid-like pattern to a vibronic progression between the vibrational levels of the ground electronic state, of the resonant electronic excited state at a given excitation energy, and of at least one electronic state lying to higher energy. Similar patterns have been observed previously in 2DES studies of nonadiabatic transitions in organic molecules.[50,51] As shown in Figure 4.3, at a waiting time of T = 2.5 fs, the 2DES spectra reveals principle peak spacings for GSB/SE and ESA signals corresponding to several prominent mid-frequency (300-1000 cm^{-1}) vibrations. At longer waiting times, such as T = 50 fs and 100 fs, the initially resolved vibronic progression has broadened to display mainly the principal exciton energy level spacings. The end result is a horizontal SE stripe of cross peaks in the 2DES spectrum centered at the band edge transition, corresponding to population of the product $1S_e$ state fully across the bandwidth of the exciton pulses. The frequencies observed during the vibronic progression are much too large to include CdSe phonon modes (~210 cm^{-1}). Instead, they match the mid-frequencies of the HDA ligands at the surface of the quantum dot.[52]

While the resolved vibronic progression involving ligand frequencies at short time is unprecedented in the 2DES spectra, analysis of the amplitude change over time at specific

exciton energy reveals additional details comparable to findings in previous work.[35,36] The on-diagonal signal at the X1 transition exhibits low-frequency amplitude modulation at 210 cm^{-1}. This value is in good agreement with the frequency observed for the longitudinal phonon mode in CdSe QDs. Additionally, ESA or photoinduced absorption (PA) signals are detected at 2.05 eV in the 2DES spectra, similar to that reported by Caram et al.[36] These signals can be assigned to potential surface trap states, a result of unpassivated sites at the surface of the QD which can reduce the photoluminescence quantum yield. At longer waiting times, like $T = 1$ ps, we also observe the presence of an ESA cross peak at 1.85 eV on the detection axis corresponding to the ground state biexciton in CdSe QDs, which has been previously observed in 2DES studies.[33,34,36]

The main result of this study, however, focuses on the nonradiative relation of the hot carrier, X3, transition. Optical preparation of the X3 exciton is followed by rapid carrier cooling with sub-picosecond time constants. Previous studies have assigned this fast relaxation process to an Auger-like mechanism through pump-probe measurements with narrow band excitation.[14,15,53–55] The 2DES study reported here reveals additional information on the processes that mediate the hot carrier cooling through analysis of the transient signals at the marked coordinates A and B in Figure 4.3. The transients for these coordinates are shown in Figure 4.4, along with their respective models.

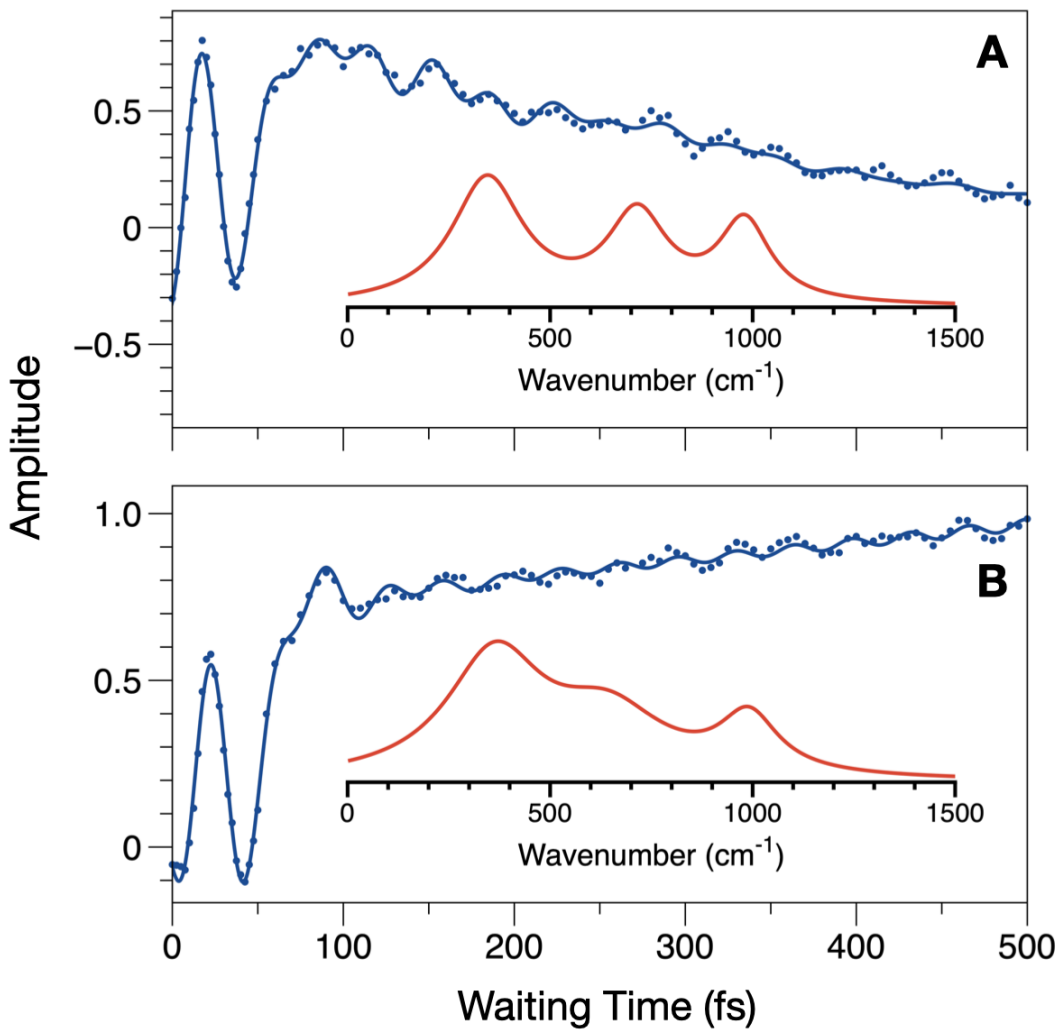

Figure 4.4. Amplitude transients for the marked coordinates in the 2DES spectra (Figure 4.3), with superimposed LPSVD models. Coordinates A and B follow optical preparation of the $1P_e$ state and the formation of the $1S_e$ state due to hot carrier cooling; A decays with a time constant of 188 fs, B rises with a 182 fs time constant. The LPSVD models show that both transients are modulated by rapidly damped quantum beating at amine and carboxylate ligand-derived frequencies: (a) 344 cm^{-1}, 715 cm^{-1}, and 980 cm^{-1} with damping times of 200 fs, 40 fs, and 60 fs, respectively; and (b) 367 cm^{-1}, 625 cm^{-1}, and 985 cm^{-1} with damping times of 200 fs, 30 fs, and 60 fs, respectively.

The population decays from the optically prepared $1P_e$ state, as seen on the diagonal at 2.10 eV, to the $1S_e$ band-edge state (cross peak at 1.91 eV) in ~180 fs. This value is in good agreement with results reported in 2DES experiments by Caram et al.[36] and with pump-probe experiments by Klimov and coworkers.[15,53] More interestingly, however, is the modulation of the amplitude of the transients at both coordinates, A and B (Figure 4.4). These high-frequency modulations are rapidly damped (<100 fs), and could therefore not be observed in traditional pump-probe experiments. Linear prediction singular value decomposition (LPSVD) analysis (Table 4.1) of the modulated amplitudes were carried out to model the signals measured. The modulated signals reveal the involvement of coherent vibronic wavepacket motions at three principal organic frequency ligands, corroborating the assignment of the vibronic progression in the short time 2DES spectra. The highest frequencies, and most rapidly damped modulation components, at ~700 cm^{-1} and 980 cm^{-1}, are in the frequency range for NH_2-bending and out-of-plane motions of the alkyl backbone of the HDA capping ligands.[52] The lowest frequency component, 350 cm^{-1}, is slowly damped in comparison, and could be assigned to potential carboxylate motion.

Table 4.1. Model parameters for the modulation components detected in the amplitude transients detected at the X3X3 (A) and X3X1 (B) coordinates in the 2DES spectra (Figures 4.4, 4.6, and 4.8).

QD and coordinate	*A*	ω (cm^{-1})	φ (rad)	τ (fs)
6.9 nm, HDA **X3X3**[a]	0.49	340 ± 20	0.20	200 ± 10
	0.28	720 ± 30	3.70	40 ± 10
	0.22	980 ± 40	2.80	60 ± 5
6.9 nm, HDA **X3X1**[b,c]	2.15	370 ± 10	0.20	200 ± 10
	1.73	630 ± 40	3.60	30 ± 9
	083	990 ± 40	2.50	60 ± 10
6.0 nm, HDA **X3X3**[a]	0.67	260 ± 10	4.50	40 ± 7
	0.59	670 ± 20	4.20	55 ± 10
	0.33	950 ± 50	3.00	90 ± 20
6.0 nm, HDA **X3X1**[a]	0.52	200 ± 10	3.80	360 ± 90
	0.89	530 ± 50	4.50	40 ± 10
	0.95	1000 ± 80	5.60	70 ± 10
6.0 nm, oleate **X3X3**[a]	0.019	200 ± 10	2.50	360 ± 70
	0.010	570 ± 30	2.20	40 ± 10
6.0 nm, oleate **X3X1**[a]	0.019	220 ± 10	2.50	340 ± 70
	0.012	360 ± 10	2.70	90 ± 10
	0.010	720 ± 30	1.70	30 ± 5

Table 4.1 (cont'd)
a. sum of rising, damped cosinusoids,
$\Sigma_i A_i \cos(\omega_i T - \varphi_i) \cdot \exp(-T/\tau_i)$
b. sum of rising, damped cosinusoids,
$A_r (1 - \exp(-T/\tau_r)) \Sigma_i A_i \cos(\omega_i T - \varphi_i) \cdot \exp(-T/\tau_i)$
c. $A_r = 0.57$, $\tau_r = 31 \pm 4$ fs

An important finding in the LPSVD model is the apparent phase of the modulation. The analysis of the phase rules out an assignment of quantum beating. Unlike the antiphase modulations with respect to the waiting time, *T*, that one would expect at the diagonal and cross peak from a quantum beating signal arising from a stimulated Raman coherence, the modulation pattern exhibits essentially in-phase modulations with small delay between them (10-20 fs from A to B). This behaviour is the signature of a nonadiabatic passage from $1P_e$ to $1S_e$ of the vibronic wavepacket, with retention of the phase in the product state. The trajectory of the vibronic wavepacket is apparently such that a fraction of the population on the initial state's potential energy surface crosses through a conical intersection (CI)[56] to that of the product state with each vibration.

One might argue that the high-frequency modulations may be intrinsic to the core exciton splitting within the QD. While this argument can be countered by the fact that the X1 and X3 exciton states are separated by 2000 cm^{-1}, we can address such concerns with additional 2DES experiments on smaller CdSe QDs, with a diameter of 6.0 nm. An advantage of QDs is the size dependent exciton transitions. In addition to the interband gap increase, the intraband transitions also feature increased energy spacing. This will result in a significant shift of the exciton transition frequencies. The 6.0 nm QDs were prepared similar to those discussed above, and therefore contain the same combination of organic surface ligands at the start. However, additional steps were taken to alter the surface composition to that of primarily oleate (carboxylate) ligands.

Figure 4.5 below shows the time evolution of the 2DES spectra, from $T = 2.5$ fs to 1000 fs, for 6.0 nm CdSe QDs capped with HDA, stearates and TOP/TOPO. As expected, the spectral features are blue shifted along the excitation axis, due to the smaller sized particle and greater quantum confinement effects. As a result of the shift in the absorption spectrum to higher energy, the excitation bandwidth only resolves the first three exciton transitions. It is also worth noting that the intensity of the laser spectrum over the X3 transition at 2.25 eV is lower than observed in the 6.9 nm QD study. Therefore, we are only able to observe lower energy X3 transitions. Just observed in the similarly encapsulated 6.9 nm CdSe QDs, the short time spectra ($T = 2.5$ fs) exhibits resolved vibronic progression along the detection energy axis, with frequency spacings ranging from 300-1000 cm^{-1}. As the waiting time progresses, the spectral features broaden, dominated by SE response at the bandedge (1.99 eV) across the bandwidth of the excitation spectrum. Interestingly, we also observe strong and persistent ESA or PA above the diagonal. This can be assigned to a possible increase in surface trap states at higher energy. Due to the smaller sized QD, and geometric restrictions, there lies the potential for more unpassivated sites at the surface than observed in larger QDs.

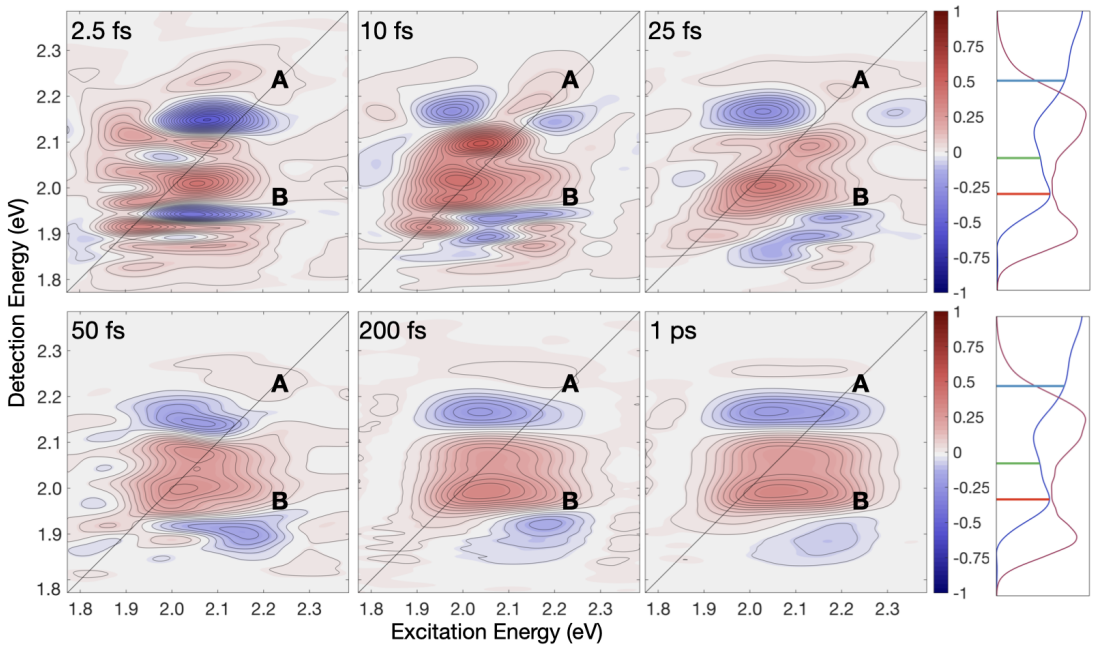

Figure 4.5. Phased absorptive 2DES spectra at waiting times $T = 5$ to 1000 fs in CdSe QDs (6.0 nm) with hexadecylamine, stearate, and trioctylphosphine oxide capping ligands in toluene solvent. The spectra are presented with evenly spaced contours and are tinted with colors indicating positive (red, GSB) and stimulated-emission (SE)) and negative (blue, excited-state absorption (ESA)) signals. The top panel shows the overlap of the four lowest exciton transitions in the linear absorption spectrum from the QDs with the laser spectrum (from 7.0 fs pulses centered at 600 nm).

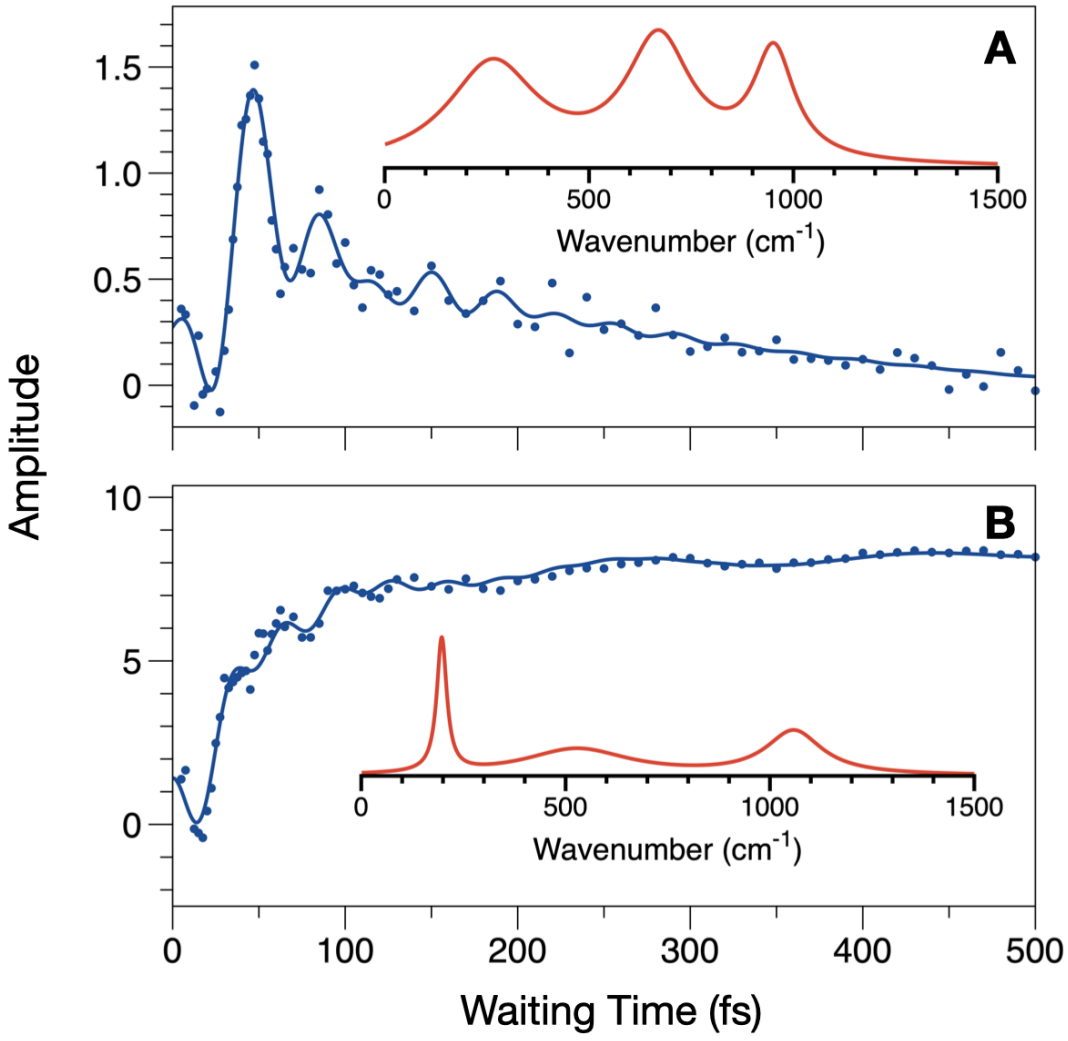

Figure 4.6. Amplitude transients for the marked coordinates in the 2DES spectra (Figure 4.5), with superimposed LPSVD models. Coordinates A and B follow optical preparation of the $1P_e$ state and the formation of the $1S_e$ state due to hot carrier cooling; A decays with a time constant of 171 fs, B rises with a 160 fs time constant. The LPSVD models show that both transients are modulated by rapidly damped quantum beating at amine and carboxylate ligand-derived frequencies: (a) 264 cm^{-1}, 670 cm^{-1}, and 952 cm^{-1} with damping times of 40 fs, 55 fs, and 90 fs, respectively; and (b) 197 cm^{-1}, 527 cm^{-1}, and 1058 cm^{-1} with damping times of 360 fs, 35 fs, and 65 fs, respectively.

Further analysis of the transients at the $1P_e$ transition coordinate on the diagonal reveals similar features as observed in the 6.9 nm QDs. Firstly, the rate of relaxation of the hot carrier from the $1P_e$ state to the $1S_e$ state in the 6.0 nm QDs are notably faster. The unmodulated kinetics reveal ~160 fs time constant for relaxation. This trend follows previous observations for the Auger mechanism, where the rate of relaxation is inversely proportional to particle size.[9,24,57–59] More importantly, however, is the modulation pattern. Despite the shift in the exciton transition energies, the frequency of modulation from the initial state to the final product state is essentially the same, within our margins of error (Table 4.1). The mid- to to high-frequency components decay rapidly (<100 fs), but are still longer than expected for electronic dephasing. The vibronic progression can be supported by these longer lived coherences, as population transfers from the $1P_e$ state to the $1S_e$ state.

The mid to high-frequency modulations can again be attributed to the HDA ligands at the surface of the QD. And, once again, we observe a very small time shift (<20 fs) in the modulation pattern between the two states. The phase relationship between the modulation patterns are more complex. High frequency modulations at short time appear more antiphase in character when compared to one another, which is a signature of quantum beating.

Figure 4.7 features 2DES spectra for waiting times of T = 2.5 to 1000 fs of CdSe QDs with a diameter of 6.0 nm capped primarily with oleates. Here, at short time (T = 2.5 and 10 fs), we observe the vibronic progression in the resolved cross peaks in the 2DES spectra. However, the cross peaks are less resolved when compared to the HDA capped QDs reported above.

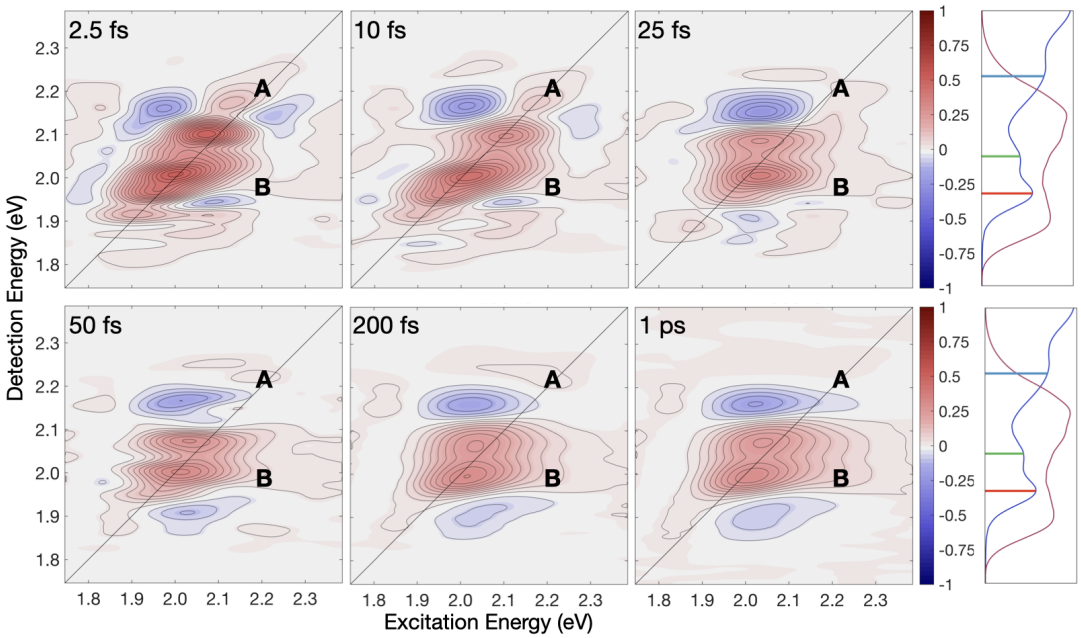

Figure 4.7. Phased absorptive 2DES spectra at waiting times $T = 2.5$ to 1000 fs in CdSe QDs (6.0 nm) with oleate capping ligands in toluene solvent. The spectra are presented with evenly spaced contours and are tinted with colors indicating positive (red, GSB and SE) and negative (blue, ESA) signals. The top panel shows the overlap of the four lowest exciton transitions in the linear absorption spectrum from the QDs with the laser spectrum (from 6.5 fs pulses centered at 595 nm).

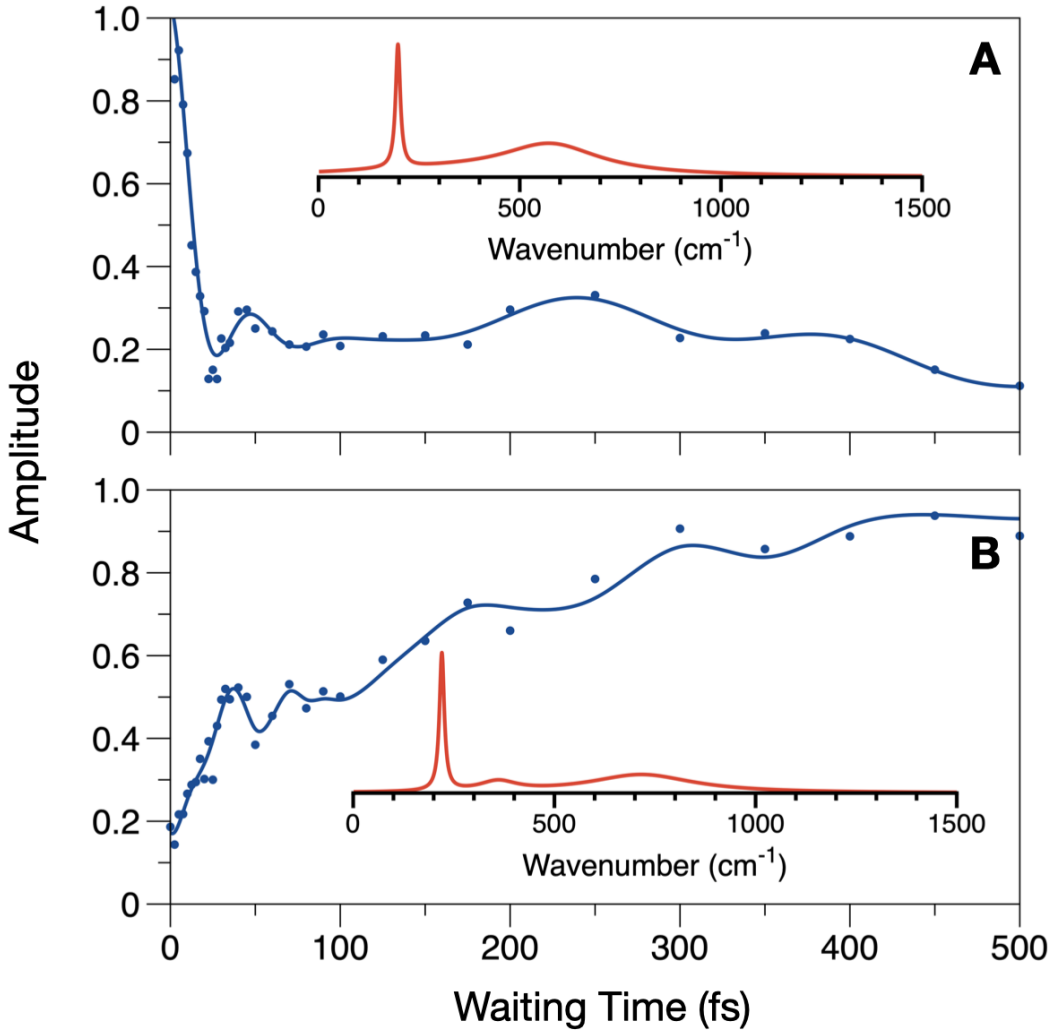

Figure 4.8. Amplitude transients for the marked coordinates in the 2DES spectra (Figure 4.7), with superimposed LPSVD models. Coordinates A and B follow optical preparation of the $1P_e$ state and the formation of the $1S_e$ state due to hot carrier cooling; B rises with a 257 fs time constant. The LPSVD models show that both transients are modulated by rapidly damped quantum beating at amine and carboxylate ligand-derived frequencies: (a) 200 cm^{-1}, and 576 cm^{-1} with damping times of 356 fs, and 36 fs, respectively; and (b) 220 cm^{-1}, 360 cm^{-1}, and 717 cm^{-1} with damping times of 339 fs, 94 fs, and 33 fs, respectively.

The 2DES transients at the coordinates corresponding to optical excitation of the X3 transition on the diagonal at an energy of 2.25 eV reveal drastic changes in the nonradiative relaxation dynamics (Figure 4.8). As evident in the transient at the off-diagonal for the $1S_e$ band-edge, the overall rate of population transfer from the $1P_e$ state to the $1S_e$ state is significantly slower, with a time constant of ~250 fs for nonmodulated part of the model. Additionally, we observe different frequencies of modulation, arising from the oleate ligands at ~300 cm^{-1}, and ~650 cm^{-1}. Another major difference is the notable depth of the modulation when compared to the HDA capped QDs, and the marked asymmetry in the damping for the optically prepared and product states. However, the modulation patterns are again essentially in-phase between the two states, rather than antipahse, as expected for quantum beating. The time shift between the initial and final product modulation patterns is significantly longer than those observed in the HDA capped QDs.

Interestingly, the mid- to high-frequency modulations are observed to be dampened on the same time scale as the amine-capped QDs reported in Figures 4.3-4.6. However, the nonradiatuve relaxation of population from the $1P_e$ state to the $1S_e$ state is much slower (~250 fs). There also appears to be noticeable asymmetry in the modulations between the states. One possibility involves the contributions from strong ESA responses from the surface trap coordinates. This feature overlaps with a significant portion of the signals reported in the Figure 4.7.

In the current study, these differences are not fully understood. However, we hypothesize that the differences in modulation depth and time shift may arise due to the strength of the coupling strength and/or the differences in the extent of ligand coverage. In larger CdSe QDs, the geometric restrictions are lessened due to the larger surface area. This would allow, theoretically,

for greater surface passivation. As shown above, amine capped QDs exhibited deeper modulations when compared to the oleate capped QDs. This may be a result of a stronger coupling between the core electronic states and the NH_2 vibrational modes at the surface. The stronger coupling is also supported by the increased rate of relaxation observed in the amine capped 6.0 nm QDs compared to the oleate capped particles. This finding provides additional insight to the effect of vibronic coherences on the hot carrier cooling process in semiconductor QDs.

4.4 Conclusions

In this chapter, we employed broadband 2DES on CdSe QDs to determine the hot carrier cooling process at short time. Differently sized particles were studied, as well as different ligand compositions. The results provide the first evidence of vibronic coherences present in the short time dynamics. More importantly, we demonstrate the ability to tune the rate of relaxation of the hot carrier by simply replacing the ligand composition. Amine-based ligands exhibit stronger coupling to the core electronic states, as evident by deeper modulations and faster relaxation rates.

The phase relationship of the modulation pattern between donor and acceptor states ($1P_e$ and $1S_e$, respectively) supports the notion for a nonadiabatic energy transfer mechanism, unlike the antiphase relationship observed in quantum beating between the states. Additionally, the damping rate of the modulations appear on the order of the rate of relaxation from donor to acceptor. This further confirms the involvement of the vibronic coherence in population transfer.

Future studies involving ligands containing various functional groups and bonding character will help determine the conditions required to tune the strength of the coupling. Additional studies might also determine the extent of surface passivation and its effect on the

relaxation dynamics. A deeper understanding of the vibronic coherences observed here can lead to the development of highly efficient photovoltaic devices and improved photocatalysis applications.

4.5 Future Quantum Dot Work

In this chapter, we reported the first evidence to support the involvement of vibronic coherences in the nonradiative relaxation of hot carriers in semiconductor QDs. The vibronic coherences observed arise from wavefunction mixing of the core electronic states of the nanocrystal with the vibrational states of the organic capping ligands at the surface. We observed significant changes in the rate of relaxation by simply changing the ligands at the surface of the QD.

Future experiments have been planned for this project. Studies will now be focused on determining the coupling strength as a function of the ligand functional groups. The effect of the bonding character, the phase of the crystal structure, and the size of the materials will also be considered. A deeper understanding of the underlying nature of vibronic coherences in semiconductor QDs can lead to significant advancements in applications involving photovoltaic devices and photocatalysis.

APPENDIX

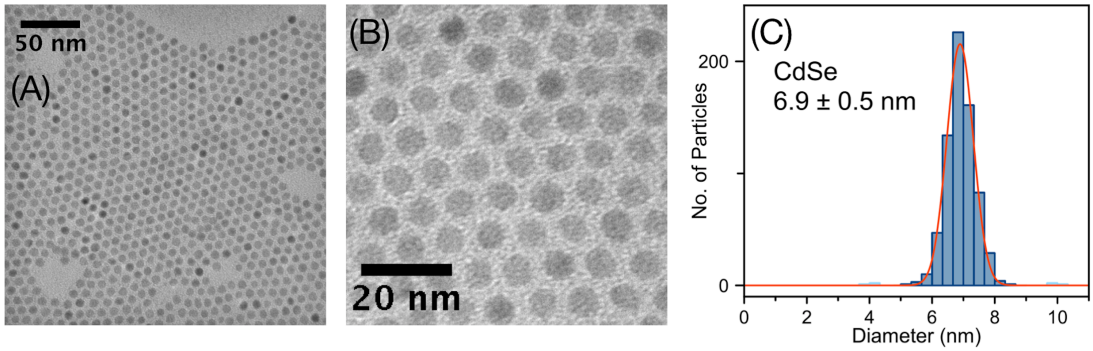

Figure A4.1. (a) TEM and (b) zoomed TEM image of the 6.9 nm CdSe QDs, illustrating a lack of stacking faults and uniform shapes. (c) size distribution histogram, showing high size monodispersity (± 5 nm).

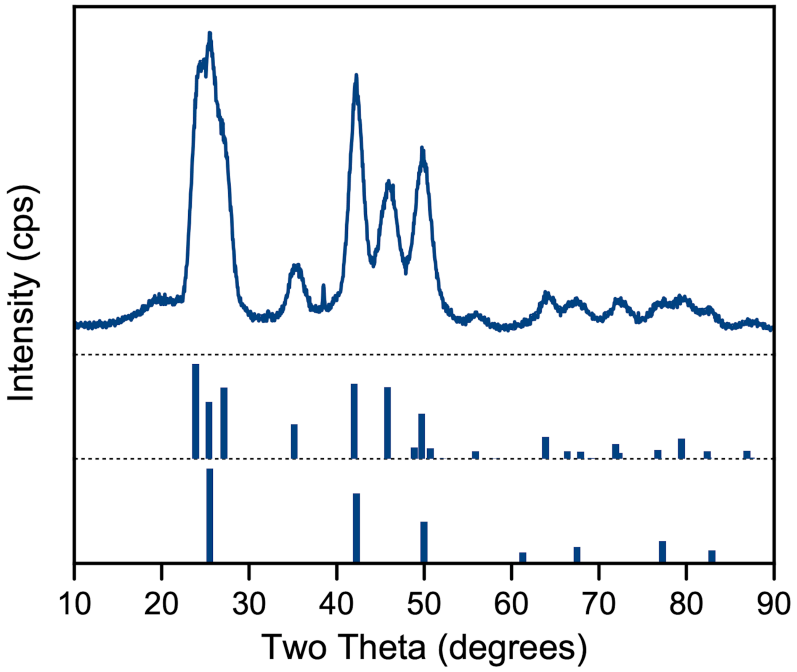

Figure A4.2. Powder X-ray diffraction pattern for 6.9 nm CdSe QDs (*top*) compared with calculated patterns for hexagonal, wurtzite phase (*middle*), and cubic, zincblende phase (*bottom*).

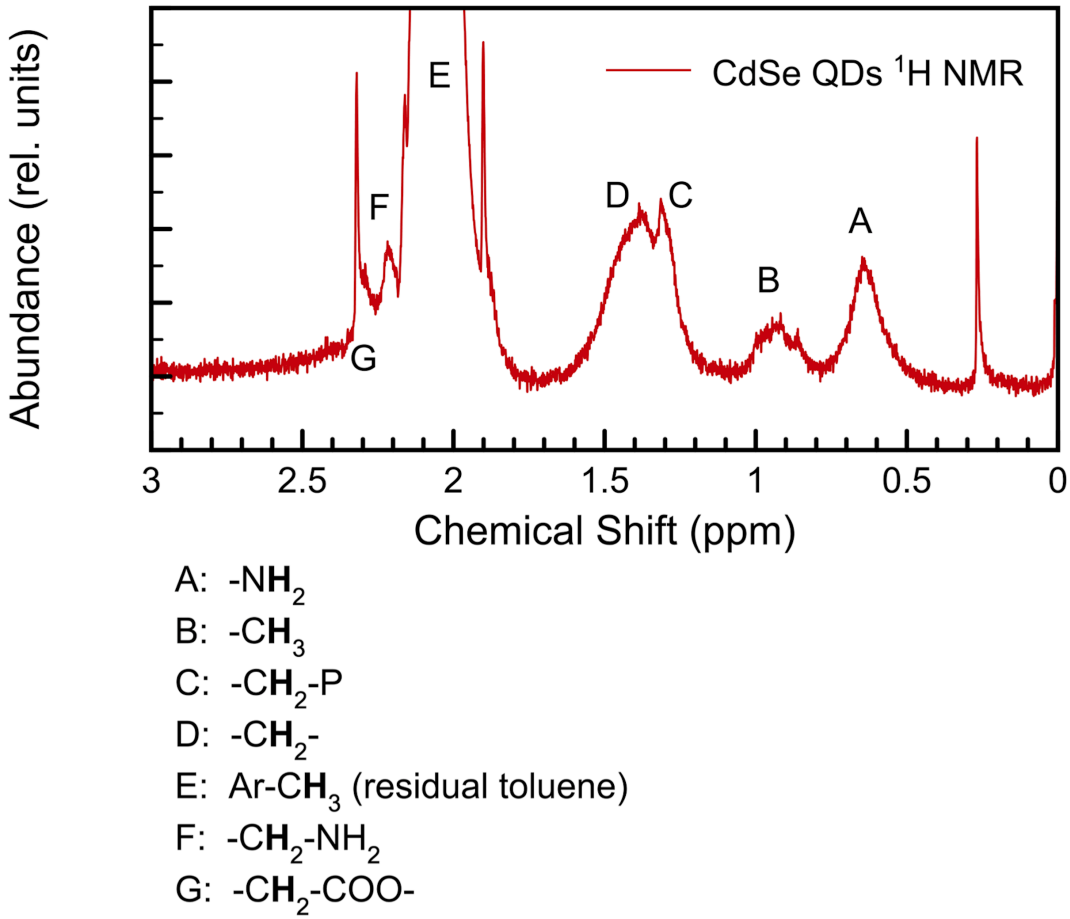

Figure A4.3. Proton NMR spectrum of CdSe QDs, exhibiting ligand composition following synthesis.

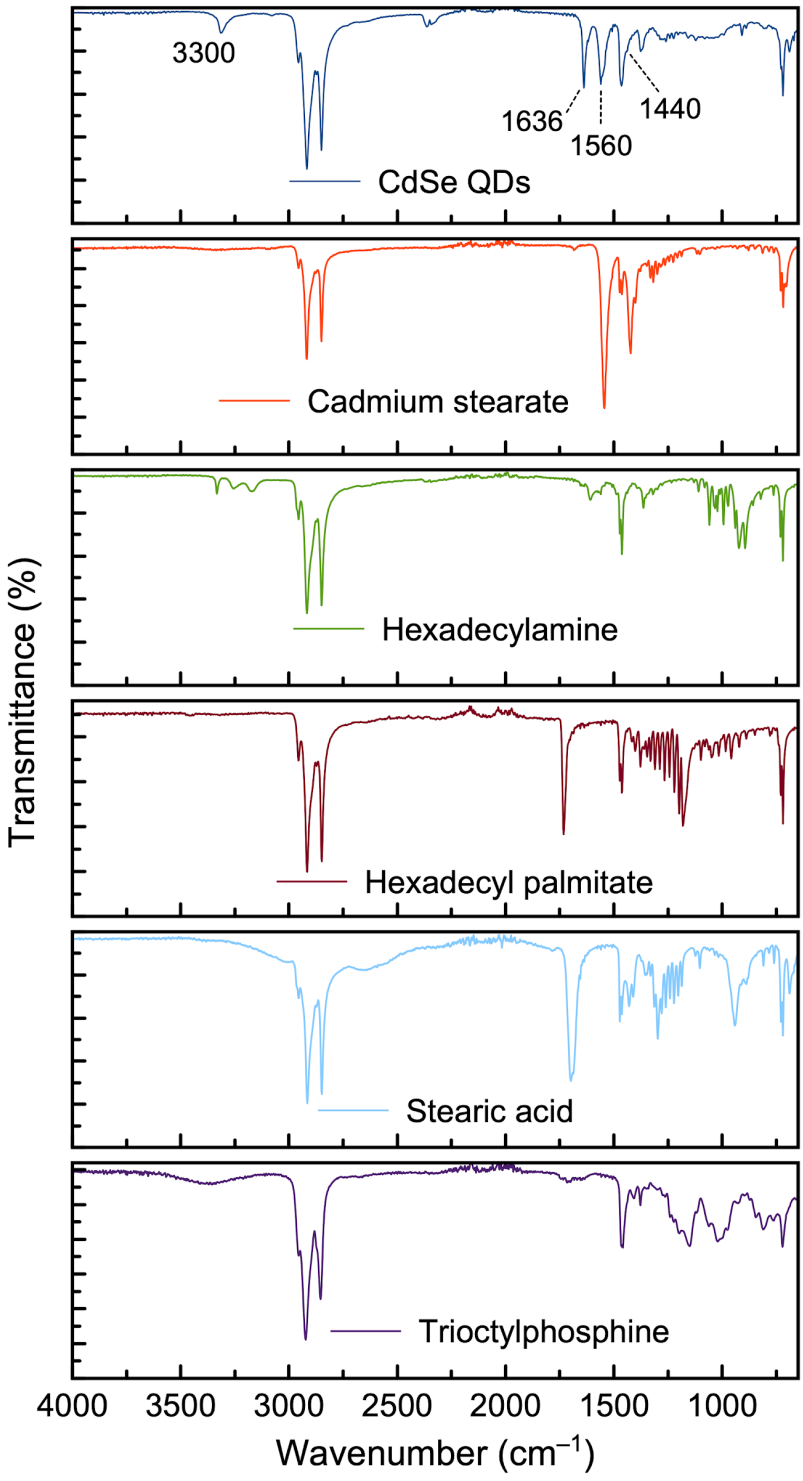

Figure A4.4. FTIR spectra of CdSe QDs (*top*) following synthesis. Below are comparison spectra confirming ligand composition.

REFERENCES

REFERENCES

(1) Brus, L. E. A Simple Model for the Ionization Potential, Electron Affinity, and Aqueous Redox Potentials of Small Semiconductor Crystallites. *J. Chem. Phys.* **1983**, *79* (11), 5566–5571.

(2) Brus, L. Quantum Crystallites and Nonlinear Optics. *Appl. Phys. A: Mater. Sci. Process.* **1991**, *53* (6), 465–474.

(3) Alivisatos, A. P. Semiconductor Clusters, Nanocrystals, and Quantum Dots. *Science* **1996**, *271* (5251), 933–937.

(4) Efros, A. L.; Rosen, M. The Electronic Structure of Semiconductor Nanocrystals. *Annu. Rev. Mater. Sci.* **2000**, *30* (1), 475–521.

(5) Owen, J.; Brus, L. Chemical Synthesis and Luminescence Applications of Colloidal Semiconductor Quantum Dots. *J. Am. Chem. Soc.* **2017**, *139* (32), 10939–10943.

(6) Klimov, V. I.; Mikhailovsky, A. A.; Xu, S.; Malko, A.; Hollingsworth, J. A.; Leatherdale, C. A.; Eisler, H.; Bawendi, M. G. Optical Gain and Stimulated Emission in Nanocrystal Quantum Dots. *Science* **2000**, *290* (5490), 314–317.

(7) Bimberg, D.; Grundmann, M.; Heinrichsdorff, F.; Ledentsov, N. N.; Ustinov, V. M.; Zhukov, A. E.; Kovsh, A. R.; Maximov, M. V.; Shernyakov, Y. M.; Volovik, B. V.; Tsatsul'nikov, A. F.; Kop'ev, P. S.; Alferov, Z. I. Quantum Dot Lasers: Breakthrough in Optoelectronics. *Thin Solid Films* **2000**, *367* (1), 235–249.

(8) García-Santamaría, F.; Chen, Y.; Vela, J.; Schaller, R. D.; Hollingsworth, J. A.; Klimov, V. I. Suppressed Auger Recombination in "Giant" Nanocrystals Boosts Optical Gain Performance. *Nano Lett.* **2009**, *9* (10), 3482–3488.

(9) Kambhampati, P. Unraveling the Structure and Dynamics of Excitons in Semiconductor Quantum Dots. *Acc. Chem. Res.* **2011**, *44* (1), 1–13.

(10) Fan, F.; Voznyy, O.; Sabatini, R. P.; Bicanic, K. T.; Adachi, M. M.; McBride, J. R.; Reid, K. R.; Park, Y. S.; Li, X.; Jain, A.; Quintero-Bermudez, R.; Saravanapavanantham, M.; Liu, M.; Korkusinski, M.; Hawrylak, P.; Klimov, V. I.; Rosenthal, S. J.; Hoogland, S.; Sargent, E. H. Continuous-Wave Lasing in Colloidal Quantum Dot Solids Enabled by Facet-Selective Epitaxy. *Nature* **2017**. https://doi.org/10.1038/nature21424.

(11) Weiss, E. A. Designing the Surfaces of Semiconductor Quantum Dots for Colloidal Photocatalysis. *ACS Energy Lett.* **2017**, *2* (5), 1005–1013.

(12) Bloom, B. P.; Liu, R.; Zhang, P.; Ghosh, S.; Naaman, R.; Beratan, D. N.; Waldeck, D. H. Directing Charge Transfer in Quantum Dot Assemblies. *Acc. Chem. Res.* **2018**, *51* (10), 2565–2573.

(13) Beard, M. C.; Johnson, J. C.; Luther, J. M.; Nozik, A. J. Multiple Exciton Generation in Quantum Dots versus Singlet Fission in Molecular Chromophores for Solar Photon Conversion. *Philos. Trans. A Math. Phys. Eng. Sci.* **2015**, *373* (2044). https://doi.org/10.1098/rsta.2014.0412.

(14) Wang, L.-W.; Califano, M.; Zunger, A.; Franceschetti, A. Pseudopotential Theory of Auger Processes in CdSe Quantum Dots. *Phys. Rev. Lett.* **2003**, *91* (5), 056404.

(15) Klimov, V. I., VI; Mikhailovsky, A. A.; McBranch, D. W.; Leatherdale, C. A.; Bawendi, M. G. Quantization of Multiparticle Auger Rates in Semiconductor Quantum Dots. *Science* **2000**, *287* (5455), 1011–1013.

(16) Ellingson, R. J.; Beard, M. C.; Johnson, J. C.; Yu, P.; Micic, O. I.; Nozik, A. J.; Shabaev, A.; Efros, A. L. Highly Efficient Multiple Exciton Generation in Colloidal PbSe and PbS Quantum Dots. *Nano Lett.* **2005**, *5* (5), 865–871.

(17) Beard, M. C.; Midgett, A. G.; Law, M.; Semonin, O. E.; Ellingson, R. J.; Nozik, A. J. Variations in the Quantum Efficiency of Multiple Exciton Generation for a Series of Chemically Treated PbSe Nanocrystal Films. *Nano Lett.* **2009**, *9* (2), 836–845.

(18) Beard, M. C. Multiple Exciton Generation in Semiconductor Quantum Dots. *J. Phys. Chem. Lett.* **2011**, *2* (11), 1282–1288.

(19) Bradshaw, L. R.; Knowles, K. E.; McDowall, S.; Gamelin, D. R. Nanocrystals for Luminescent Solar Concentrators. *Nano Lett.* **2015**, *15* (2), 1315–1323.

(20) Peterson, M. D.; Cass, L. C.; Harris, R. D.; Edme, K.; Sung, K.; Weiss, E. A. The Role of Ligands in Determining the Exciton Relaxation Dynamics in Semiconductor Quantum Dots. *Annu. Rev. Phys. Chem.* **2014**, *65*, 317–339.

(21) Lifshitz, E. Evidence in Support of Exciton to Ligand Vibrational Coupling in Colloidal Quantum Dots. *J. Phys. Chem. Lett.* **2015**, *6* (21), 4336–4347.

(22) Guyot-Sionnest, P.; Shim, M.; Matranga, C.; Hines, M. Intraband Relaxation in CdSe Quantum Dots. *Phys. Rev. B Condens. Matter* **1999**, *60* (4), R2181–R2184.

(23) Guyot-Sionnest, P.; Wehrenberg, B.; Yu, D. Intraband Relaxation in CdSe Nanocrystals and the Strong Influence of the Surface Ligands. *J. Chem. Phys.* **2005**, *123* (7), 074709.

(24) Pandey, A.; Guyot-Sionnest, P. Slow Electron Cooling in Colloidal Quantum Dots. *Science* **2008**, *322* (5903), 929–932.

(25) Wu, D.; Kordesch, M. E.; Van Patten, P. G. A New Class of Capping Ligands for CdSe Nanocrystal Synthesis. *Chem. Mater.* **2005**, *17* (25), 6436–6441.

(26) Jasieniak, J.; Bullen, C.; van Embden, J.; Mulvaney, P. Phosphine-Free Synthesis of CdSe Nanocrystals. *J. Phys. Chem. B* **2005**, *109* (44), 20665–20668.

(27) Chen, O.; Chen, X.; Yang, Y.; Lynch, J.; Wu, H.; Zhuang, J.; Cao, Y. C. Synthesis of Metal-Selenide Nanocrystals Using Selenium Dioxide as the Selenium Precursor. *Angew. Chem. Int. Ed.* **2008**, *47* (45), 8638–8641.

(28) Katari, J. E. B.; Colvin, V. L.; Alivisatos, A. P. X-Ray Photoelectron Spectroscopy of CdSe Nanocrystals with Applications to Studies of the Nanocrystal Surface. *J. Phys. Chem.* **1994**, *98* (15), 4109–4117.

(29) Yu, W. W.; Qu, L.; Guo, W.; Peng, X. Experimental Determination of the Extinction Coefficient of CdTe, CdSe, and CdS Nanocrystals. *Chem. Mater.* **2003**. https://doi.org/10.1021/cm034081k.

(30) Wang, Q.; Seo, D.-K. Synthesis of Deep-Red-Emitting CdSe Quantum Dots and General Non-Inverse-Square Behavior of Quantum Confinement in CdSe Quantum Dots. *Chem. Mater.* **2006**, *18* (24), 5764–5767.

(31) Mekis, I.; Talapin, D. V.; Kornowski, A.; Haase, M.; Weller, H. One-Pot Synthesis of Highly Luminescent CdSe/CdS Core- Shell Nanocrystals via Organometallic and "Greener" Chemical Approaches. *J. Phys. Chem. B* **2003**, *107* (30), 7454–7462.

(32) Huxter, V. M.; Kim, J.; Lo, S. S.; Lee, A.; Nair, P. S.; Scholes, G. D. Spin Relaxation in Zinc Blende and Wurtzite CdSe Quantum Dots. *Chem. Phys. Lett.* **2010**, *491* (4), 187–192.

(33) Wong, C. Y.; Scholes, G. D. Using Two-Dimensional Photon Echo Spectroscopy to Probe the Fine Structure of the Ground State Biexciton of CdSe Nanocrystals. *J. Lumin.* **2011**, *131* (3), 366–374.

(34) Wong, C. Y.; Scholes, G. D. Biexcitonic Fine Structure of CdSe Nanocrystals Probed by Polarization-Dependent Two-Dimensional Photon Echo Spectroscopy. *J. Phys. Chem. A* **2011**, *115* (16), 3797–3806.

(35) Caram, J. R.; Zheng, H.; Dahlberg, P. D.; Rolczynski, B. S.; Griffin, G. B.; Fidler, A. F.; Dolzhnikov, D. S.; Talapin, D. V.; Engel, G. S. Persistent Inter-Excitonic Quantum Coherence in CdSe Quantum Dots. *J. Phys. Chem. Lett.* **2014**, *5* (1), 196–204.

(36) Caram, J. R.; Zheng, H.; Dahlberg, P. D.; Rolczynski, B. S.; Griffin, G. B.; Dolzhnikov, D. S.; Talapin, D. V.; Engel, G. S. Exploring Size and State Dynamics in CdSe Quantum Dots Using Two-Dimensional Electronic Spectroscopy. *J. Chem. Phys.* **2014**, *140* (8), 084701.

(37) Jonas, D. M. Two-Dimensional Femtosecond Spectroscopy. *Annu. Rev. Phys. Chem.* **2003**, *54*, 425–463.

(38) Grumstrup, E. M.; Shim, S.-H.; Montgomery, M. A.; Damrauer, D. H.; Zanni, M. T. Facile Collection of Two-Dimensional Electronic Spectra Using Femtosecond Pulse-Shaping Technology. *Opt. Express* **2007**, *15*, 16681–16689.

(39) Shim, S. H.; Zanni, M. T. How to Turn Your Pump-Probe Instrument into a Multidimensional Spectrometer: 2D IR and Vis Spectroscopies via Pulse Shaping. *Phys. Chem. Chem. Phys.* **2009**, *11* (5), 748–761.

(40) Myers, J. A.; Lewis, K. L.; Tekavec, P. F.; Ogilvie, J. P. Two-Color Two-Dimensional Fourier Transform Electronic Spectroscopy with a Pulse-Shaper. *Opt. Express* **2008**, *16* (22), 17420.

(41) Tekavec, P. F.; Myers, J. A.; Lewis, K. L. M.; Ogilvie, J. P. Two-Dimensional Electronic Spectroscopy with a Continuum Probe. *Opt. Lett.* **2009**, *34*, 1390–1392.

(42) Lozovoy, V. V.; Pastirk, I.; Dantus, M. Multiphoton Intrapulse Interference 4: Characterization and Compensation of the Spectral Phase of Ultrashort Laser Pulses. *Opt. Lett.* **2004**, *29*, 775–777.

(43) Augulis, R.; Zigmantas, D. Two-Dimensional Electronic Spectroscopy with Double Modulation Lock-in Detection: Enhancement of Sensitivity and Noise Resistance. *Opt. Express* **2011**, *19* (14), 13126–13133.

(44) Veamatahau, A.; Jiang, B.; Seifert, T.; Makuta, S.; Latham, K.; Kanehara, M.; Teranishi, T.; Tachibana, Y. Origin of Surface Trap States in CdS Quantum Dots: Relationship between Size Dependent Photoluminescence and Sulfur Vacancy Trap States. *Phys. Chem. Chem. Phys.* **2015**, *17* (4), 2850–2858.

(45) Houtepen, A. J.; Hens, Z.; Owen, J. S.; Infante, I. On the Origin of Surface Traps in Colloidal II–VI Semiconductor Nanocrystals. *Chem. Mater.* **2017**, *29* (2), 752–761.

(46) Empedocles, S. A.; Bawendi, M. G. Quantum-Confined Stark Effect in Single CdSe Nanocrystallite Quantum Dots. *Science* **1997**, *278* (5346), 2114–2117.

(47) Pokutnyi, S. I.; Jacak, L.; Misiewicz, J.; Salejda, W.; Zegrya, G. G. Stark Effect in Semiconductor Quantum Dots. *J. Appl. Phys.* **2004**, *96* (2), 1115–1119.

(48) Hönig, G.; Callsen, G.; Schliwa, A.; Kalinowski, S.; Kindel, C.; Kako, S.; Arakawa, Y.; Bimberg, D.; Hoffmann, A. Manifestation of Unconventional Biexciton States in Quantum Dots. *Nat. Commun.* **2014**, *5*, 5721.

(49) Seiler, H.; Palato, S.; Kambhampati, P. Investigating Exciton Structure and Dynamics in Colloidal CdSe Quantum Dots with Two-Dimensional Electronic Spectroscopy. *J. Chem. Phys.* **2018**, *149* (7), 074702.

(50) Krčmář, J.; Gelin, M. F.; Domcke, W. Simulation of Femtosecond Two-Dimensional Electronic Spectra of Conical Intersections. *J. Chem. Phys.* **2015**, *143*, 074308.

(51) Turner, D. B.; Dinshaw, R.; Lee, K. K.; Belsley, M. S.; Wilk, K. E.; Curmi, P. M.; Scholes, G. D. Quantitative Investigations of Quantum Coherence for a Light-Harvesting Protein at Conditions Simulating Photosynthesis. *Phys. Chem. Chem. Phys.* **2012**, *14*, 4857–4874.

(52) Cooper, J. K.; Franco, A. M.; Gul, S.; Corrado, C.; Zhang, J. Z. Characterization of Primary Amine Capped CdSe, ZnSe, and ZnS Quantum Dots by FT-IR: Determination of Surface Bonding Interaction and Identification of Selective Desorption. *Langmuir* **2011**. https://doi.org/10.1021/la201273x.

(53) Klimov, V. I.; McBranch, D. W.; Leatherdale, C. A.; Bawendi, M. G. Electron and Hole Relaxation Pathways in Semiconductor Quantum Dots. *Phys. Rev. B Condens. Matter* **1999**, *60* (19), 13740–13749.

(54) Klimov, V. I.; Mikhailovsky, A. A.; McBranch, D. W.; Leatherdale, C. A.; Bawendi, M. G. Mechanisms for Intraband Energy Relaxation in Semiconductor Quantum Dots: The Role of Electron-Hole Interactions. *Phys. Rev. B Condens. Matter* **2000**, *61* (20), R13349–R13352.

(55) Xu, S.; Mikhailovsky, A. A.; Hollingsworth, J. A.; Klimov, V. I. Hole Intraband Relaxation in Strongly Confined Quantum Dots: Revisiting the ``phonon Bottleneck'' Problem. *Phys. Rev. B Condens. Matter* **2002**, *65* (4), 045319.

(56) Levine, B. G.; Martínez, T. J. Isomerization through Conical Intersections. *Annu. Rev. Phys. Chem.* **2007**, *58*, 613–634.

(57) Kambhampati, P. Hot Exciton Relaxation Dynamics in Semiconductor Quantum Dots: Radiationless Transitions on the Nanoscale. *J. Phys. Chem. C* **2011**, *115* (45), 22089–22109.

(58) Sewall, S. L.; Cooney, R. R.; Dias, E. A.; Tyagi, P.; Kambhampati, P. State-Resolved Observation in Real Time of the Structural Dynamics of Multiexcitons in Semiconductor Nanocrystals. *Phys. Rev. B Condens. Matter* **2011**, *84* (23), 235304.

(59) Klimov, V. I.; McBranch, D. W. Femtosecond P-to- S Electron Relaxation in Strongly Confined Semiconductor Nanocrystals. *Phys. Rev. Lett.* **1998**, *80* (18), 4028–4031.

Chapter 5: Preliminary Work: Excitation Energy Transfer in Intact Phycobilisomes

In this dissertation, mechanisms and pathways of excitation energy transfer (EET) and nonradiative relaxation in light harvesting proteins and quantum dots were investigated using femtosecond broadband two-dimensional electronic spectroscopy (2DES). In particular, 2DES experiments were employed to identify vibronic coherences and nonadiabatic energy transfer in the peridinin–chlorophyll protein (PCP) and colloidal CdSe QDs.

In previous studies of PCP,[1–4] the role of quantum coherence was studied using 2DES and transient grating experiments. Here, we performed 2DES experiments with a different window of observation, primarily photoselecting the peridinin donor states and the vibrational states of the acceptor chlorophylls (Chls). We identify vibrationally impulsive and phase amplitude modulations of the Chl acceptor cross peak in both wild-type PCP containing Chl *a* (wtPCP–Chl *a*) and reconstituted PCP with Chl *b* (rPCP–Chl *b*). These findings support a nonadiabatic mechanism, where the vibrational phase coherence is retained in the product Chl exciton as it crosses a conical intersection (CI). The information obtained from these experiments provide an understanding of the structure and design necessary for efficient and rapid EET.

The findings reported here provide inspiration to extend 2DES studies to identify vibronic coherences in other light harvesting systems, such as phycobilisomes (PBS), and potential photovoltaic materials, such as semiconductor QDs.

Previous studies[5,6] on colloidal QDs have identified potential surface state contributions to the core electronic dynamics of the nanocrystals. In particular, many studies[6–8] suggested the role of organic surface ligands in the nonradiative relaxation of hot carriers may have been overlooked. Future work will focus on the nature of vibronic coherences in both semiconductor materials as well as light harvesting systems, as featured below.

5.1 Extending the coherent excitation energy transfer studies to intact phycobilisomes

In an effort to further understand the role of structure in efficient EET in nature, studies have started on intact phycobilisomes (PBS). While these studies are not a main feature of this dissertation, they represent the future direction of the work mentioned in this dissertation.

Phycobilisomes (PBS) are the hemidiscoid water-soluble phycobiliprotein complexes (Figure 5.1) and serve as the peripheral light harvesting antenna for photosystem I (PSI) and photosystem II (PSII) in cyanobacteria and red algae.[9–18] The PBS is composed of rods and core, with stacks of disk-shaped phycobiliprotein complexes held together by linker polypeptides (Figure 5.2).[19–21] PBS are known to exhibit a funnel-shaped energy landscape; in cyanobacteria, the absorption and emission spectra of the bilin (linear tetrapyrrole) chromophores bound by phycoerythrin (PE) and C-phycocyanin (PC) in the rods are blue-shifted compared to those bound by allophycocyanin (APC) in the core, which promotes a downhill flow of excitation energy from the rods to the core.[10,15,22]

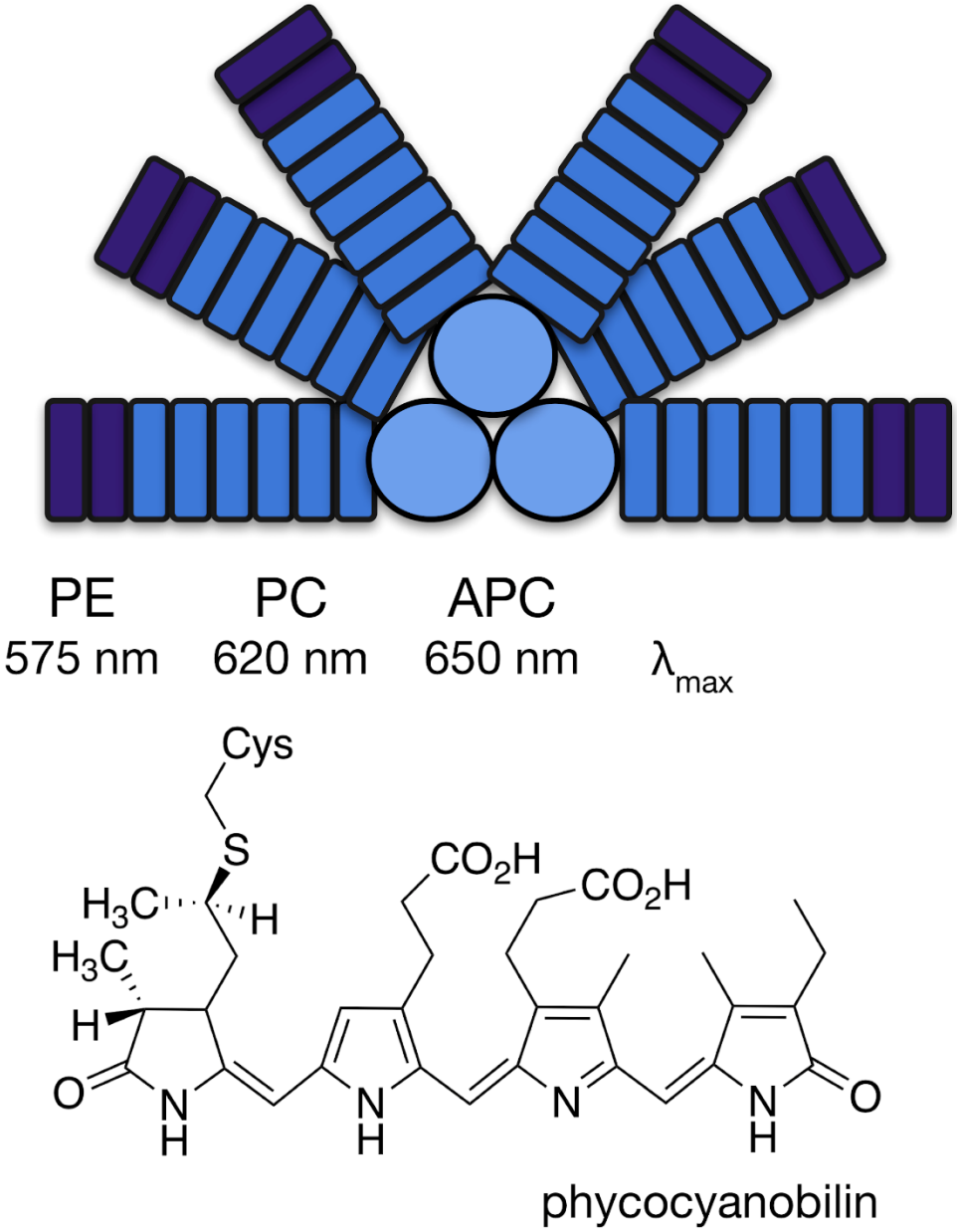

Figure 5.1. *Top:* structure of the phycobilisome from *Fremyella diplosiphon*, with the absorption maxima in the rods and core of phycoerythrin (PE), C-phycocyanin (PC), and allophycocyanin (APC).[10,12,13,23] *Bottom:* extended conformation of phycocyanobilin, as bound by PC and APC via thioether linkages to cysteine residues.[13,14]

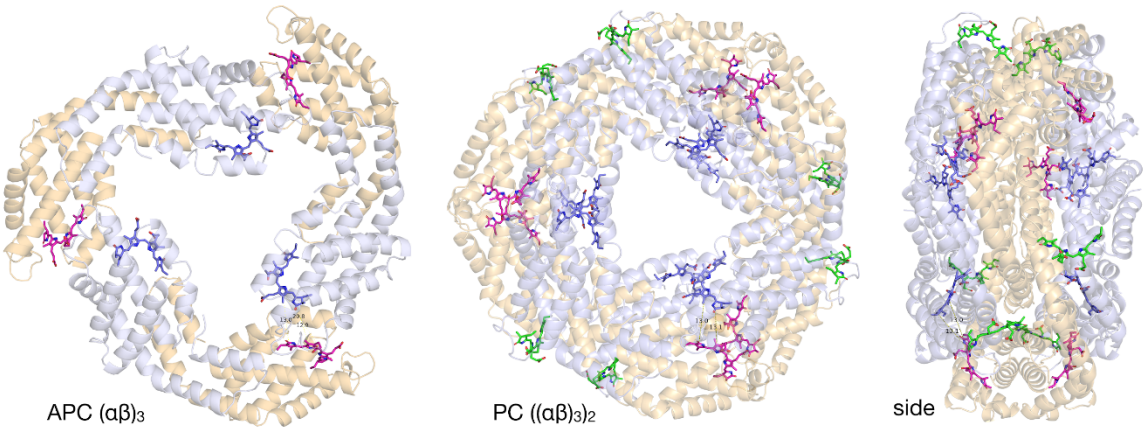

Figure 5.2. Crystal structures of allophycocyanin (APC) $(\alpha\beta)_3$ trimers from *Spirulina platensis* (1ALL)[24] and of C-phycocyanin (PC) $((\alpha\beta)_3)_2$ hexamers from *Fremyella diplosiphon* (1CPC).[25] The α (light orange) and β subunits (grey) protein subunits are rendered as transparent ribbons. The α84 (magenta), β84 (blue), and β155 (green) phycocyanobilin chromophores are rendered as stick figures. Closest and center-to-center distance measurements are shown for one of the α84–β84 pairs in each, that of the front $(\alpha\beta)_3$ trimer for the PC structure.

5.1.1 Energy Transfer in Phycobilisomes

Previous studies employed picosecond fluorescence and pump–probe spectroscopy work, identifying excitation energy transfer between the chromophores in the PC and APC disks other than the α84–β84 pair can be described by the Förster mechanism.[26–32] However, work by the Beck's laboratory demonstrated that the α84–β84 pair in APC is collectively excited upon absorption of a photon, producing a set of exciton states in the intermediate to strong electronic coupling limit.[32–37] This conclusion was subsequently supported by observation of collective excitations of the α84–β84 pairs in single-molecule fluorescence experiments[38] and then by heterodyne transient grating spectroscopy and 2DES experiments.[39,40] The latter discuss a vibronic exciton picture, in which the electronic coupling is enhanced in the α84–β84 pair in APC trimers by matching of the exciton state energy gap with the 800 cm^{-1} HOOP deformation mode of the bilin chromophores.[39,40] The vibronic exciton picture has been thoroughly discussed in this dissertation, and serves as inspiration for these future works.

The proposed future work focuses on studies of intact phycobilisomes. Only a few studies to date have measured the excitation energy transfer in intact phycobilisomes. Recent studies involving picosecond fluorescence measurements in whole cells[41] and in isolated, intact phycobilisomes from *Synechococcus* PCC 6803[42] EET in PC down the rods with time constants of 6–9 ps, but notably this is about the same as their instrument response time. Transfer of excitation from PC to APC660 is much slower, at 40 ps, and transfer from APC660 to APC680 is even slower, at 120 ps.[41,42] Recent femtosecond pump-probe spectroscopy work on intact phycobilisomes from *Thermosynechococcus vulcanus*, however, identified sub-ps energy transfer front hge rods to the core via a coherent energy transfer mechanism.[43] In order for this to be possible, the distances between the bilins along the rods must be fairly short. Single-particle EM and cryo-EM structures of the intact phycobilisome from cyanobacteria[44] and red algae,[45] respectively, may support this suggestion. The red algal cryo-EM structure is of relatively high resolution (3.5 Å). It indicates fairly close spacings between the α84 and β84 chromophores in adjacent hexamers in the rods (two interactions are 12.7 and 16.1 Å, with most in the 20 Å range center to center),[45] which is notably somewhat closer together than in the trimers themselves. These estimates suggest the possibility of intermediate to strong electronic couplings and collective excitations down the rods of the phycobilisome.

5.1.2 Preliminary Results

We have applied broadband 2DES methods for the first time to our knowledge to characterize the excitation energy transfer pathways and mechanisms in intact phycobilisomes. The preliminary results contain evidence of long-range collective excitations over the length of rods, extending to the core of the phycobilisomes from *Fremyella diplosiphon* and *Synechocystis* PCC 6803. There is a distinct rate bottleneck for energy transfer in the core, which would allows

photoregulatory mechanisms to operate there with sensitivity. These results support the presence of long range collective excitations along the entire pathways taken by an excitation from the rods to the core. However, fast recovery of the originally excited ground state is not observed in isolated phycobiliproteins. The nature of the excitation energy transfer in the core of the PBS is clearly much slower, suggesting that polarons produced by the coherent EET process do not employ coherent mechanisms to move excitation in the core from APC660 to APC680.

5.1.3 Excitation energy transfer

Figure 5.3 shows a series of broadband 2DES spectra acquired from intact PBS from *Fremyella diplosiphon*. These PBS incorporate a disk of PE at the end of the rods, producing a peak absorption in the 570 nm range. The 2DES experiment was performed with 6.5 fs pulses, with bandwidth spanning from 520 nm in the PE region absorption spectrum up to the 680 nm emission of the terminal emitters.

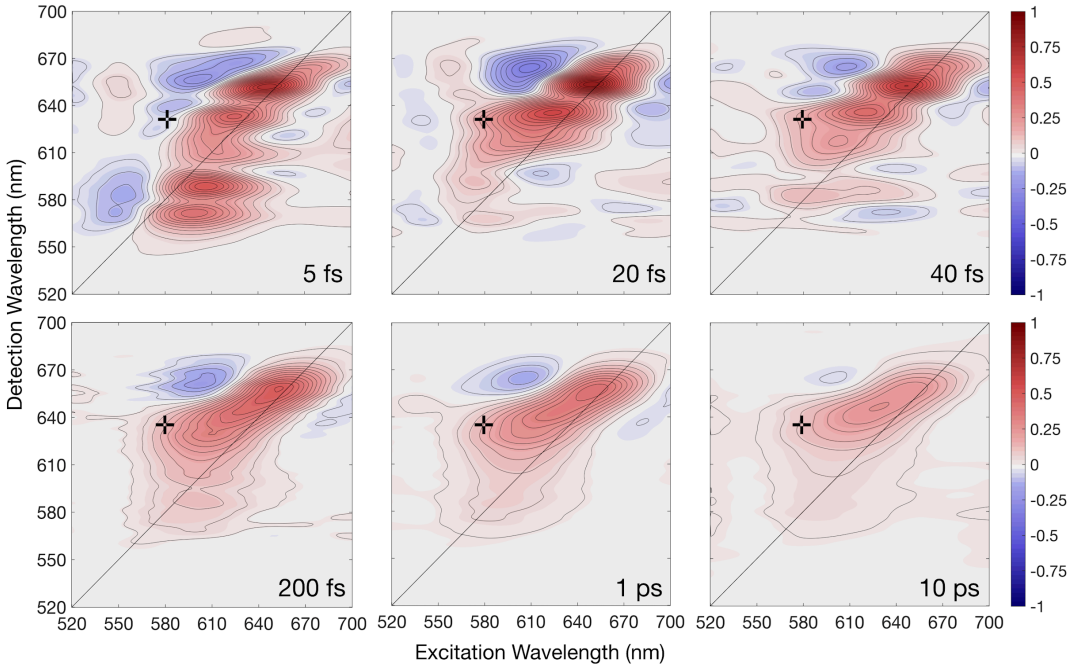

Figure 5.3. Phased absorptive 2DES spectra from *Fremyella diplosiphon* following excitation by 6.5 fs pulses (520 nm to 700 nm).

At short waiting times, <10 fs, a principally diagonal 2DES spectrum is observed, with ground-state bleaching (GSB) and stimulated emission (SE) signals from partially resolved features arising from direct excitation of bilins in PE (two pigment groups) from those of PC in the rods; further, signals from excitations of APC660 are partially resolved from those in APC680. Above the diagonal, relatively strong excited-state absorption (ESA) signals are observed, assigned to transitions to doubly excited exciton states, lasting only for ~20 fs, the timescale for the fastest downhill energy transfer processes. On a similar timescale there is evident decay of signal from the well resolved off-diagonal cross peaks of net GSB and SE character that link excitations in the 550–580 nm range with detection in the 640–670 nm range. These features provide direct evidence for the initial presence and decay of quantum coherence between bilins in PE and PC in the rods and those in APC in the core.

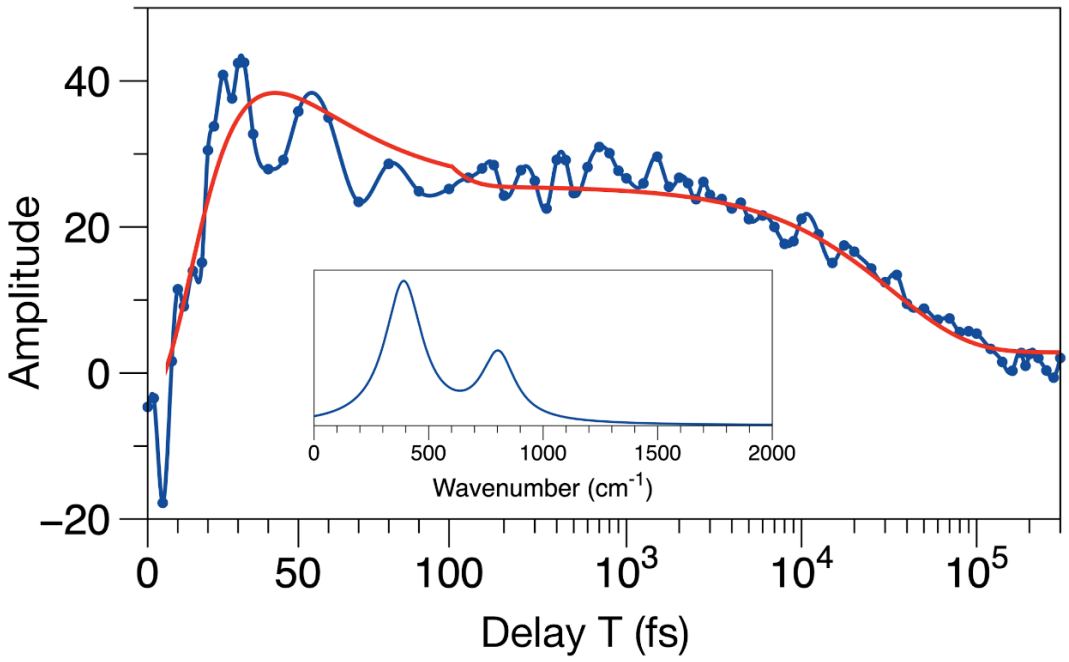

Figure 5.4. Phased amplitude of the 2DES spectrum measured at the cross-peak marker in Figure 5.3, at λ_{ex} = 580 nm and λ_{det} = 640 nm. The model curve (red, with convolution with the instrument function) includes a 24 fs rise and 25 fs and 33 ps decay components. The response is plotted as a function of a semilogarithmic axis split at 100 fs. The inset shows a LPSVD model to the <100 fs quantum beating.

Downhill excitation transfer in these PBS is marked by ultrafast evolution of off-diagonal cross peaks. The initially diagonal PB and SE signal moves upwards to the >640 nm region of the detection axis in <20 fs, reporting the progression of excitation energy down the ends of the rods of the phycobilisome. At longer waiting time, the cross peaks continue to slide upwards to still longer wavelengths; the progress of the SE character above the marker (and the 25 fs decay of the signal amplitude in Figure 5.4) certainly reports further transfer of excitation from PC to APC660, the acceptor cylinder in the core. An interesting feature if the amplitude change over time is the clear modulation of the signal. The modulation pattern involves two frequencies, 390 and 800 cm^{-1}, with both components damped in 55 fs, significantly slower than the principal line broadening timescale. As in PCP, as discussed in previous chapters, we propose that this vibronic coherence and the recovery of GSB on the diagonal evidences polaron formation, the localization/self-trapping of excitons following coherent energy transfer.[46–48] These vibrational frequencies are preliminarily assigned to displaced torsional and HOOP coordinates[40] of the bilin chromophore in the acceptor exciton state.

At waiting times >50 fs, the 2DES spectra exhibit a broadened, tilted diagonal character that predominantly reflects stalling of excitation at the APC660 acceptor in the core. The GSB and SE signal above the diagonal then moves much more slowly (33 ps time constant) to still longer wavelengths over the several ps (Figure 5.5) to reach APC680, the terminal emitters. These kinetics are essentially consistent with previous work in the ps streak-camera experiments by van Amerongen and coworkers,[41,42] but the 2DES spectra makes it possible to correlate the arrival of excitation at the terminal emitters with the initial excitation of different species in the phycobilisome.

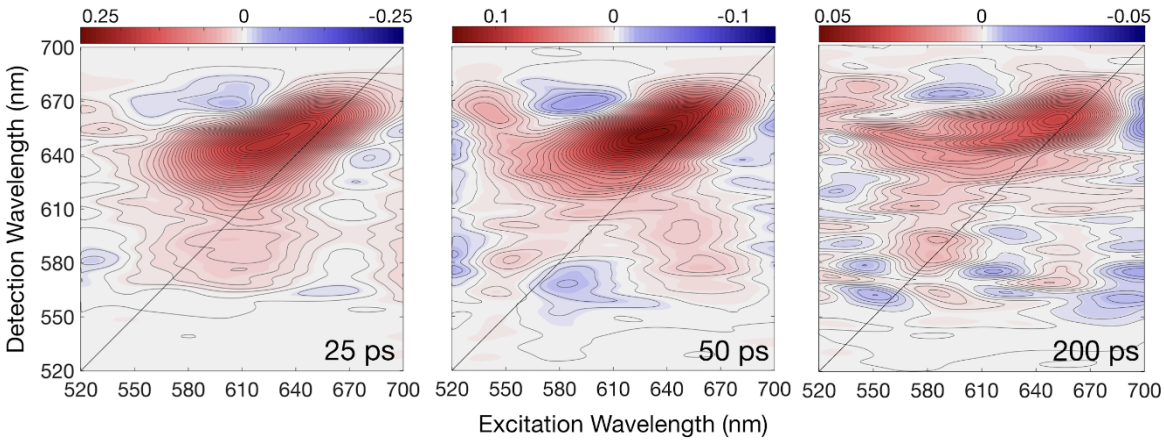

Figure 5.5. Phased absorptive 2DES spectra from *Fremyella diplosiphon* at long time delays following excitation by 6.5 fs pulses (520 nm to 700 nm). These spectra are autoscaled to the maximum signal amplitude on the diagonal.

The preliminary findings in the phycobilisome experiment represent an extension of the work reported in this dissertation. Future work on intact phycobilisomes will reveal more detail on the excitation energy transfer mechanisms employed in natural light harvesting complexes. These studies can influence the experiments involving semiconductor nanomaterials, in an effort to increase photovoltaic efficiencies.

5.3 Conclusions

In conclusion, we have applied femtosecond broadband 2DES on the peridinin–chlorophyll protein and semiconductor QDs. We report the first evidence for nonadiabatic energy transfer in PCP, and the first observation of vibronic coherences in semiconductor QDs involving the core electronic states and the ligand vibrational modes. These studies provide a deeper understanding of the mechanisms employed in natural photosynthetic systems, and identify similar phenomena in synthetic materials. We have extended the study to additional natural light harvesting systems, such as the phycobilisomes. Further research inspired by these works can improve the efficiency of devices in applications including photovoltaics, photocatalysis, and quantum information.

REFERENCES

REFERENCES

(1) Ghosh, S.; Bishop, M. M.; Roscioli, J. D.; LaFountain, A. M.; Frank, H. A.; Beck, W. F. Excitation Energy Transfer by Coherent and Incoherent Mechanisms in the Peridinin–chlorophyll *a* Protein. *J. Phys. Chem. Lett.* **2017**, *8*, 463–469.

(2) Roscioli, J. D.; Ghosh, S.; LaFountain, A. M.; Frank, H. A.; Beck, W. F. Quantum Coherent Excitation Energy Transfer by Carotenoids in Photosynthetic Light Harvesting. *J. Phys. Chem. Lett.* **2017**, *8*, 5141−5147.

(3) Roscioli, J. D.; Ghosh, S.; LaFountain, A. M.; Frank, H. A.; Beck, W. F. Structural Tuning of Quantum Decoherence and Coherent Energy Transfer in Photosynthetic Light Harvesting. *J. Phys. Chem. Lett.* **2018**, 5071–5077.

(4) Roscioli, J. D. Detection of Coherent Energy Transfer Pathways in Photosynthesis with Two-Dimensional Electronic Spectroscopy. Chemistry - Doctor of Philosophy, Michigan State University, 2018.

(5) Peterson, M. D.; Cass, L. C.; Harris, R. D.; Edme, K.; Sung, K.; Weiss, E. A. The Role of Ligands in Determining the Exciton Relaxation Dynamics in Semiconductor Quantum Dots. *Annu. Rev. Phys. Chem.* **2014**, *65*, 317–339.

(6) Lifshitz, E. Evidence in Support of Exciton to Ligand Vibrational Coupling in Colloidal Quantum Dots. *J. Phys. Chem. Lett.* **2015**, *6* (21), 4336–4347.

(7) Guyot-Sionnest, P.; Shim, M.; Matranga, C.; Hines, M. Intraband Relaxation in CdSe Quantum Dots. *Phys. Rev. B Condens. Matter* **1999**, *60* (4), R2181–R2184.

(8) Guyot-Sionnest, P.; Wehrenberg, B.; Yu, D. Intraband Relaxation in CdSe Nanocrystals and the Strong Influence of the Surface Ligands. *J. Chem. Phys.* **2005**, *123* (7), 074709.

(9) Gantt, E. Phycobilisomes: Light-Harvesting Pigment Complexes. *Bioscience* **1975**, *25* (12), 781–788.

(10) Bryant, D. A.; Guglielmi, G.; de Marsac, N. T.; Castets, A.-M.; Cohen-Bazire, G. The Structure of Cyanobacterial Phycobilisomes: A Model. *Arch. Microbiol.* **1979**, *123* (2), 113–127.

(11) Gantt, E. Phycobilisomes. *Annu. Rev. Plant Physiol.* **1981**, *32* (1), 327–347.

(12) Glazer, A. N. Phycobilisomes: Structure and Dynamics. *Annu. Rev. Microbiol.* **1982**, *36*, 173–198.

(13) Glazer, A. N. Phycobilisome a Macromolecular Complex Optimized for Light Energy Transfer. *Biochimica et Biophysica Acta (BBA) - Reviews on Bioenergetics* **1984**, *768* (1), 29–51.

(14) Glazer, A. N. Light Harvesting by Phycobilisomes. *Annu. Rev. Biophys. Biophys. Chem.* **1985**, *14*, 47–77.

(15) Adir, N. Elucidation of the Molecular Structures of Components of the Phycobilisome: Reconstructing a Giant. *Photosynth. Res.* **2005**, *85* (1), 15–32.

(16) Watanabe, M.; Ikeuchi, M. Phycobilisome: Architecture of a Light-Harvesting Supercomplex. *Photosynth. Res.* **2013**, *116* (2-3), 265–276.

(17) Watanabe, M.; Semchonok, D. A.; Webber-Birungi, M. T.; Ehira, S.; Kondo, K.; Narikawa, R.; Ohmori, M.; Boekema, E. J.; Ikeuchi, M. Attachment of Phycobilisomes in an Antenna–photosystem I Supercomplex of Cyanobacteria. *Proc. Natl. Acad. Sci. U. S. A.* **2014**, *111* (7), 2512–2517.

(18) Harris, D.; Bar-Zvi, S.; Lahav, A.; Goldshmid, I.; Adir, N. The Structural Basis for the Extraordinary Energy-Transfer Capabilities of the Phycobilisome. *Subcell. Biochem.* **2018**, *87*, 57–82.

(19) de Marsac, N. T. Phycobiliproteins and Phycobilisomes: The Early Observations. *Photosynth. Res.* **2003**, *76* (1-3), 193–205.

(20) Liu, L.-N.; Chen, X.-L.; Zhang, Y.-Z.; Zhou, B.-C. Characterization, Structure and Function of Linker Polypeptides in Phycobilisomes of Cyanobacteria and Red Algae: An Overview. *Biochim. Biophys. Acta* **2005**, *1708* (2), 133–142.

(21) David, L.; Marx, A.; Adir, N. High-Resolution Crystal Structures of Trimeric and Rod Phycocyanin. *J. Mol. Biol.* **2011**, *405* (1), 201–213.

(22) Grabowski, J.; Gantt, E. Excitation Energy Migration in Phycobilisomes: Comparison of Experimental Results and Theoretical Predictions. *Photochem. Photobiol.* **1978**, *28* (1), 47–54.

(23) Rosinski, J.; Hainfeld, J. F.; Rigbi, M.; Siegelman, H. W. Phycobilisome Ultrastructure and Chromatic Adaptation in *Fremyella Diplosiphon*. *Ann. Bot.* **1981**, *47* (1), 1–12.

(24) Brejc, K.; Ficner, R.; Huber, R.; Steinbacher, S. Isolation, Crystallization, Crystal Structure Analysis and Refinement of Allophycocyanin from the Cyanobacterium *Spirulina Platensis* at 2.3 A Resolution. *J. Mol. Biol.* **1995**, *249* (2), 424–440.

(25) Duerring, M.; Schmidt, G. B.; Huber, R. Isolation, Crystallization, Crystal Structure Analysis and Refinement of Constitutive C-Phycocyanin from the Chromatically Adapting Cyanobacterium *Fremyella Diplosiphon* at 1.66 Å Resolution. *J. Mol. Biol.* **1991**, *217* (3), 577–592.

(26) Wendler, J.; John, W.; Scheer, H.; Hoezwarth, A. R. Energy Transfer in Trimeric C-Phycocyanin Studied by Picosecond Fluorescence Kinetics. *Photochem. Photobiol.* **1986**, *44* (1), 79–85.

(27) Holzwarth, A. R.; Wendler, J.; Suter, G. W. Studies on Chromophore Coupling in Isolated Phycobiliproteins: II. Picosecond Energy Transfer Kinetics and Time-Resolved Fluorescence Spectra of C-Phycocyanin from *Synechococcus* 6301 as a Function of the Aggregation State. *Biophys. J.* **1987**, *51* (1), 1–12.

(28) Holzwarth, A. R.; Wendler, J.; Suter, G. W. Studies on Chromophore Coupling in Isolated Phycobiliproteins. *Biophys. J.* **1987**, *51* (1), 1–12.

(29) Sauer, K.; Scheer, H.; Sauer, P. Förster Transfer Calculations Based on Crystal Structure Data from *Agmenellum Quadruplicatum C*-Phycocyanin. *Photochem. Photobiol.* **1987**, *46* (3), 427–440.

(30) Sauer, K.; Scheer, H. Excitation Transfer in C-Phycocyanin. Forster Transfer Rate and Exciton Calculations Based on New Crystal Structure Data for C-Phycocyanins from *Agmenellum Quadruplicatum* and *Mastigocladus Laminosus*. *Biochim. Biophys. Acta* **1988**, *936*, 157–170.

(31) Debreczeny, M. P.; Sauer, K.; Zhou, J.; Bryant, D. A. Comparison of Calculated and Experimentally Resolved Rate Constants for Excitation Energy Transfer in C-Phycocyanin. 2. Trimers. *J. Phys. Chem.* **1995**, *99*, 8420–8431.

(32) Beck, W. F.; Sauer, K. Energy-Transfer and Exciton-State Relaxation Processes in Allophycocyanin. *J. Phys. Chem.* **1992**, *96* (11), 4658–4666.

(33) Edington, M. D.; Riter, R. E.; Beck, W. F. Evidence for Coherent Energy Transfer in Allophycocyanin Trimers. *J. Phys. Chem.* **1995**, *99* (43), 15699–15704.

(34) Edington, M. D.; Riter, R. E.; Beck, W. F. Interexciton-State Relaxation and Exciton Localization in Allophycocyanin Trimers. *J. Phys. Chem.* **1996**, *100* (33), 14206–14217.

(35) Riter, R. E.; Edington, M. D.; Beck, W. F. Isolated-Chromophore and Exciton-State Photophysics in C-Phycocyanin Trimers. *J. Phys. Chem. B* **1997**, *101* (13), 2366–2371.

(36) Edington, M. D.; Riter, R. E.; Beck, W. F. Femtosecond Transient Hole-Burning Detection of Interexciton-State Radiationless Decay in Allophycocyanin Trimers. *J. Phys. Chem. B* **1997**, *101* (22), 4473–4477.

(37) Homoelle, B. J.; Edington, M. D.; Diffey, W. M.; Beck, W. F. Stimulated Photon-Echo and Transient-Grating Studies of Protein-Matrix Solvation Dynamics and Interexciton-State Radiationless Decay in *α* Phycocyanin and Allophycocyanin. *J. Phys. Chem. B* **1998**, *102*, 3044–3052.

(38) Ying, L.; Xie, X. S. Fluorescence Spectroscopy, Exciton Dynamics, and Photochemistry of Single Allophycocyanin Trimers. *J. Phys. Chem. B* **1998**, *102* (50), 10399–10409.

(39) Womick, J. M.; Moran, A. M. Exciton Coherence and Energy Transport in the Light-Harvesting Dimers of Allophycocyanin. *J. Phys. Chem. B* **2009**, *113* (48), 15747–15759.

(40) Womick, J. M.; Moran, A. M. Vibronic Enhancement of Exciton Sizes and Energy Transport in Photosynthetic Complexes. *J. Phys. Chem. B* **2011**, *115* (6), 1347–1356.

(41) Tian, L.; van Stokkum, I. H. M.; Koehorst, R. B. M.; Jongerius, A.; Kirilovsky, D.; van Amerongen, H. Site, Rate, and Mechanism of Photoprotective Quenching in Cyanobacteria. *J. Am. Chem. Soc.* **2011**, *133* (45), 18304–18311.

(42) Tian, L.; Gwizdala, M.; van Stokkum, I. H. M.; Koehorst, R. B. M.; Kirilovsky, D.; van Amerongen, H. Picosecond Kinetics of Light Harvesting and Photoprotective Quenching in Wild-Type and Mutant Phycobilisomes Isolated from the Cyanobacterium *Synechocystis* PCC 6803. *Biophys. J.* **2012**, *102* (7), 1692–1700.

(43) Nganou, C.; David, L.; Adir, N.; Mkandawire, M. Linker Proteins Enable Ultrafast Excitation Energy Transfer in the Phycobilisome Antenna System of Thermosynechococcus Vulcanus. *Photochem. Photobiol. Sci.* **2016**, *15* (1), 31–44.

(44) Chang, L.; Liu, X.; Li, Y.; Liu, C.-C.; Yang, F.; Zhao, J.; Sui, S.-F. Structural Organization of an Intact Phycobilisome and Its Association with Photosystem II. *Cell Res.* **2015**, *25* (6), 726–737.

(45) Zhang, J.; Ma, J.; Liu, D.; Qin, S.; Sun, S.; Zhao, J.; Sui, S.-F. Structure of Phycobilisome from the Red Alga *Griffithsia Pacifica*. *Nature* **2017**, *551* (7678), 57–63.

(46) Dahlbom, M.; Beenken, W.; Sundström, V.; Pullerits, T. Collective Excitation Dynamics and Polaron Formation in Molecular Aggregates. *Chem. Phys. Lett.* **2002**, *364* (5), 556–561.

(47) Timpmann, K.; Rätsep, M.; Hunter, C. N.; Freiberg, A. Emitting Excitonic Polaron States in Core LH1 and Peripheral LH2 Bacterial Light-Harvesting Complexes. *J. Phys. Chem. B* **2004**, *108* (29), 10581–10588.

(48) Novoderezhkin, V. I.; van Grondelle, R. Physical Origins and Models of Energy Transfer in Photosynthetic Light-Harvesting. *Phys. Chem. Chem. Phys.* **2010**, *12* (27), 7352–7365.